國 立 交 通 大 學
光 電 工 程 學 系 博 士 班
博 士 論 文

雷射濺鍍法成長單晶非極性氧化鋅薄膜在藍寶石基板之光學與晶體結構相關特性研究

The correlation between optical and structural properties of nonpolar ZnO epitaxial films on sapphires grown by pulsed laser deposition

研 究 生：郭晉嘉

指 導 教 授：謝文峰 教授

中 華 民 國 一百零二 年 二 月

雷射濺鍍法成長單晶非極性氧化鋅薄膜在藍寶石基板之光學與晶體結構相關特性研究

The correlation between optical and structural properties of nonpolar ZnO epitaxial films on sapphires grown by pulsed laser deposition

研 究 生：郭晉嘉　　Student：Chin-Chia Kuo

指導教授：謝文峰 教授　　Advisor : Prof. Wen-Feng Hsieh

國 立 交 通 大 學

光 電 工 程 學 系 博 士 班

博 士 論 文

A Dissertation

Submitted to Department of Photonics and Institute of Electro-Optical Engineering

College of Electrical Engineering and Computer Science

National Chiao Tung University

In Partial Fulfillment of the Requirements

for the Degree of

Doctor of Philosophy

in

Electro-Optical Engineering

February 2013

Hsinchu, Taiwan, Republic of China

中華民國一百零二年二月

雷射濺鍍法成長單晶非極性氧化鋅薄膜在藍寶石基板之光學與晶體結構相關特性研究

研究生:郭晉嘉　　　　　　　　　　　　指導教授:謝文峰 教授

國立交通大學光電工程學系博士班

摘要

我們利用準分子雷射濺鍍的方法分別成長非極性的氧化鋅 $(1\bar{1}00)$ 與 $(11\bar{2}0)$ 的磊晶薄膜在 $(02\bar{2}4)$ 與 $(\bar{3}300)$ 的藍寶石基板上，而這些磊晶面的關係分別如下所示：$(11\bar{2}0)[1\bar{1}00]_{ZnO} \parallel (02\bar{2}4)[2\bar{1}\bar{1}0]_{sapphire}$ 與 $(1\bar{1}00)[11\bar{2}0]_{ZnO} \parallel (1\bar{1}00)[0001]_{sapphire}$。 非極性 $(11\bar{2}0)$ 氧化鋅的磊晶薄膜成長在 $(02\bar{2}4)$ 面的藍寶石基板上，會受到非等向性的應力作用造成晶格扭曲進而改變晶體的對稱性：由本來纖鋅礦 C_{6V} 的對稱性變成一個斜方晶系 C_{2V} 的對稱性。 從 X 光繞射分析可得知此非極性 $(11\bar{2}0)$ 氧化鋅的 c 軸是受到一個壓縮的應力，而另兩個方向都是拉伸的應力(y 軸延表面方向，x 軸是與 c 軸方向垂直且在 in-plane 上)。 當 x 與 y 軸的應力大小差距超過了 0.6%，這樣非等向性應力大小足夠讓晶體結構從原本的纖鋅礦 C_{6V} 的對稱性變成一個斜方晶系 C_{2V} 的對稱性。利用不同偏極化的拉曼光譜、光學反射與螢光光譜，我們都可以觀察到晶體對稱性由纖鋅礦 C_{6V} 改變到斜方晶系 C_{2V} 的結果。 拉曼光譜上特定的振動模態並不滿足 C_{6V} 的特性卻恰恰符合 C_{2V} 對稱性下的振動模態；而光學反射與螢光光譜發現特別的躍遷能階 E_1 與 E_2，這個有別於纖鋅礦氧化鋅的躍遷是由於晶體結構因為非等向性應力作用而變形成斜方晶系 C_{2V} 所造成的。

而成長在$(3\bar{3}00)$藍寶石基板的$(1\bar{1}00)$氧化鋅利用了額外的晶相$(1\bar{1}03)_{ZnO}$，來降低應力對其磊晶薄膜造成的影響。 這些雜相$(1\bar{1}03)_{ZnO}$的 a 軸與主結構$(1\bar{1}00)$氧化鋅的 a 軸是完全重疊在一起，像兩個原本$(1\bar{1}00)$氧化鋅的晶體對應其 a 軸往兩側各自旋轉約 59°並沿著$(1\bar{1}00)$氧化鋅的 c 軸排列；因此我們可以得這些不同晶相之間的磊晶面關係: $(1\bar{1}00)[11\bar{2}0]_{ZnO} \parallel (1\bar{1}03)\left[\bar{1}10\bar{1}\right]_{extra\ ZnO} \parallel (1\bar{1}00)[0001]_{sapphire}$。 此外我們也發現這些雜相的多寡與螢光光譜上的寬頻譜有關，這個躍遷能量大約在 3.17 電子伏特。 這個躍遷是由於不同晶相間的界面雜質或者是缺陷束縛激子所造成的，我們把它稱作是表面束縛激子。 當雜相的數量增加的同時也增加的界面的數量，進而產生出更多的表面束縛激子在這些邊界上。

為了解決雜相帶來的表面束縛激子發光，我們利用兩階段成長的方式來消除這些雜相的產生。當低溫成長緩衝層厚度在 47 到 67 奈米之間，這些緩衝層能夠分攤足夠的應力而讓再成長於高溫下的氧化鋅會是單純的$(1\bar{1}00)$晶面，但是如果低溫緩衝層的厚度超過或者是不足都會有雜相的產生。 利用兩階段成長所長出來的$(1\bar{1}00)$氧化鋅只要在低溫時沒有觀察到雜相的出現都能有很好的表面平整度，我們也發現雜相的數量增加會增加薄膜的表面粗糙度，所以表面粗糙度也可以用來初步判斷是否有雜相的形成。 低溫光學頻譜下我們發現了除了一般氧化鋅的發光特性外還有一個很強的基面堆疊缺陷發光，這是由於在兩階段成長的$(1\bar{1}00)$氧化鋅有較多的基面堆疊缺陷，而大量的基面堆疊缺陷分散了應力造成的影響並降低氧化鋅的應力作用。 所以兩階段成長確實能消除表面束縛激子發光與雜相的形成，並且能有效的降低應力對磊晶薄膜的影響也有較好的表面平整度。 我們也製作了非極性的量子結構，並證實不會有量子史塔克效應產生，光學特性主要都是受量子效應影響；這樣的結構也證實是比極性結構更適合應用在光學元件上。

The correlation between optical and structural properties of nonpolar ZnO epitaxial films on sapphires grown by pulsed laser deposition

Student: Chin-Chia Kuo Advisor: Prof. Wen-Feng Hsieh

Department of Photonics & Institute of Electro-Optical Engineering

National Chiao Tung University

Abstract

The nonpolar $(11\bar{2}0)$-and $(1\bar{1}00)$-oriented ZnO films have been epitaxially grown by pulsed laser deposition (PLD) on the sapphire $(02\bar{2}4)$ and $(3\bar{3}00)$ substrates. The epitaxial relationship of nonpolar *a*- and *m*-plane ZnO on *r*- and *m*-sapphires are $(11\bar{2}0)[1\bar{1}00]_{ZnO} \parallel (02\bar{2}4)[2\bar{1}\bar{1}0]_{sapphire}$ and $(1\bar{1}00)[11\bar{2}0]_{ZnO} \parallel (1\bar{1}00)[0001]_{sapphire}$, respectively.

Crystal symmetry breaking of wurtzite C_{6V} to orthorhombic C_{2V} due to in-plane anisotropic strain was investigated for nonpolar $(11\bar{2}0)$ ZnO epi-films grown on the *r*-sapphire. X-ray diffraction (XRD) results reveal the epi-layer is subjected to a compressive strain along the polar *c*-axis and tensile strain along both *y*-$[11\bar{2}0]$

surface normal and in-plane x-$[1\bar{1}00]$ axis. The strain difference between y- and x-axes is larger than 0.6% that introduces enough anisotropic strain to break the crystal symmetry from wurtzite C_{6V} to orthorhombic C_{2V}. The polarized Raman spectra of E_2 modes reveal violation of the C_{6V} selection rules; oppositely, the C_{2V} configuration satisfies the selection rules for the Raman modes. The observed E_1 and E_2 bands in polarized optical reflection and photoluminescence (PL) spectra, which are different from the typical ZnO for wurtzite structure, confirm the anisotropic strain causes the structure change to the orthorhombic one.

In the m-plane ZnO films grown on m-sapphire, small amount of $(1\bar{1}03)_{ZnO}$ domains were found providing strain relaxation of the m-ZnO matrix. And the a-axes of both the $(1\bar{1}03)_{ZnO}$ domains and the m-ZnO matrix are aligned with the c-axis of the m-Al_2O_3 substrate. The c-axis of the $(1\bar{1}03)_{ZnO}$ domains rotates about ±59° against the common a-axis of the m-ZnO. From this result, we found the epitaxial relationship of $(1\bar{1}00)[11\bar{2}0]_{ZnO} \,||\, (1\bar{1}03)\left[1\bar{1}0\bar{1}\right]_{extra\ ZnO} \,||\, (1\bar{1}00)[0001]_{sapphire}$. Through carefully correlating low-temperature polarized PL spectra with the XRD peak intensity ratio of $(1\bar{1}03)_{ZnO}/(1\bar{1}00)_{ZnO}$ of the samples grown at different temperature and after thermal treatment, we found that the broad-band emission around 3.17 eV may result from the interface defects trapped excitons at the boundaries between the $(1\bar{1}03)_{ZnO}$ domains and the m-ZnO matrix. The more $(1\bar{1}03)_{ZnO}$ domains in the m-ZnO layer cause the more surface boundary that makes the stronger surface-bound-exciton emission.

To eliminate the extra domain, we used the low-temperature (LT) grown buffer of m-ZnO to investigate the optical and crystalline properties. Examined by XRD,

we found when the thickness of LT-buffer layer is below 67 nm it contain no any extra domains, however, there exist a lot of extra domains for the thickness above 156 nm. The amount of extra domains increases with decreasing the buffer thickness. The optimal thickness of LT-buffer is from 47 to 67 nm, in which no observable extra $(1\bar{1}03)$-domains present in the two-step *m*-ZnO epilayers. The AFM measurement also shows the lower surface roughness for the two-step growth *m*-ZnO than those without buffers grown at the same temperature. This characteristics benefit for fabricating quantum-well (QW) structures. The LT-PL spectra show the three emission peaks around 3.364, 3.328 and 3.263 eV, which are attributed to the emissions of donor-bound excitons, basal plane stacking faults (BSFs) and free electron bound to acceptor emissions, respectively. The BSFs emission due to high BSFs density of ~2×10^6 cm^{-1} by TEM measurement, this value is larger than the m-ZnO without LT-buffer. The high BSFs density should provide the way to relax the lattice strain. In addition, the LT-PL spectra indicate absence of the broad-band emission at 3.17 eV result from the domain boundary trapping between the *m*-ZnO and extra domains which is dominant in the *m*-ZnO without LT-buffer.

Finally, 5 pairs of nonpolar *m*-plane ZnO/$Mg_xZn_{1-x}O$ quantum well structures were successfully grown on *m*-sapphire with LT *m*-ZnO LT-buffer. The results demonstrate these QW structures possess quantum confinement without experiencing the quantum confined Stark effect due to their nonpolar nature.

Acknowledgement

Ya~也終於能寫致謝了，在交大的日子算一算也超過七年半了，真是漫長又艱辛的歲月，不過最終還是給我撐到了。在這博士班五年半左右的日子最感謝的當然是謝老闆，想當初被叮得滿頭包連博士班也是吊車尾的，不過在老師的幫忙之下終於還是能往”成才”這兩個字靠攏一點了。再來要感謝的就是徐博啦，不只在 XRD 的幫忙跟教育外還要感謝您深厚的英文底子，每次都讓您辛苦改到我的 paper 我都很抱歉。

當然還要感謝實驗室的每一位共事過的學長學弟跟同學，首先要感謝松哥，碩班時期一起 NDL 到天明&後來博班時期給我的幫忙也是很巨大的；再來就是感謝維仁的幫助，讓我能有所成長也能有基本的技能能完成我的博士論文；碧軒也是幫忙我許多，不管是同步方面的問題或實驗方面的都受你幫忙很多，感謝!此外我還要感謝黃董&智章這兩位學長給我的幫助，豪哥&Poki 算是後博班時期的戰友。此外同期的喜憨(恭喜!)、明容、玫單跟狼王也是博班時期互相砥礪的戰友，再來實驗室的大仁哥與智雅現在就看你們囉~以及每一屆的學弟包含一直想找我真情流露的紹庭，很小隻的小單哥，居然叫我延畢陪他打球的老大，給力的鈺程，無力的宣民哥，建銘&育弘等等，都感謝各位在一路來的幫忙跟照顧。在此還要特別感謝大學同窗的禿頭 ki、基佬家軒、帝王亞育，以及兩位已為人父的蛇&霹靂叔，這些好朋友不管是在碩班、博班時期都是一起歡笑一起努力的好朋友，玩得不營養廢話也很多可是友情絕對不是隨便都可以說得清，一起努力人生吧!我的好朋友們。當然還有吳阿夫同學，身為他在交大唯一的朋友我也只能祝你幸福，雖然你會孤老一生，我還是由衷的期望有女人瞎了眼會跟你在一起，要幸福喔!還有壢中的另外四位同學，在我最失落的時候也是給我醉多的幫助，也感謝這四位在我人生的特別來賓幫我在這段日子增加不少風采。

最後當然是要感謝我爸媽在我這長期抗戰下還是給我無窮的助力跟支持，還有我老哥在生活上精神上的幫助，以及經驗上的分享讓我更能調適自己；再來就是彪哥啦，雖然你參予的是我博士班下半場的戰鬥，但是也是多虧你的陪伴這戰鬥才能更有活力，往後還有很多要一起面對的，一起努力吧。

Table of Contents

Abstract in Chinese…………………………………….…….…. **I**

Abstract in English……………………………………………. **III**

Acknowledgement………………………………………...**VI**

Table of Contents...**VII**

List of Figure Captions……………………………….....**XII**

List of Table……………………………………………...**XIX**

Chapter 1 Introduction…………………………………….**1**

1.1 Basic properties of ZnO-- overview of *c*-plane ZnO related problems……………………………………..………………**1**

1.1.1 Basic properties of ZnO………………………………………..…………1

1.1.2 Overview of *c*-plane (polar) ZnO and its problems…..……………………..4

1.2 Motivation……………………………………………...………**8**

1.3 Motives and contributions…………………………..……………**10**

1.4 Organization of the thesis……………………………..……….**11**

Chapter 2 Theoretical background of experimental methods........................…………………………………**16**

2.1 System and principle of laser-MBE………………..……………..**16**

2.1.1 Principle of laser-MBE……………………………………………………16

2.1.2 Description of laser-MBE system…………….……………………………18

2.2 Epitaxy………………………..……………………………………**19**

2.2.1 Lattice mismatch epitaxy (LME)………………………...……………19

2.2.2 Domain mismatch epitaxy (DME)……………………...………………..20

2.3 X-ray diffraction…………………………………….……………**21**

2.3.1 Theory of X-ray diffraction ……………………………………………....21

2.3.2 Radial scan………………………………………...…………………24

2.3.3 Rocking curve…………………………………..………………………24

2.3.4 Azimuthal scan……………………………………..………………….....25

2.4 Microscopy………………………..……………………………….**26**

2.4.1 Transmission electron microscopy (TEM)……………………………..26

2.4.1-1 Selected area electron diffraction (SAED)…………………………………...27

2.4.1-2 Two beam analysis……………………………………..………………..28

2.4.2 Atomic force microscopy (AFM)……………………..……...............29

2.5 Fundamentals of optical characterizations……………….........**31**

2.5.1 Photoluminescence (PL) characterizations……………………...................31

2.5.1-1 General concepts………………………..………………………………32

2.5.1-2 Free excitons…………………………..………………………………34

2.5.1-3 Bound excitons and Two-electron satellites……………………..……………..39

2.5.1-4 LO-phonon replicas……………………………………………..……………43

2.5.1-5 Defect emission……………………………………………………………44

2.5.2 Raman scattering measurement……………………………...........................45

2.5.2-1 Crystal structures…………………...……………………………………..45

2.5.2-2 Selection rules and phonon modes…..……………….................................48

Chapter 3 Experimental procedures and characterization technique…………………………………………………………..55

3.1 Growth nonpolar ZnO epilayers……………………………...............55

3.1.1 Cleaning process of substrate and target arrangement…….………...……..55

3.1.2 Operation arrangement of laser-MBE deposition.................……………...56

3.2 Structural and lattice dynamics characterization of the ZnO films……………………………...……………………………………..…58

3.2.1 X-ray diffraction (XRD)……………………...………………...……………58

3.2.2 Transmission electron microscopy (TEM)……………….………................58

3.2.3 Raman scattering spectra……………………………………….…………...…59

3.3 Surface morphology of the ZnO films - Atomic force microscopy…………………………………………..……………….....60

3.4 Measurements of optical properties……………………………....60

3.4.1 Photoluminescence system…………….…………………………………60

3.4.2 Optical reflection system………………..……………………………...61

Chapter 4 Anisotropic biaxial strains causing crystal symmetry breaking in nonpolar *a*-ZnO on *r*-sapphire.........63

4.1 Introduction...63

4.2 Crystallographic orientation of *a*-ZnO on *r*-sapphire..................64

4.3 Anisotropic strain versus the growth temperature……….……..70

4.4 The influence of anisotropic strains on optical properties in *a*-ZnO ……………………………...…………………………………...73

4.4.1 Polarized Raman measurement……………………………………...73

4.4.2 Optical emission properties of *a*-ZnO……………………………………78

4.5 Summary……………...……………………………………………80

Chapter 5 Influence of extra domain on crystalline and optical properties in nonpolar *m*-ZnO films on *m*-sapphire………………………………………………...84

5.1 Introduction……………………..…………………………………84

5.2 The crystal properties of *m*-ZnO on *m*-plane sapphire………....85

5.3 The defect states in *m*-ZnO……………………..………………91

5.4 Optical properties associated with domain interfaces in

***m*-ZnO**..94

5.5 Summary..100

Chapter 6 Eliminating extra domains in *m*-plane ZnO by two-step growth on *m*-sapphire..104

6.1 Introduction..104

6.2 Structural properties of *m*-ZnO by two-step growth..105

6.2.1 Low temperature (LT) growth *m*-ZnO buffer layers..105

6.2.2 The *m*-ZnO epi-films on LT-buffer..116

6.2.3 Defect states in the two-step grown *m*-ZnO films..122

6.3 Optical properties of two-step growth *m*-ZnO..125

6.3.1 PL spectra..125

6.3.2 Raman spectra..133

6.4 Non-polar quantum well structures on *m*-sapphire..138

6.5 Summary..140

Chapter 7 Conclusion and Prospective..146

7.1 Conclusion..146

7.2 Prospective..148

List of Figure Captions

Fig. 1-1 The typical ZnO PL spectrum at 300K. The ZnO film is c-plane orientation..2

Fig. 1-2 The wurtzite structure of ZnO……………………………………………..3

Fig. 1-3 Unit cell of wurtzite ZnO crystal……………………………………………..3

Fig. 1-4 (a) Schematic diagram of ZnO LEDs with and without ZnO/MgZnO. (b) comparison of EL spectra of the p–n homojunction ZnO LED and the ZnO LED with MgZnO layers…………………………………………………………………………4

Fig. 1-5 Internal field as a function of Mg-doping concentration in *c*-plane QWs…....7

Fig. 1-6 Dependences of PL transition energies on well width in *c*-plane QWs under different excitation intensities. The solid line is calculated exciton energies without the electric field and the dashed line corresponds to energy shift with the built-in electric field of 560 kV/cm……………………………………………………………..…7

Fig. 1-7 Schematic of surfaces of ZnO and sapphire, upper and lower are *a*-ZnO and *r*-sapphire and *m*-ZnO and *m*-sapphire, respectively. The rectangles represent the surface unit cells……………………………………………………………………...10

Fig. 2-1 Schematic diagram of Laser-MBE system…………………………………17

Fig. 2-2 Layout of laser-MBE………………………………………………………..19

Fig. 2-3 X-ray scattering from a cubic crystal……………………………………..…22

Fig. 2.4 X-ray diffraction $\theta - 2\theta$ scan……………………………………………....24

Fig. 2-5 X-ray diffraction rocking curve……………………………………………..25

Fig. 2-6 X-ray diffraction azimuthal scan……………………………………………26

Fig. 2-7 Scheme of the lens assembly and the ray path diagram forming the image (left) or the diffraction pattern (right)…………………………………………………...27

Fig. 2-8 Selected area electron diffraction…………………………………………...28

Fig. 2-9 Scheme of an atomic force microscope and the force-distance curve

characteristic of the interaction between the tip and sample……………………….**30**

Fig. 2-10 Band structure and selection rules for ZB and W structures. Crystal field and spin-orbit splitting are indicated schematically. Transitions rules, which are allowed for various polarizations of electric field vector with respect to the *c*-axis, are indicated……………………………………………………………………...**35**

Fig. 2-11 Reflection spectra from ZnO at 4.2K for (a) $\vec{E} \perp \hat{c}$ and $\vec{E} \parallel \hat{c}$ ……….....**36**

Fig. 2-12 Absorption coefficient of ZnO for annealed (solid lines) and without annealed (dotted line) shows at room temperature. The inset shows the absorption coefficient for the annealed sample at 77 K………………………………………….**37**

Fig. 2-13 Free excitonic fine structure region of the PL spectrum at 10K for a ZnO substrate…………………………………………………………………………….**37**

Fig. 2-14 Free carriers bound to point defects…………………………………….**40**

Fig. 2-15 Bound excitonic region of the 10K PL spectrum for a forming gas annealed ZnO substrate………………………………………………………………...…**41**

Fig. 2-16 PL spectrum at 10K for ZnO substrate in the TES region of the main bound exciton lines. Inset shows the donor binding energy is proportional to the exciton binding energy……………………………………………………………...…**41**

Fig. 2-17 PL spectrum for ZnO substrate at 10K in the region where donor-acceptor pair transition and LO-phonon replicas are expected to appear…………………...…**44**

Fig. 2-18 Schematic representation of a wurtzitic ZnO structure having lattice constants *a* and *c*; *u* parameter (0.375 in ideal) is the bond length, and α and β (109.47° in ideal) are the bond angles…………………………………...……**47**

Fig. 2-19 Displacement vectors of the phonon modes in ZnO wurtzite structure…...**51**

Fig. 3-1 Layout of the PLD growth system...**57**

Fig. 3-2 Schematic of a four-circle diffractomter..**58**

Fig. 3-3 Appearance of JEM-2100F TEM system..**59**

Fig. 3-4 Layout of PL system……………………………………………………….**61**

Fig. 3-5 Optical reflection system……………………………………………….....**62**

Fig. 4-1 **(a)** XRD radial scan along surface normal, in which only the ZnO $(11\bar{2}0)$ and sapphire $(02\bar{2}4)$ reflections were observed and (b) shows azimuthally *Φ*-scans across the ZnO $\{10\bar{1}0\}$ and sapphire $\{20\bar{2}2\}$ off-normal reflections…………...**66**

Fig. 4-2 The radical scans of surface normal along (a) $Al_2O_3[01\bar{1}2]$ and (b) $ZnO[11\bar{2}0]$, respectively…………………………………………………………………………...**67**

Fig. 4-3 Schematic illustrates the reciprocal spaces of *a*-ZnO/ *r*-Al_2O_3, the red and purple circles represent the reciprocal lattice point of *r*-sapphire and *a*-ZnO, respectively…………………………………………………………………………...**68**

Fig. 4-4 (a) With different Φ, the miscut of *r*-Al2O3 optical plane (black) and misalignment of $ZnO\left(11\bar{2}0\right)$ (red) as well as the FWHM of the rocking curve (blue) of the $ZnO\left(11\bar{2}0\right)$ plane growth at 400℃, respectively. The black arrow directs the maximum miscut and misalignment at Φ =45°. (b) The rocking curves of $ZnO\left(11\bar{2}0\right)$ shows the anisotropic distribution……………………………………..**70**

Fig. 4-5 (a) The lattice constant of *a*-ZnO and (b) in-plane strains along *c*-axis and normal *c*-axis with different growth temperature. The dash line of red and blue are the lattice constant for ZnO wafer. (a) and (b) also show anisotropic strains and strain relaxed with high temperature grown………………………………………………...**72**

Fig. 4-6 The unit cells of wurtzite ZnO and distorted ZnO are labeled as dash and solid lines, where y- and x-axes are the orthorhombic axes……………………….…**74**

Fig. 4-7 Polarized Raman spectra taken in 4 distinct backscattering configurations.

A spectrum of bare sapphire substrate is also plotted for comparison. The dashed lines at 101 and 436 cm^{-1} mark respectively the positions of $E_2^{(low)}$ and $E_2^{(high)}$ modes of bulk ZnO. A schematic of the scattering geometry is also shown in the inset…..**76**

Fig. 4-8 (a) polarized optical reflection and (b) polarized PL spectra of the *a*-ZnO epi-layer taken in various polarization configurations at 13K……………………….**79**

Fig. 5-1 XRD radial scans along the surface normal of *m*-ZnO/*m*-sapphire grown at two temperatures. (a) 500℃ and (b) 400℃. The red curve is the radial scan of *m*-sapphire wafer……………………………………………………………………..**87**

Fig. 5-2 Azimuthal scans across *m*-ZnO $\{10\bar{1}0\}$ off-normal reflections for growth temperatures at (a) 500℃ and (b) 400℃. The angular positions of sapphire{0006} reflections are marked by dashed lines as references………………………………...**88**

Fig. 5-3 Schematic of the diffraction pattern plotted along the $[11\bar{2}0]_{ZnO}$ zone axis. The Bragg reflections associated with the *m*-ZnO matrix and $(1\bar{1}03)_{ZnO}$ domains are depicted by red solid-circles and blue hollow-circles, respectively. Two $(1\bar{1}03)_{ZnO}$ domains share the same $[11\bar{2}0]_{m-ZnO}$ axis with the *m*-ZnO matrix but are rotated by ±59° around the $[11\bar{2}0]_{ZnO}$ axis, respectively…………………………………..…….**89**

Fig. 5-4 Plots of the peak intensity ratio of $(1\bar{1}03)_{ZnO}/(1\bar{1}00)_{ZnO}$ with different growth temperature………………………………………………………………………...**91**

Fig. 5-5 A cross-sectional TEM bright field micrograph (a) and a SAED pattern (b), taken at the *m*-ZnO/sapphire interface along the $[0002]_{ZnO}$ and $[11\bar{2}0]_{ZnO}$ zone axis. The lattices of *m*-ZnO and *m*-sapphire are marked, respectively, by solid and dashed lines……………………………………………………………………………….**92**

Fig. 5-6 The HRTEM micrographs taken along the (a) $[11\bar{2}0]_{ZnO}$ and (b) $[0002]_{m\text{-}ZnO}$

zone axis at *m*-ZnO/sapphire interface. The observed stacking faults in (a) were determined to be an intrinsic type-I_1 stacking fault. The inset in (b) shows a Fourier filtered image of the interface where the misfit dislocations are marked by ⊥.........**93**

Fig. 5-7 PL spectra of the samples grown at different temperatures measured the spectra show a strong NBE and a broad-band emission without the deep level transitions. A spectrum of the sample annealed at 850°C in O_2 is depicted by the black curve, where the SX band is suppressed. The inset shows the XRD intensity ratio of the $(1\bar{1}03)_{ZnO}$ reflection associated with the $(1\bar{1}03)_{ZnO}$ domains to the $(1\bar{1}00)_{ZnO}$ reflection of the *m*-ZnO (●) and the PL intensity ratio of SX/NBE (★) as a function of sample growth temperature..**96**

Fig. 5-8 (a) The polarized spectra of the sample grown at 450°C taken in various polarization configurations at 13 K and (b) the polarizability versus the excited polarization direction, where Φ=0° and Φ=0° mean the electric field vertical and parallel the *m*-ZnO *c*-axis. (c) The polarized PL peak (integrated) ratio of I_{SX}/I_{NBE} with different $(1\bar{1}03)_{ZnO}$ content at 13K...**97**

Fig. 6-1 The XRD radial scans of four thicknesses of LT-ZnO buffers grown at 175℃. The thicknesses are around (a) 4.7 nm, (b) 15.4 nm, (c) 58.3 nm, and (d) 156 nm, respectively. The extra domains are only observed for the 156nm sample.........**108**

Fig. 6-2 Azimuthal scans of LT-ZnO with various thicknesses. (a) 15.4 nm, (b) 58.3 nm, and (c) 156 nm. The yellow dashed lines indicate the sapphire $\{0006\}$ as references...**109**

Fig. 6-3 (a) The reciprocal space L-scan on $ZnO(0002)$ with various probed depths label as the H values. The value of L around 2.005 and 2.08 are due to $ZnO(0002)$ of *m*-ZnO and $ZnO(1\bar{1}0\bar{1})$ of extra domain. (b) The strain along the

$[1\bar{1}00]$ x-axis and the $[0002]$ z-axis, respectively……………………………..**112**

Fig. 6-4 AFM images of LT-ZnO with various thicknesses. (a) 1.7 nm, (b) 4.7 nm, (c) 15.4 nm, (d) 58.3 nm, and (e) 156 nm, respectively. (f) The cross-section profiles of AFM, the upper panel is for the thickness below 67 nm and the lower panel is from the AFM image of (e)……………………………………………………….**115**

Fig. 6-5 The XRD radial and azimuthal scans of two-step growth *m*-ZnO on *m*-sapphire with LT-buffers of 4.7 and 58.3 nm thick. (a) and (b) are the surface radial scans (black curves for the LT-buffers and red curves for the HT *m*-ZnO). (c) and (d) are the azimuthal scans. The yellow dashed lines indicate the sapphire {0006} reflections……………………………………………………………………...**118**

Fig. 6-6 The strains along the $[1\bar{1}00]$ *x*-axis and the $[0002]$ *z*-axis, respectively.**119**

Fig. 6-7 The AFM images of two-step *m*-ZnO epilayers with various thicknesses of LT-buffers, (a) 4.7 nm, (b) 58.3 nm, and (c) 156 nm. (e) The cross-section profiles of AFM images of (a)-(d). (f) The 3-D image of the *m*-ZnO/*m*-sapphire without LT-buffer……………………………………………………………………….**121**

Fig. 6-8 (a) The selected area electron diffraction (SAED) of TEM along $[11\bar{2}0]_{ZnO}$ zone-axis, (b) high resolution TEM TEM images of the *m*-ZnO/sapphire interface along $[0002]_{ZnO}$ zone-axis, and (c) The TEM dark field image along $[11\bar{2}0]_{ZnO}$ zone-axis with $\vec{g}=[1\bar{1}00]_{ZnO}$. The inset in (b) is inverse Fourier transform image from interface with $\vec{g}=[11\bar{2}0]_{ZnO}$…………………………………………………..**124**

Fig. 6-9 The PL spectra of two-step growth m-ZnO and direct growth shown red and black lines at 13K. The peaks at about 3.321 and 3.264 eV are labeled with the X and Y bands……………………………………………………………………...**127**

Fig. 6-10 The dependences of Y band position (blue circles) and intensity ratio (black

stars) of X-band/D_0X on the pumping power (a) and the TES binding energy versus the donor binding energy (b). The red line is ideal Haynes rule and black points are the donor binding energy proportional to exciton binding energy of two-step samples with various thicknesses of LT-buffers…………………………………………..**128**

Fig. 6-11 The temperature dependent PL spectra (a) and (b) peaks position of $FX_{A,B}$, D_0X, TES, X-band and (e, A) of two-step m-ZnO with ~58.3 nm buffer which possesses no extra domains. The dashed lines in (a) are the phonon replica of (e, A). The temperature dependent peaks position of $FX_{A,B}$, D_0X, TES, X-band and (e, A) are labeled with black, red, blue, pink and green points, respectively in (b). The solid curves are the fittings to the Bose-Einstein equation……………………………..…**131**

Fig. 6-12 The polarization dependent Raman spectra of the direct growth *m*-ZnO samples on *m*-sapphires without buffer layers grown at various temperatures. (a) 400℃, (b) 500℃, and (c) 550℃, respectively. The blue circles are sapphire modes. Black dashed and red solid lines are E_2^{high} mode at 443.02 cm^{-1} and 580 cm^{-1}. (d) The normalized peak intensity of LO-phonon modes and extra domains contents depend on growth temperature…………………………………………………...**134**

Fig. 6-13 The polarization dependent Raman spectra of two-step growth *m*-ZnO with buffer thickness ~ 4.7 nm (a) and the E_2^{high} mode frequency and strain of *x*-axis versus the thickness of LT-buffers (b). The extra domains content ($(1\bar{1}03)_{ZnO} / (1\bar{1}00)_{ZnO}$) is around $\sim 3.4\times10^{-5}$. The peaks marked by blue circles are the sapphire modes…**138**

Fig. 6-14 The PL spectra of *m*-plane MQWs with well widths of 4, 8 and 16 nm measured at 13K. (a) The PL spectrum of nonpolar MQWs of 4 nm well width shows the near-band edge (NBE) emissions from barriers, respectively; and (b) The PL spectra of various well widths indicated. The dashed line is the NBE emission of bulk ZnO………………………………………………………………………**140**

List of Table

Table 2-1 Phonon modes frequencies for wurtzite ZnO……………………………..…**50**

Table 3-1 List the parameters of growth for ZnO epilayers..**57**

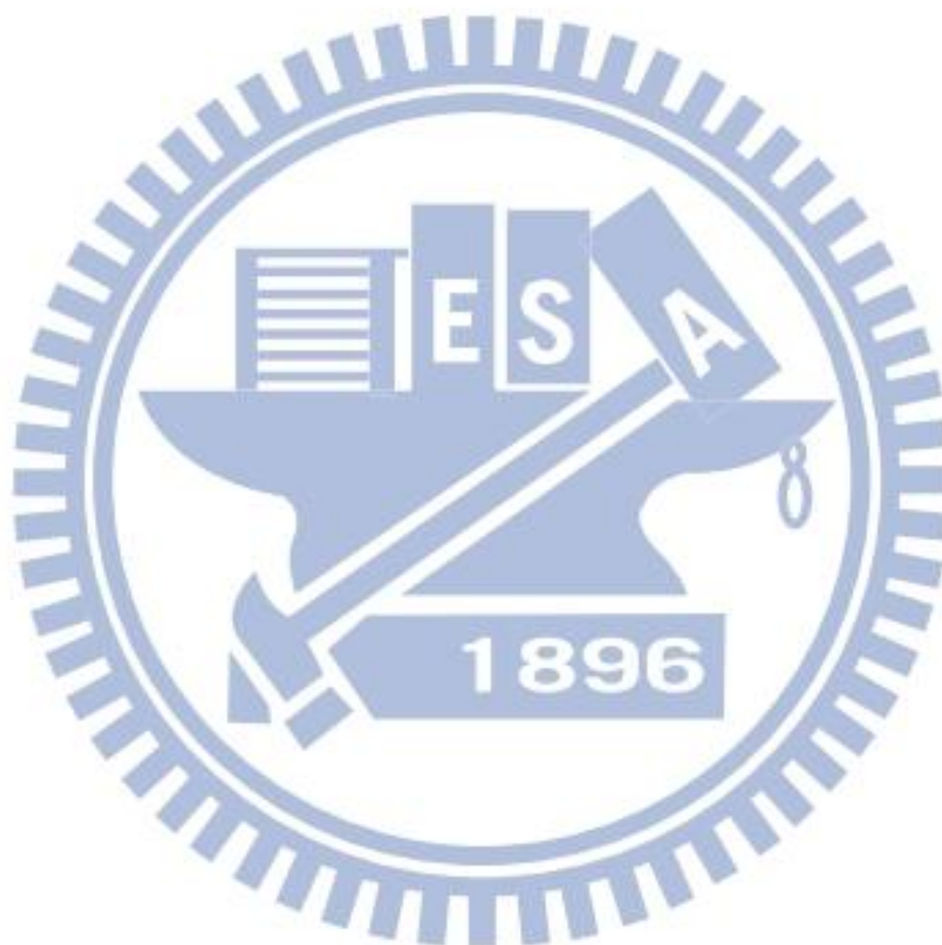

Chapter 1 Introduction

1.1Basic properties of ZnO-- overview of *c*-plane ZnO related problems

1.1.1 Basic properties of ZnO

ZnO is a direct band gap semiconductor and has been considered as one of the most promising candidates for the materials used in ultraviolet (UV) photonic devices due to its wide band gap of 3.37 eV at room temperature (RT). The advantage for its UV photonic applications is the stability of the ZnO free exiton having large binding energy of 60 meV, which is much larger than that of ZnSe and GaN [**1, 2**]. The nature of high thermal conductivity, high luminous efficiency and mechanical and chemical robustness has made ZnO and its alloys the promising material system for light-emitting devices (LED) operated in the UV spectral region [**3**]. Owing to these properties, the strong commercial desire for blue and UV diode lasers and LEDs has prompted research efforts on II-VI wide band-gap semiconductors [**4**].

The fundamental optical properties of ZnO are characterized by the spectra of photoluminescence (PL), photoconductivity, reflection and absorption. The optical spectra reflect the intrinsic direct band gap, strongly bound exciton states, and gap states arising from point defects, etc. Figure 1-3 shows a typical PL spectrum of ZnO at RT. There exist a strong near-band-edge (NBE) in UV range of the PL peak at ~ 3.27 eV, which is attributed to free exciton transitions, as the exciton binding energy is ~ 60 meV. In addition, visible emission around 2.4 eV is also observed as a result of defect states. The detailed crystal structure and optical transitions of PL spectra will be further discussed in Chapter 2.

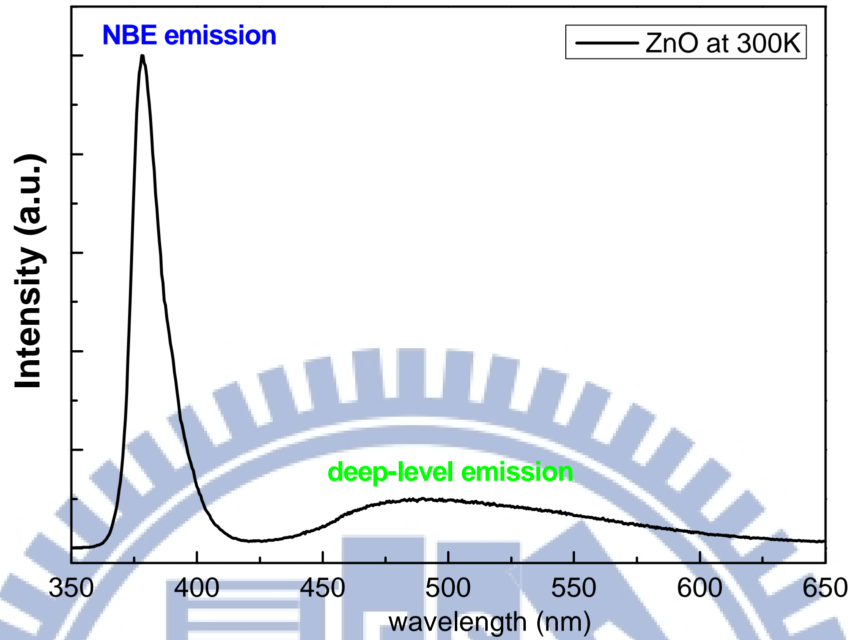

Fig. 1-1 The typical ZnO PL spectrum at 300K. The ZnO film is c-plane orientation.

In crystallography, ZnO crystal is hexagonal wurtzite structure as schematically shown in Fig. 1-2 with lattice constants of *a* = 3.2496 A and *c* = 5.2069 Å. The hexagonal ZnO has a point group C_{6V} and the space group is P_{63mc} or C_{6V}^{4}. The gray and yellow spheres denote Zn and O atoms, respectively. There are three main faces composed in hexagonal structure, *c*-face (0001), *m*-face $(1\bar{1}00)$ and *a*-face $(11\bar{2}0)$ as shown in Fig. 1-3. The arrangement of *c*-plane is consisted of Zn and O atoms layer by layer along the *c*-axis that gives rise to a net spontaneous dipole field along the *c*-axis, the preferentially grown orientation of ZnO.

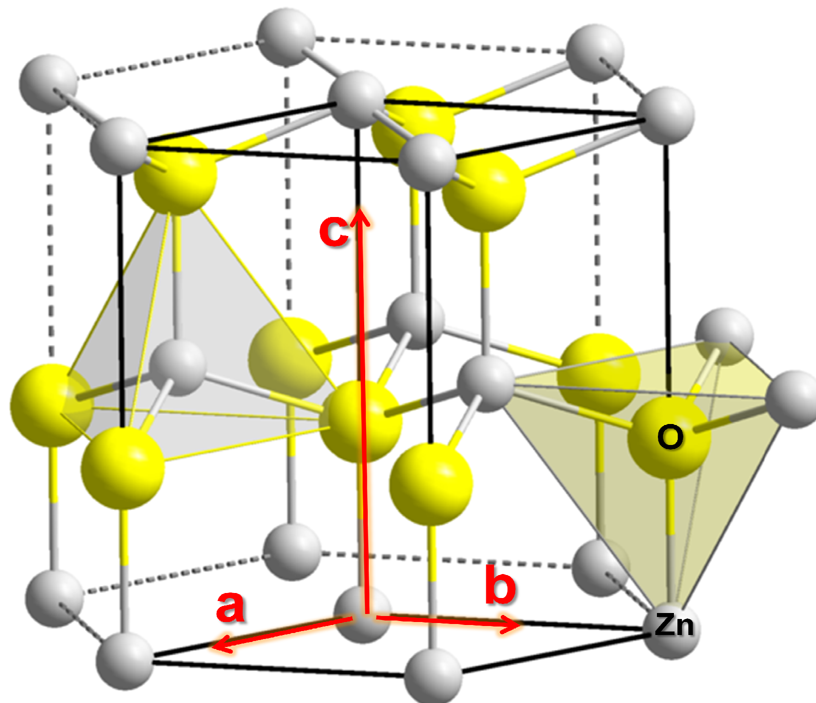

Fig. 1-2 The wurtzite structure of ZnO.

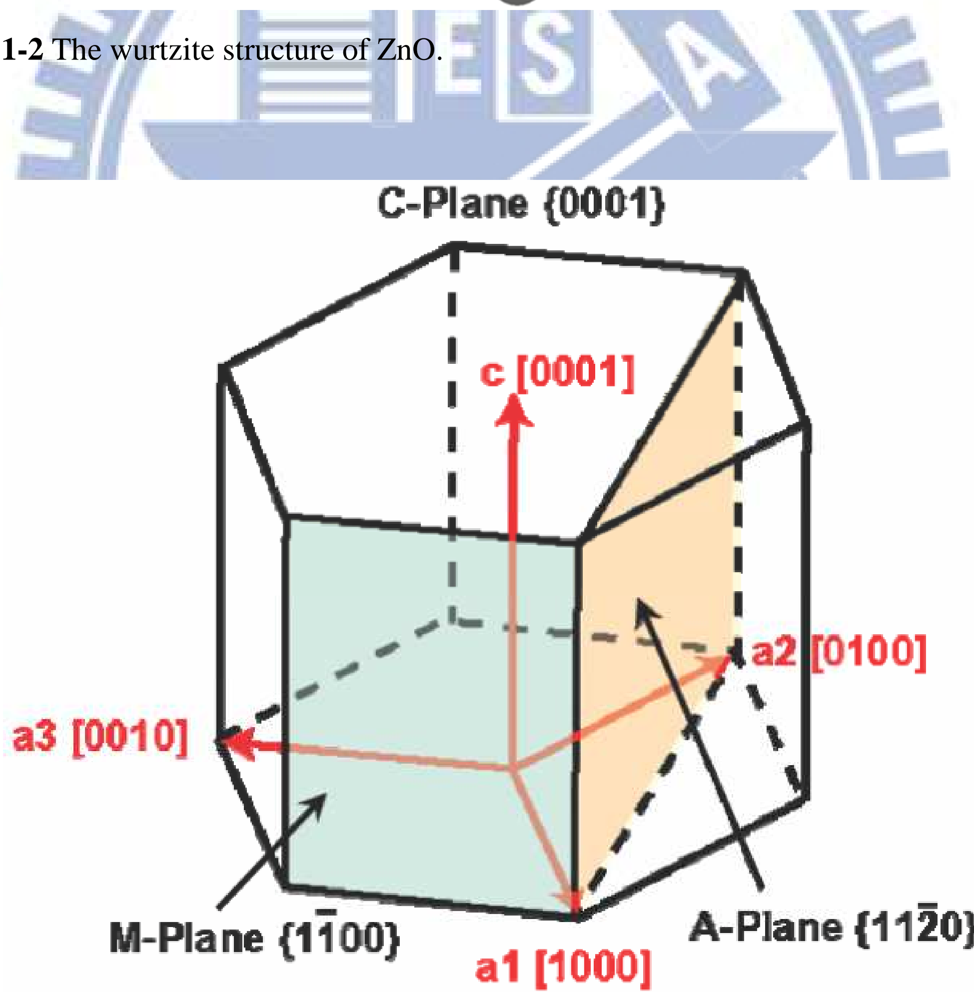

Fig. 1-3 Unit cell of wurtzite ZnO crystal.

1.1.2 Overeview of *c*-plane (polar) ZnO and its problems

UV LEDs and laser diodes (LDs) are of interest for their powerful use in long-lifetime and energy saving solid-state lighting, and high-density information storage. Moreover, the lasing actions of ZnO materials have been demonstrated in thin films, nanowires and nanostructure [**5-10**]. The lasing mechanism is attributed to the exciton-exciton scattering and electron-hole plasma process. The combination of these characteristics and proper optical cavity to match optical emission of ZnO makes ZnO a system of choice for thin film UV photonic or electro-optic device applications [**11**]. In 2005, Tsukazaki *et al.* [**12**] reported the first blue LED of homostructural *p-i-n* junction based on *c*-plane ZnO operated by feeding in a direct current of 20 mA, however, the spectrum of the *c*-ZnO LED shows strong green (deep-level) emission and weak UV emission. In 2006, Lim *et al.* [**13**] fabricated the *c*-ZnO LED with *p-n* homojunction and *p-n* heterojunction containing the ZnO/MgZnO as shown in Fig. 1-4(a). The elecroluminescence (EL) spectra shown in Fig. 1-4(b) indicate that increasing NBE emission at 380 nm at RT with great suppression of the deep-level emission by using ZnO/MgZnO heterostructure.

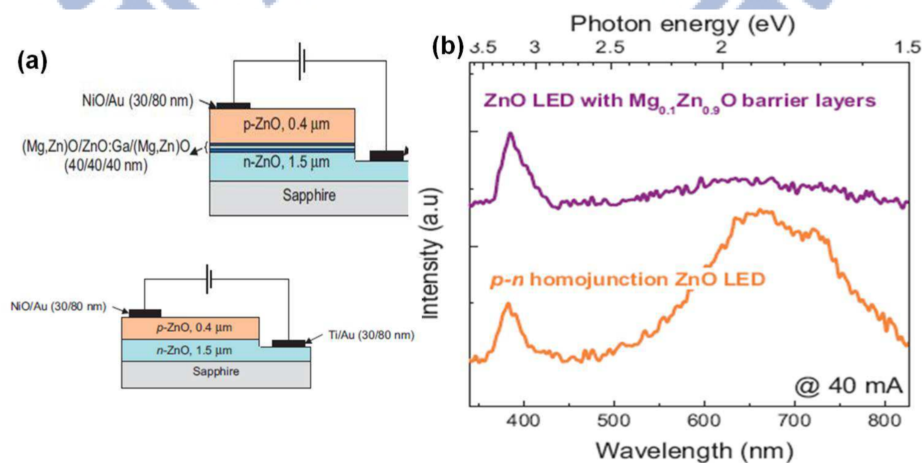

Fig. 1-4 (a) Schematic diagram of ZnO LEDs with and without ZnO/MgZnO. (b) comparison of EL spectra of the p–n homojunction ZnO LED and the ZnO LED with MgZnO layers. [**13**]

The driving force for ZnO UV photonic applications is the stability of the free exiton having large binding energy of 60 meV, which assures more efficient excitonic emission at RT or even at higher temperatures. Moreover, the excitons in ZnO-based quantum well (QW) exhibit strong stability as compared to ZnO bulk or III–V QWs due to the enhancement of the binding energy [**14-17**] and the reduction of the exciton–phonon coupling [**18, 19**] caused by quantum confinement. Due to above effects, excitons are expected to play an important role in many-body processes such as laser action of ZnO QWs even at RT. Usually, ZnO layers grow preferentially with c-plane normal. In this orientation, ZnO consists of alternative layers of Zn cations and O anions along the growth direction that gives rise to a net piezoelectric and spontaneous dipole field along the *c*-axis. In addition, the effect of internal electric fields inside QW layers might be taken into account for ZnO QWs having a relatively high barrier height. Compare ZnO-based QWs with the c-plane orientation as those having been extensively investigated in wurtzite GaN-based QW structure, piezoelectric and spontaneous polarization effects present as a consequence of role, there are many advantages of ZnO-based materials, e.g., the band gap engineering of MgZnO can tunable from 3.37 to 5.4 eV, [**2**] which is a high barrier gap to give higher exciton confinement and recombination rate.

Figure 1-5 shows comparison of the built-in electric fields of ZnO/MgZnO and GaN-base QW as a function of Mg or In concentration [**20-22**]. In the same dopant concentrations of the barriers, the ZnO-based QWs show weaker built-in electric field than that of GaN-based. The more dopant makes the more piezoelectric field induced by the strain at the QW interfaces due to lattice mismatch and the MgZnO barrier layers is relatively large, since the directions of spontaneous and piezoelectric polarizations along the ZnO wells are coincident with respect to each other, the electric field induces inclination of the band profiles is considered to become

significant. The phenomenon is called the quantum-confinement Stark effect (QCSE), the QCSE results from the large internal electric field to tilt band diagram to reduce the exciton oscillator strength through separation of the wave functions of the electron and hole, in turn the exciton binding energy and to make the optical emission red-shift.

Recently, it is reported that the QCSE dominates the optical emission in *c*-plane ZnO/MgZnO QWs when their well widths exceed ~ 4 nm due to the large internal electric field, whereas, the quantum confinement effect dominates for the well width is smaller than 4 nm, as shown Fig. 1-6 [**23-29**]. In the regime of quantum confinement, the energy of NBE emission blue shifts with decreasing well width, and it red shifts with increasing well width in the QCSE regime. The internal electric field is estimated to be ~ 300 kV/cm for 10% Mg doping [**24, 25**]. The higher concentration of Mg make the higher quantum confinement effect, unfortunately, there are a large built-in field of the order of 1 MV/cm when Mg concentration exceed 20% [**25, 26**]. The QCSE also influenced on the lifetime of exciton, which is inversely proportional to the recombination rate of electron and hole [**26, 27**]. The short lifetime of exciton is observed when the quantum confinement is dominant; the the life time becomes longer due to reduction of the recombination rate of electron and hole if the QCSE is dominant [**30**]. The photoexcitation screening effect with the more electrons and holes interaction to reduce the band tilting of internal electric field on the luminescence energy is evidenced by the luminescence blue shift with an increase in excitation intensity [**27-29**]. The *c*-plane ZnO QWs has the QCSE due to the internal field that leads to reduce the optical gain [**31, 32**] and presents a barrier for achieving the larger efficiency of optoelectronic devices.

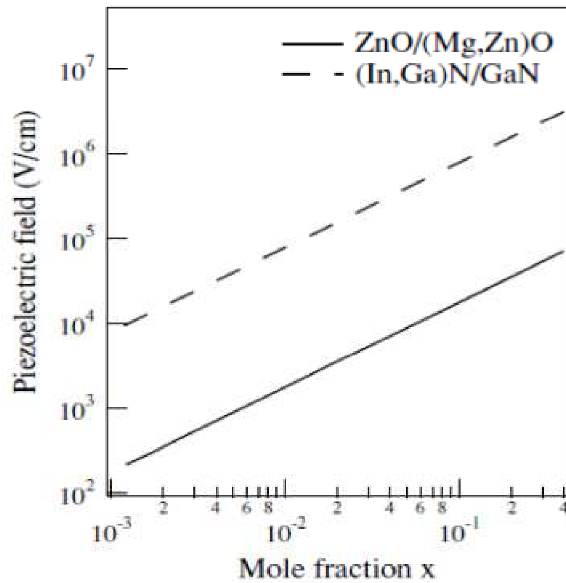

Fig. 1-5 Internal field as a function of Mg-doping concentration in *c*-plane QWs. [**23**]

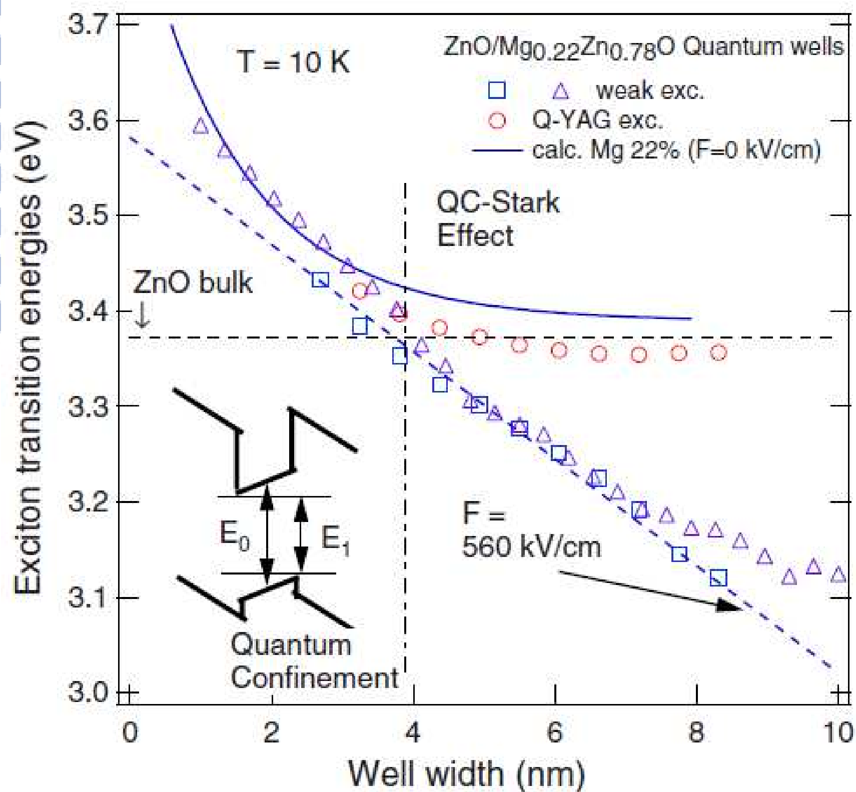

Fig. 1-6 Dependences of PL transition energies on well width in *c*-plane QWs under different excitation intensities. The solid line is calculated exciton energies without the electric field and the dashed line corresponds to energy shift with the built-in electric field of 560 kV/cm. [**29**]

1.2 Motivation

Until now many ZnO/MgZnO-based heterostructures have been grown with c-plane (polar) orientation. Unfortunately, the wurtzite ZnO layers exhibit built-in electric field in this crystallographic orientation, which can be of the order of 1 MV/cm along the *c*-axis [**25-26, 33**]. Hence, polarization discontinuities exist along the c-plane growth direction and create fixed sheet charges at surfaces and interfaces in polar structure. The total polarization of ZnO film contributed from spontaneous and piezoelectric polarization creates an internal electric field that could bend the potential band and spatially separate wave functions of electron and hole in quantum wells. This phenomenon causes red shift in NBE emission, reducing the carrier recombination, lengthening the carrier lifetimes, and consequently decreasing the internal quantum efficiency. Therefore, devices with ZnO of nonpolar orientations, such as *a*-plane $(11\bar{2}0)$ and *m*-plane $(1\bar{1}00)$, have been proposed to improve the quantum efficiency. The growth on nonpolar surface QWs has been proposed to avoid the built-in electric field, and the nonpolar QWs have already been demonstrated in GaN-based nonpolar heterostructures [**34**]. The life time of excitons in the *m*-plane MQWs was averagely much decreased to 0.45 ns, which is much shorter than that in the *c*-plane MQWs [**34**]. Kuokstis *et al.* [**35**] have demonstrated no build-in electric field in the nonpolar structure in 2002, they used power dependent PL to confirm no existence of internal electric field. Since the *c*-plane MQWs possess internal electric field, the increased excited carriers by pumping would produce an opposite electric field in QW to screen the build-in field to reduce the QCSE thus cause a blue-shift in PL emission, whereas the screen effect don't happen in the nonpolar MQWs. In addition, the nonpolar structure of GaN film also shown optical properties and polarization effect were first revealed by Domen *et al.* [**36**].

They found *m*-plane GaN could emit polarized light emission due to different amount of excitons recombined between different energy levels. Those effects also exist in nonpolar ZnO material.

Recently, there are many nonpolar *a*- or *m*-plane ZnO layers have fabricated by $LaAlO_3$ [**37, 38**], $LiAlO_3$ [**39-41**] and sapphire [**42-47**] substrates. Among those substrates the sapphire substrate is the low-cost and prevalent substrate than others. The growth direction of either *m*- or *a*-plane ZnO is perpendicular to that of traditional *c*-plane ZnO, the hetero-epitaxial growth of nonpolar ZnO always suffers biaxial stress comes from different crystal orientations. Chauveau *et al.* have reported the epitaxial relationship between sapphire and nonpolar ZnO and the lattice mismatching model [**47**]. The in-plane lattice parameters are indicated in both *a*- and *m*-plane ZnO in Fig. 1-7. Although the literatures for nonpolar ZnO films growth and epitaxial structure plentifully has been reported that nonpolar *m*- or *a*-plane ZnO film can be grown on *m*- or *r*-plane sapphire substrate, the optical characteristics is more important resulting from the ZnO applications for optoelectronic devices. However, the optical characteristics of nonpolar ZnO films systems are rarely reported and the crystalline structures correlated with optical characteristic are very scarce.

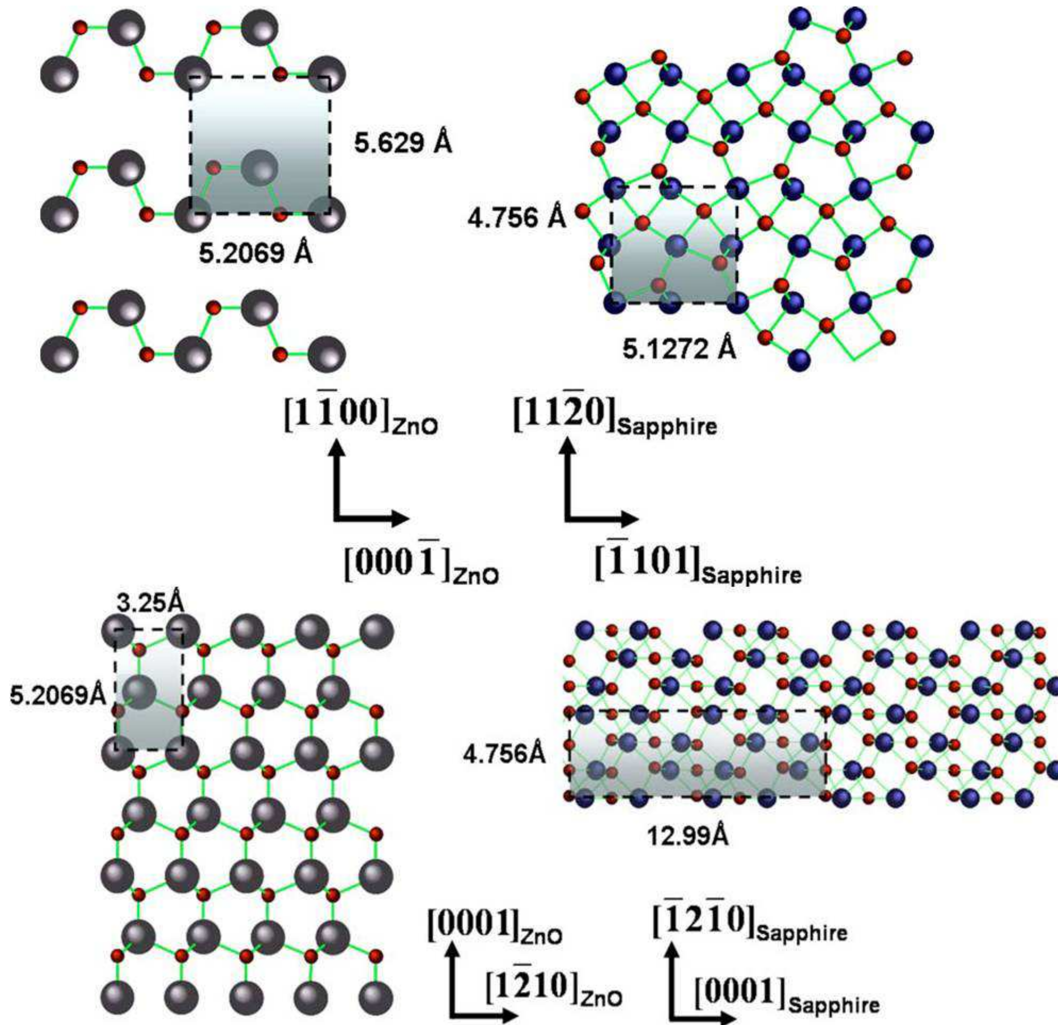

Fig. 1-7 Schematic of surfaces of ZnO and sapphire, upper and lower are *a*-ZnO and *r*-sapphire and *m*-ZnO and *m*-sapphire, respectively. The rectangles represent the surface unit cells. [**47**]

1.3 Motives and contributions

Because the nonpolar ZnO epilayer has advantages including no build-in electric field, high degree of polarization and it is expected to be a good candidate for making high-performance photonic devices, we shall study on fabrication and optical characterizations of the nonpolar *a*- and *m*-plane ZnO epilayers on *r*- and *m*-sapphire substrates. However, the asymmetrical strain from the lattice mismatch at the interface of growth layer and substrate will be a critical issue, which makes the

epitaxial growth difficult. We will investigate the influence of strain and defect effects on the optical characteristics of the nonpolar ZnO epitaxial grown on the sapphire based substrates. The optical characterization of nonpolar ZnO films will be conducted to correlate their crystal structure with optical properties. Although the peculiar optical transitions of *a*-ZnO has been reported, the correlation of crystal structure still not be confirm clearly. In use of XRD and polarization dependent Raman spectroscopy, we thoroughly study the influence of anisotropic strain state on the crystal symmetry to cause the symmetry breaking and explain the peculiar optical transitions resulting from how and what the symmetry changes from wurtzite. In addition, the extra domains have often been reported in *m*-ZnO layers, but there is rare reported the extra domains play the role in optical characteristic. For the first time in our knowledge, we correlate the content of extra domains in *m*-ZnO thin films with the broad-band emission in LT-PL spectra. We also find the way to eliminate extra domains to reduce the broad-band emission. The clear correlation of crystalline properties with optical emission will also show in this thesis.

1.4 Organization of the thesis

This thesis will be organized as follows. In the next chapter, I will introduce the theoretical background of experimental methods and theory. Chapter 3 is the experimental procedures and measured systems. Finally, in Chapters 4, 5 and 6, I will discuss the nonpolar *a*- and *m*-plane ZnO on sapphire substrates. Chapter 7 give the conclusion and the future works of my study.

References

1. B. X Lin, Z. X. Fu, and Y. B. Jia, Appl. Phys. Lett. 79, 943 (2001).
2. Mollwo E 1982 *Semiconductors: Physics of II–VI and I–VII Compounds, Semimagnetic Semiconductors (Landolt-B¨ornstein New Series)* O Madelung, M Schulz and H Weiss (Berlin: Springer) vol 17 , p 35
3. Y. Segawa, A. Ohtomo, M. Kawasaki, H. Koinuma, Z. Tang, P. Yu and G. Wong, *Phys. Status Solid* b 202 609 (1997)
4. Y. Chen, D. M. Bahnall, H. Koh, K. Park, K. Hiraga, Z. Zhu, and T. Yao, J. Appl Phys. Lett. 84, 7 (1998).
5. R. M. Ma, X. L. Wei, L. Dai, S. F. Liu, T. Chen, S. Yue, Z. Li,Q. Chen and G. G. Qin, *Nano Lett.*, 9, 2697 (2009).
6. P. Yang, H. Yan, S. Mao, R. Russo, J. Johnson, R. Saykally, N. Morris, J. Pham, R. He and H. J. Choi, *Adv. Funct. Mater.*, 12, 312 (2002).
7. M. H. Huang, S. Mao, H. Feick, H. Yan, Y. Wu, H. Kind, E. Weber, R. Russo, P. Yang, *Science,* 292, 1897 (2001).
8. S. F. Yu, Clement Yuen, and S. P. Lau, W. I. Park and Gyu-Chul Yi, *Appl. Phys. Lett.*, 84, 3241 (2004).
9. H. C. Hsu, C. Y. Wu and W. F. Hsieh, *J. Appl. Phys.*, 97, 064315 (2005).
10. X. Ma, P. Chen, D. Li, Y. Zhang, and D. Yang, *Appl. Phys. Lett.*, 91, 251109 (2007).
11. Gregory J. Exarhos, and Shiv K. Sharma, Thin Solid Film 270, 27 (1995).
12. A. Tsukazaki, A. Ohtomo, T. Onuma, M. Ohtani, T. Makino, M. Sumiya, K. Ohtani, S. F. Chichibu, S. Fuke, Y. Segawa, H. Ohno, H. Koinuma, and M. Kawasaki, *Nature Mater.* 4 42 (2005)
13. J.-H. Lim, C.-K. Kang, K.-K. Kim, Il-K. Park, D.-K. Hwang and S.-J. Park, Adv. Mater. 18, 2720 (2006)

14. H. D. Sun, T Makino, N. T. Tuan, Y. Segawa, K. Z.Tang, G. K. L. Wong, M Kawasaki, A Ohtomo, K Tamura and H. Koinuma, Appl. Phys. Lett. 77 4250 (2000).
15. H. D. Sun, T. Makino, Y. Segawa, M. Kawasaki, A. Ohtomo, K. Tamura and H, Koinuma, J. Appl. Phys. 91, 1993 (2002).
16. G. Coli and K. K. Bajaj, Appl. Phys. Lett. 78, 2861 (2001).
17. W. T. Hsu, K. F. Lin, and W. F. Hsieh, Appl. Phys. Lett. 91, 181913 (2007).
18. H. D. Sun,T. Makino, N. T. Tuan, Y. Segawa, M. Kawasaki, A. Ohtomo, K. Tamura and H. Koinuma, Appl. Phys. Lett. 78, 2464 (2001)
19. J W Sun and B P Zhang, Nanotechnology 19, 485401 (2008)
20. P. B. Schwarz, K. Khachaturyan and E. R. Weber, Appl. Phys. Lett., 70, 1122 (1997).
21. L. G¨orgens, O. Ambacher, M Stutzmann, C Miskys, F Scholz and J. Off, Appl. Phys. Lett., 76, 577 (2000).
22. A Bykhovski, B Gelmont and M. Shur, J. Appl. Phys., 74 6734 (1993)
23. T Makino, Y Segawa, M Kawasaki and H Koinuma, Semicond. Sci. Technol., 20 78 (2005)
24. B. P. Zhang, B. L. Liu, J. Z. Yu, Q. M. Wang, C. Y. Liu, Y. C. Liu and Y. Segawa, Appl. Phys. Lett., 90, 132113 (2007)
25. T. Bretagnon, P. Lefebvre, T. Guillet, T. Taliercio, B. Gil and C. Morhain, Appl. Phys. Lett., 90, 201912 (2007)
26. T. Makino, A. Ohtomo, C.H. Chia, Y. Segawa, H. Koinuma and M. Kawasaki, Physica E, 21, 671 (2004)
27. C. Morhain, T. Bretagnon, P. Lefebvre, X. Tang, P. Valvin, T. Guillet, B. Gil, T. Taliercio, M. Teisseire-Doninelli, B. Vinter, and C. Deparis, *Phys. Rev.* B 72, 241305 (2005).

28. J A Davis, L V Dao, X Wen, C Ticknor, P Hannaford, V A Coleman,H H Tan, C Jagadish, KKoike, S Sasa, M Inoue and M Yano, Nanotechnology, 19 055205 (2008)

29. T. Makino, Y. Segawa, A. Tsukazaki, A. Ohtomo, and M. Kawasaki, Appl. Phys. Lett. 93, 121907 (2008)

30. B Gil, P Lefebvre, T Bretagnon, T Guillet, J A Sans, T Taliercio and C Morhain, *Phys. Rev.* B 74, 153302 (2006)

31. S-H Park and D. Ahn, *Appl. Phys. Lett.* 87 253509 (2005).

32. J S Im, H Kollmer, J Off, A Sohmer, F Scholz and A Hangleiter, *Phys. Rev.* B 57 R9435 (1998)

33. J-M Chauveau, M La¨ugt, P Vennegu`es, M Teisseire, B Lo, C Deparis, C Morhain and B Vinter, Semicond. Sci. Technol. 23, 035005 (2008)

34. P Waltereit, O Brandt, A Trampert, H T Grahn, J Menniger, M Ramsteiner, M Reiche and K H Ploog, *Nature* 406, 865 (2000)

35. E. Kuokstis, C. Q. Chen, M. E. Gaevski, W. H. Sun, J. W. Yang, G. Simin, M. Asif Khan, H. P. Maruska, D. W. Hill, M. C. Chou, J. J. Gallagher, B. Chai, Appl. Phys. Lett. 81, 4130, (2002).

36. K. Domen, K. Horino, A. Kuramata, T. Tanahashi, Appl. Phys. Lett. 71, 1996, (1997).

37. Yen-Teng Ho, Wei-Lin Wang, Chun-Yen Peng, Mei-Hui Liang, Jr-Sheng Tian, Chih-Wei Lin, and Li Chang, Appl. Phys. Lett. 93, 121911 (2008)

38. J-S Tian, M-H Liang, Y-T Ho, Y-A Liu, and L. Chang, Journal of Crystal Growth 310, 777 (2008)

39. S. Zhou, J. Zhou, T. Huang, S. Li, J. Zou, J. Wang, X. Zhang, X. Li, and R. Zhang, Journal of Crystal Growth 303, 510 (2007)

40. Mitch M.C. Chou, L. Chang, H-Y Chung, T-H Huang, J-J Wu, and C-W Chen,

Journal of Crystal Growth 308, 412 (2007)

41. Mitch M.C. Chou, L. Chang, D-R Hang, C. Chen, D-S Chang, and C-A Li, Crystal Growth & Design, 9,2073 (2009)
42. J. Zu’n˜iga-Pe’rez, V. Mun˜oz-Sanjose’, E. Palacios-Lido’n, J. Colchero, Appl. Phys. Lett. 88, 261912 (2006).
43. T. Moriyama, S. Fujita, Jpn. J. Appl. Phys. 42, 7919 (2005)
44. M.-S. Mu, A. Azuma, T. Shiosaki, A. Kawabata, J. Appl. Phys. 62, 2482 (1987)
45. M. Wraback, H. Shen, S. Liang, C.R. Gorla, Y. Lu, Appl. Phys. Lett. 74, 507 (1999).
46. J. Zu’n˜iga-Pe’rez, V. Mun˜oz-Sanjose’ , E. Palacios-Lido’n, J. Colchero, Phys. Rev. Lett. 95, 226105 (2005).
47. J.-M. Chauveau, P. Vennégués, M. Laügt, C. Deparis, J. Zuniga-Perez, and C. Morhain, J. Appl. Phys. 104, 073535 (2008)

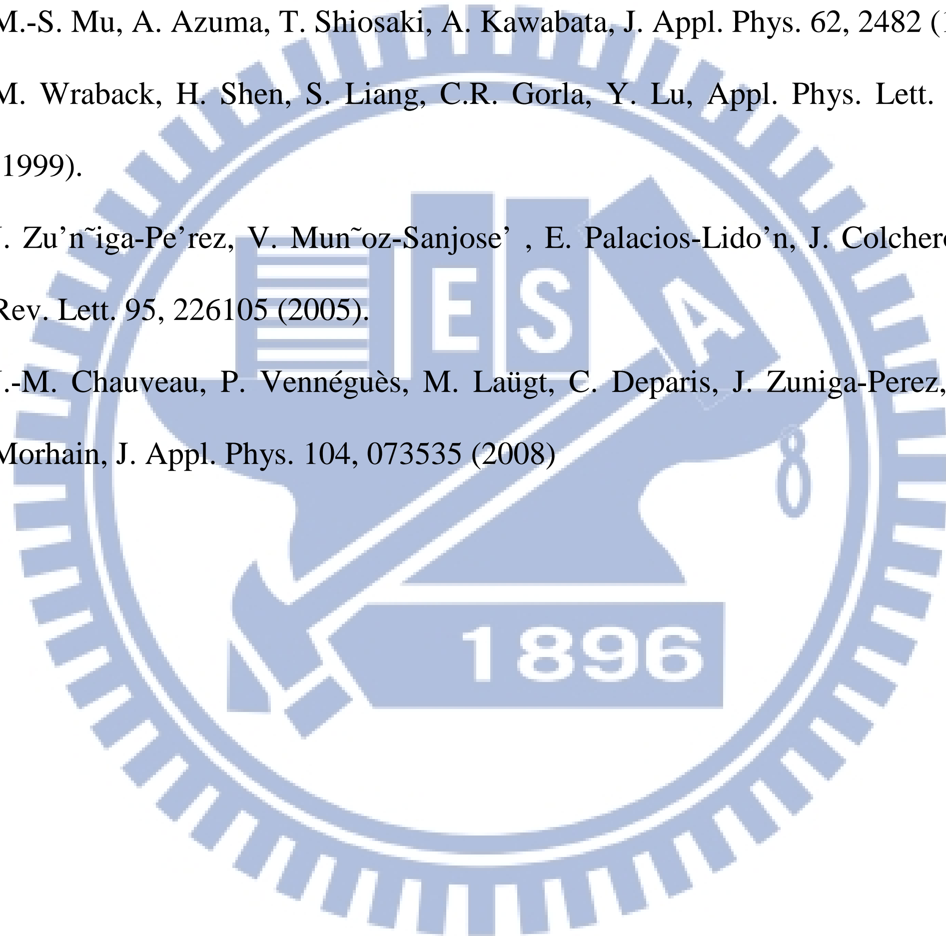

Chapter 2 Theoretical background of experimental methods

In this chapter, theoretical background and equipment setup of laser-MBE growth method, crystal structures, fundamental optical transitions and lattice dynamics of ZnO are reviewed. The crystal structures have been analyzed by X-ray diffraction and transmission electron microscopy, which are powerful techniques to measure crystalline structure, quality and defects. The atomic force microscope is used to observe the morphology of samples. Optical transitions in ZnO have been studied by a variety of experimental techniques such as optical reflection and photoluminescence (PL). Lattice dynamics corresponding to the selection rules and lattice vibrational properties are discussed. The principles and equipments of these characterization techniques are described.

2.1 System and principle of laser-MBE

2.1.1 Principle of laser-MBE

Laser-molecular beam epitaxy (laser-MBE), which is also called the pulsed-laser deposition (PLD), use high energy and short pulse-width laser beam to focus on the target to generate plasma. Schematic diagram of laser-MBE system is shown in Fig. 2-1. High power laser pulses vaporize the target material through formation of plasma plume with high kinetic energy by the absorption of laser energy. The ablated target material is deposited on a substrate to form a thin film. The laser-deposition processes involve the evaporation of the target material, the formation of high-temperature plasma from absorbing the laser energy by the evaporated material, and the expansion of the plasma resulting in deposition of thin films that will be considered in below.

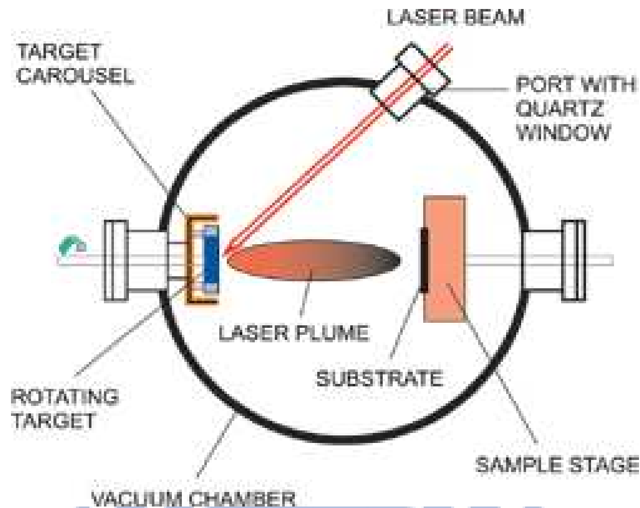

Fig. 2-1 Schematic diagram of Laser-MBE system

Depending on the different kinds of interaction between the laser beam and the target material, the laser deposition processes can be typically classified into three separate regimes: (1) evaporation of the surface layers of target material resulting from the interaction between the target material and the laser beam; (2) an isothermal plasma formation and expansion resulting from interaction between the evaporated material and the incident laser; and (3) anisotropic adiabatic expansion of the plasma leading to the characteristic of the laser deposition [**1**]. Each of the three regimes is considered separately in detail in the following.

(1) Interaction between the target and the laser beam

When a high power density excimer-laser pulse indicated at nanosecond impinges on the target, heating and evaporation the target material occurs in the beginning of the pulse. The amount of evaporated flux varies linearly with the pulse energy.

(2) Interaction between the evaporated material and laser beam

As the evaporated material is further heated by the interaction of the laser beam, the high-temperature plasma plume will be generated which consists of ions, atoms, molecules, and electrons. The plasma temperature is determined the power density,

frequency and pulse duration of the used laser beam as well as the thermal properties of the materials. During the laser pulse duration, the isothermally expanding plasma constantly increases at its inner surface with evaporated particle from the target. The velocities of acceleration and expansion in this region depend on the initial velocities of the plasma. Due to the large lateral dimensions of the plasma, this expands preferential to the irradiated surface normally.

(3) Anisotropic adiabatic expansion of the plasma and deposition process

After the termination of the laser pulse, the plasma expands adiabatically with its initial dimensions. The plasma cools rapidly during the expansion process, with the edge velocity reaching asymptotic value. The particles from the expanding plasma strike the substrate and form a thin film with characteristic spatial thickness.

2.1.2 Description of laser-MBE system

Our laser-MBE system consists of a load-lock chamber and a deposition chamber as shown in Fig. 2-2 and a KrF excimer laser (Lamda Physics LPX 210i) with 24 ns pulse duration and repetition rate of 1-100 Hz as the ablation light source. The samples are loaded from the load-lock chamber through a gate valve to main chamber using a magnetically transfer arm. The deposition chamber designed for PLD contains a target manipulator, a substrate manipulator and entrance ports for laser injection, vacuum and pumping system (gauges, scroll and turbo pump), gas inlet system and cool-water system, etc. The scroll pump and the turbo pump are used to achieve high vacuum pressure (< 10^{-8} torr). The substrate was mounted on a Mo-substrate holder. The substrate holder can be transferred from load-lock chamber into the deposition chamber by the transfer arm and the substrate can be picked up from the load-lock chamber by the manipulator through rotating, pushing and pulling.

LMBE has the advantages of ultra-clean, simplicity, without corrosive gas, and achieving high-quality epitaxial films at a relatively low growth temperature (500℃) due to its high kinetic energy (10eV—100eV) of laser ablated species [**2**]. Besides, the source of Zn and O can be obtained directly from the high quality ZnO (5N) target in LMBE, i.e., no extra oxygen supply is necessary.

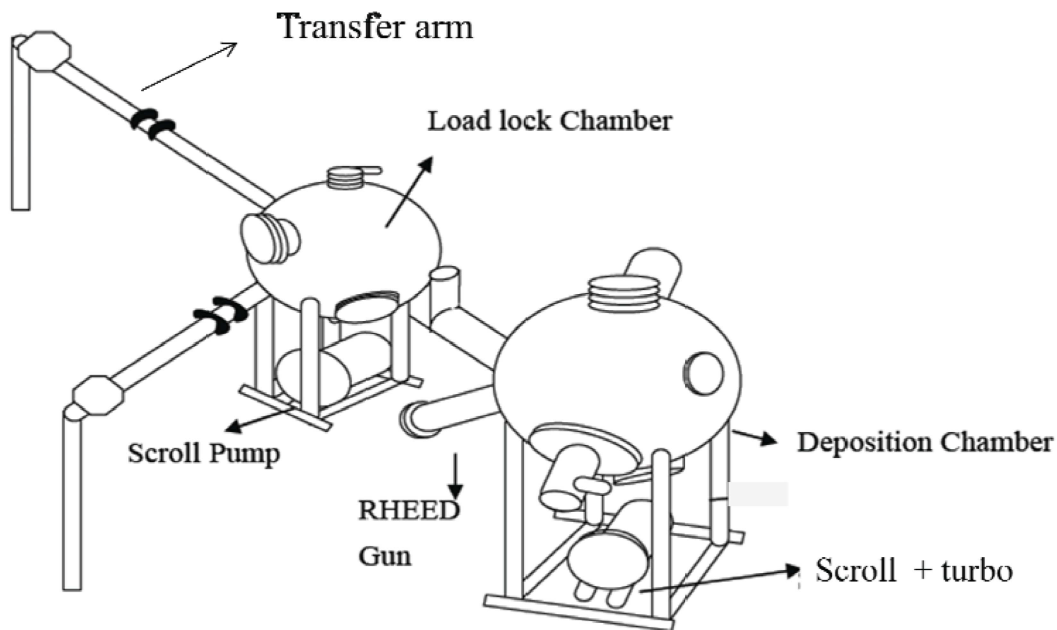

Fig. 2-2 Layout of laser-MBE

2.2 Epitaxy

Epitaxy refers to the growth on a crystalline substrate of a crystalline substance that mimics the orientation of the substrate. Film is deposited on a substrate of the same compositions, the process is called homoepitaxy; otherwise, it is called heteroepitaxy. Depending on the lattice mismatch, $(a_f - a_s)/a_s$, where a_f and a_s, respectively, denote the lattice constants of film and substrate, the epitaxy of heterosystems can be modeled by lattice match and domain match models [**3**].

2.2.1 Lattice match model (LMM)

The well-established lattice-matching model is suitable for describing systems with

small lattice misfit (less than 7%–8%). The epilayer is grown in use of one-to-one match of lattice constants across the film and substrate interface. The film grows arrive to a ''critical thickness'', where it becomes energetically favorable for the film to contain dislocations [**4, 5**]. In this condition, the dislocations are generated at the film surface and glide to the interface; therefore, the Burgers vectors and planes of the dislocations are dictated by the slip vectors and glide planes of the crystal structure of the film [**6**]. The smaller lattice misfit leads to the smaller elastic energy and coherent epitaxy is formed. Above this misfit, it was surmised that the film will grow textured or largely polycrystalline.

2.2.2 Domain match model (DMM)

The DMM concept represents a considerable departure from the conventional LME for hetero-systems with lattice misfit less than 7–8%. When larger lattice misfit in heteroepitaxy, the integer multiples of lattice planes - domains, instead of lattice constants, match across the film–substrate interface. The size of the domain equals the integer multiples of planar spacing in the DMM.

The c-plane ZnO grown on c-plane sapphire is an example of DMM [**7**]. The lateral lattice constants of ZnO and sapphire are 3.2495 and 4.758 Å, respectively, yielding a lattice mismatch of -31.7%. However, the *c*-plane of ZnO lies on the basal plane of sapphire with a 30° in-plane rotation to reduce the mismatching, which leads to the alignment of the $\left\{11\bar{2}0\right\}$ of ZnO with $\left\{30\bar{3}0\right\}$ of sapphire. The domain consisted of an average 5.5 ZnO $\left(11\bar{2}0\right)$ planes of ZnO with 6 or 7 $\left(30\bar{3}0\right)$ planes of sapphire at the interface, which equivalent to lattice constant of ZnO (8.935 Å) matches nicely with the domain made of an average 6.5 sapphire $\left(30\bar{3}0\right)$ (8.928 Å). The DMM reduce the lattice mismatch from -31.7% to 0.078%. Besides, the DMM

effect of ZnO growth on Si by high-K material was also observed [**8**].

2.3 X-ray diffraction

X-ray diffraction (XRD) is a usefully technique to characterize crystallographic structure and crystalline quality of the deposited films without destructing sample. The technique is basically a measurement of the diffraction intensity of x-ray, which interacts with sample as functions of incident and scattered angles, polarizations, and wavelength or energy.

2.3.1 Theory of X-ray diffraction

X-ray diffraction is used to determine the geometry or shape of a molecular. In 1913, W. L. Bragg developed the theory of XRD based on the elastic scattering of x-rays through structures that have long range. Regular arrangements of atoms make up the crystal; each atom owns different abilities to scatter electromagnetic waves. A monochromatic beam of X-ray that impinges on a crystal will be scattered in all directions, the spatial distribution of the scattered intensity bears the information about the atomic arrangement of the probed material.

For a crystalline material, the structural information can be determined by analyzing the scattered X-rays by crystal atoms to undergo constructive interference can be obtained as in Fig. 2-3. In the plane wave description, a beam containing X-ray of wavelength λ impinges on a crystal at an angle θ with neighboring atomic planes with spacing of d in the crystalline material. The path differences of incident and reflected X-rays must be $n\lambda$, where n is an integer, interfere constructively condition will be worked. There are two conditions in the XRD. One condition is that their common scattering angle is equal to the angle of incidence θ of the original beam, the other is that the geometry arrangement meets the condition for the Bragg's

law:

$$n\lambda = 2d \sin \theta \,, \quad (2\text{-}1)$$

where n is an integer, λ is the wavelength of X-ray and θ is the angle between incident X-rays and reflecting planes. In other words, the constructive interference occurs only when the path between the rays scattered by the consecutive crystalline planes differs by exactly λ, 2λ, 3λ, and so on.

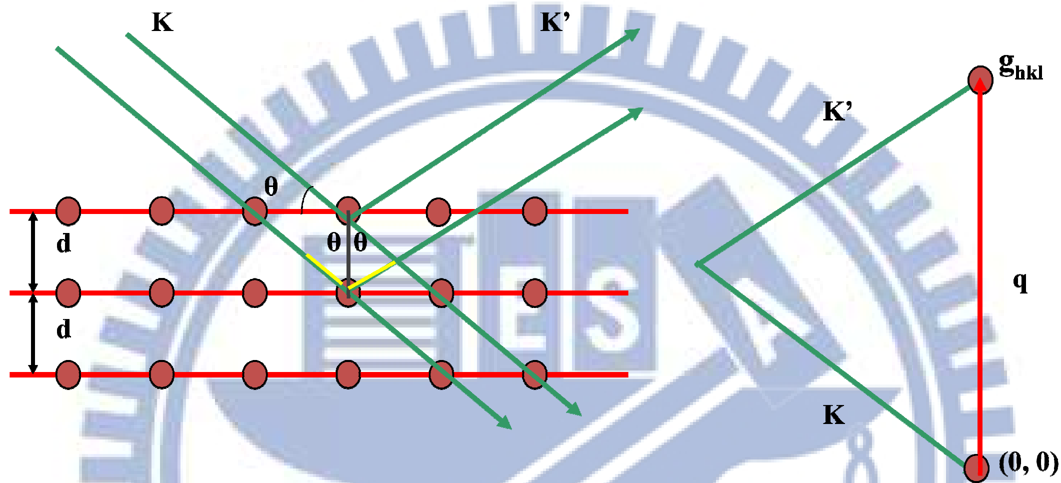

Fig. 2-3 X-ray scattering from a cubic crystal

In the elastic scattering process, the wave vectors of the incident and scattered X-ray, denoted by k and k', respectively, both have the magnitude of $2\pi/\lambda$, and the scattering vector q is defined by the equation: $q \equiv k' - k = 2k\sin\theta$. Each set of periodical parallel planes with inter-planar spacing d in real space can be indexed by the Miller indices (hkl), which is associated with a lattice vector g_{hkl} in reciprocal space with the magnitude $|g_{hkl}|$ equal to $2\pi/d_{hkl}$. When the condition of diffraction satisfies the Bragg's law, it means $q = 2\pi/d$. The ZnO crystal structure is hexagonal with lattice parameters, $a = 3.243$ Å and $c = 5.203$ Å ($\alpha = \beta = 90°$, and $\gamma = 120°$). The reciprocal lattice vector g_{hkl} of a hexagonal

lattice can be given as:

$$|g_{hkl}| = \frac{2\pi}{d_{hkl}} = \pi\sqrt{\frac{4}{3}\left(\frac{h^2+hk+k^2}{a^2}\right)+\frac{l^2}{c^2}}\,. \qquad (2\text{-}2)$$

In the hexagonal structure, the inter-planar spacing *d* is given as:

$$\frac{1}{d^2} = \frac{4}{3}\left(\frac{h^2+hk+k^2}{a^2}\right)+\frac{l^2}{c^2}\,. \qquad (2\text{-}3)$$

Combining the Bragg's law with (2-2):

$$\frac{1}{d^2} = \frac{4}{3}\left(\frac{h^2+hk+k^2}{a^2}\right)+\frac{l^2}{c^2} = \frac{4\sin^2\theta}{\lambda^2}\,. \qquad (2\text{-}4)$$

Conventionally, for crystals with hexagonal and rhombohedral symmetry, crystallographic planes are denoted using the four indices based on a four-axis Miller-Bravias coordinate system, which consists of three basal plane axes (a_1, a_2, a_3) at the angle $120°$ among them and a fourth axis c perpendicular to the basal plane. The Miller-Bravias indices (*hkil*) have to satisfy the condition: $i = -(h+k)$. In this thesis, 4-digit Miller-Bravias indices are used for materials with hexagonal and rhombohedral symmetries including ZnO and sapphire to distinguish them from those with cubic symmetry.

To determine the crystalline structural properties, a four-circle diffractometer is used which consists of four rotatable circles: θ, 2θ, χ and ϕ. The 2θ circle is the detector axis to control the magnitude of scattering vector *q*. The θ, χ and ϕ circles control the sample orientation. When the *q* vector coincides with the specific reciprocal lattice vector g, the Bragg condition is satisfied. The ϕ angle is equivalent to the azimuthal angle and the χ angle is related to the polar angle of the sample. Different types of scans can be performed to probe the properties in different aspects. The θ-2θ scan can observe the properties along the surface normal. The direction and spread of lattice tilting of the deposited film can be

observed through the θ rocking curve (ω scan), and then the ϕ scan could determine the direction and spread of lattice in the azimuth.

2.3.2 Radial scans

Radial scans collect scattered X-ray intensity while the scattering vector q is scanned along any of the radial directions in reciprocal space. Radial scan is performed by driving the two rotatable circles, θ and 2θ, shown in Fig. 2-4, to change the q vector with scanning the reciprocal space along the surface normal direction. The most commonly performed radial scan is the one along sample surface normal, which is often known as $\theta-2\theta$ or $\omega-2\theta$ scan as shown in Fig. 2-4. From the positions of diffraction peaks we can determine the corresponding interplanar spacing along the direction of q from the positions of diffraction peaks and it can probe the structural coherence length (grain size) and inhomogeneous strain along the same direction by the line width of the diffraction peak.

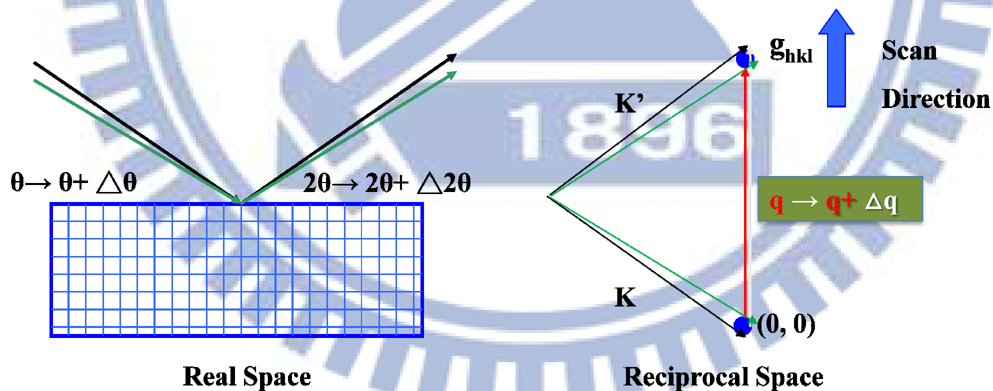

Fig. 2.4 X-ray diffraction $\theta-2\theta$ scan.

2.3.3 Rocking curve (ω scan)

For a given incident x-ray direction and detector position, the scattered x-ray is collected while the crystal is rotated by means of scanning the θ angle as illustrated in Fig. 2-5. The obtained intensity distribution ($\theta \pm \Delta\theta$) is called the "rocking curve

or ω scan''. The width of a rocking curve is a direct measurement of the width of the diffraction peak in the transverse direction, the $\Delta\theta$ bears the information of the orientation distribution of grains in a film, mosaicity; the wider the distribution leads to the larger $\Delta\theta$. Rocking curve performed at reflections along the surface-normal is sensitive to the distribution of tilt angle of the sample; on the other hand, the rocking curved measured at surface Bragg peaks mainly reflect the twist (azimuthal) angle distribution of the sample.

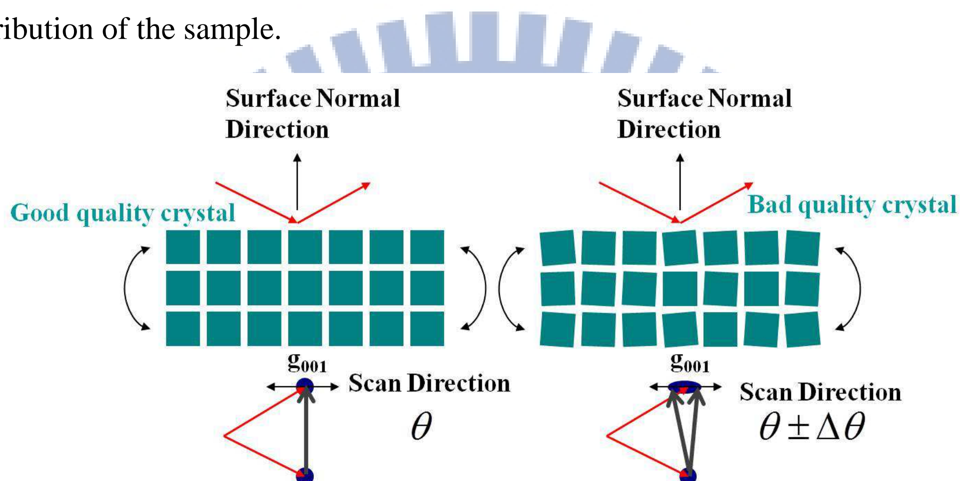

Fig. 2-5 X-ray diffraction rocking curve

2.3.4 Azimuthal scan

Azimuthal scan means measuring the diffraction intensity as a function of azimuthal angle ϕ by rotation the sample along an axis, which is usually parallel to surface normal or, in some cases, to a specific crystallographic axis, as illustrated in Fig. 2-6.

Using azimuthal scan, we can study the symmetry and crystal quality of the grown films and determine its relative orientation with respect to the substrate.

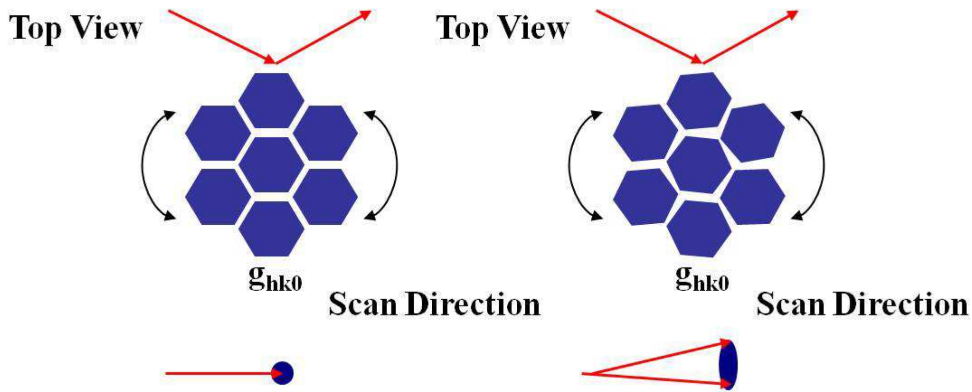

Fig. 2-6 X-ray diffraction azimuthal scan

2.4 Microscopy

2.4.1 Transmission electron microscopy (TEM) [9]

In the atomic scale level, TEM is a powerful and higher resolution tool to analyze the structure of a crystalline material and makes the direct observation of crystal defect possible. In practice, the diffraction patterns measured by x-ray methods are more quantitative and have better resolution than electron diffraction patterns, but to use electrons has an important advantage over x-ray: electrons can be easily focused to a small spot size (short de Broglie wavelength of electron) [**10**].

An image is formed from the interaction of the electrons transmitted through the sample; the image is magnified and focused onto an image device, like a fluorescent screen, on a layer of photographic film or CCD camera. TEM usually consists of the electron source, which is an electron gun connecting to a high voltage (typically about 100-300 kV) accelerating electronic filed and an assembly of magnetic lenses, the electron beam is focused to a spot of the order of 1 mm on the sample. According to the scheme in Fig 2-7, where the ray path diagrams are shown in the cases when an image or diffraction patterns (DP) are produced. The section below is a brief description of TEM technique.

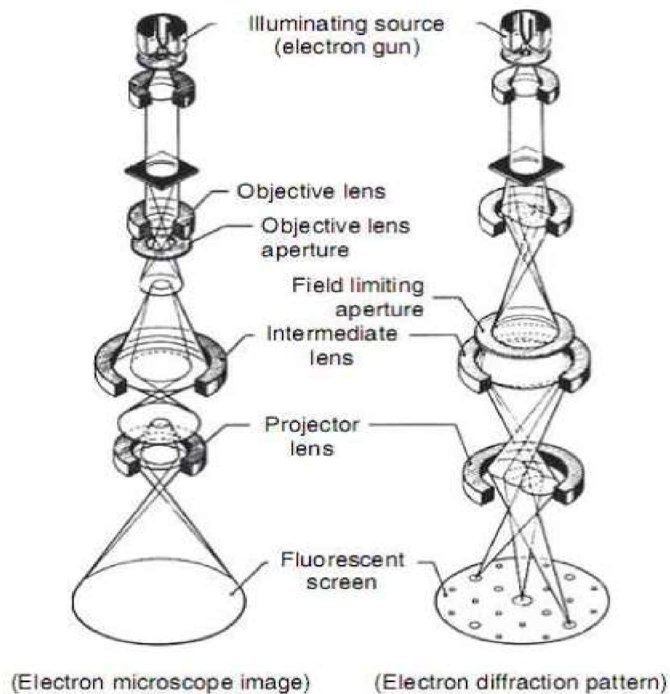

Fig. 2-7 Scheme of the lens assembly and the ray path diagram forming the image (left) or the diffraction pattern (right). [**11**]

2.4.1-1 Selected area electron diffraction (SAED)

Due to the wave-particle duality, electron beam can be considered as wave and is subjected to diffraction from periodic arrangement of atom layers. Selected area electron diffraction (SAED) is a crystallographic experimental technique, which selects an area of the sample and can be described as the first Fourier transformation of atoms arranged periodically. The crystalline sample is subjected to a parallel beam of high-energy electrons. The periodic atoms act as a diffraction grating to the electrons. The image on the screen of the TEM is thus an array of diffraction pattern, and each diffraction spot corresponds to a satisfied diffraction condition of the crystal structure. SAED can be used to identify crystal structure and to examine crystal defects. The sample holder is an objective aperture, which can be inserted into the beam path to block electron beam except for the selected diffraction spot shown in Fig.

2-8. By tilting the sample relative to the electron beam, we can choose the optimal geometry to satisfy the Bragg law for a specific reciprocal lattice vector $\bar{g}$. The electrons passing the objective aperture form the image on the screen and tilting the sample to satisfy specific diffraction vector $\bar{g}$, which is called the dark field (DF) images. In addition, the image formed by the unblocked spots including the direct beam and specific selected diffraction spots is called the bright filed (BF). Using the BF mode, the TEM image can be formed by only the selected spots with specific diffraction vector $\bar{g}$.

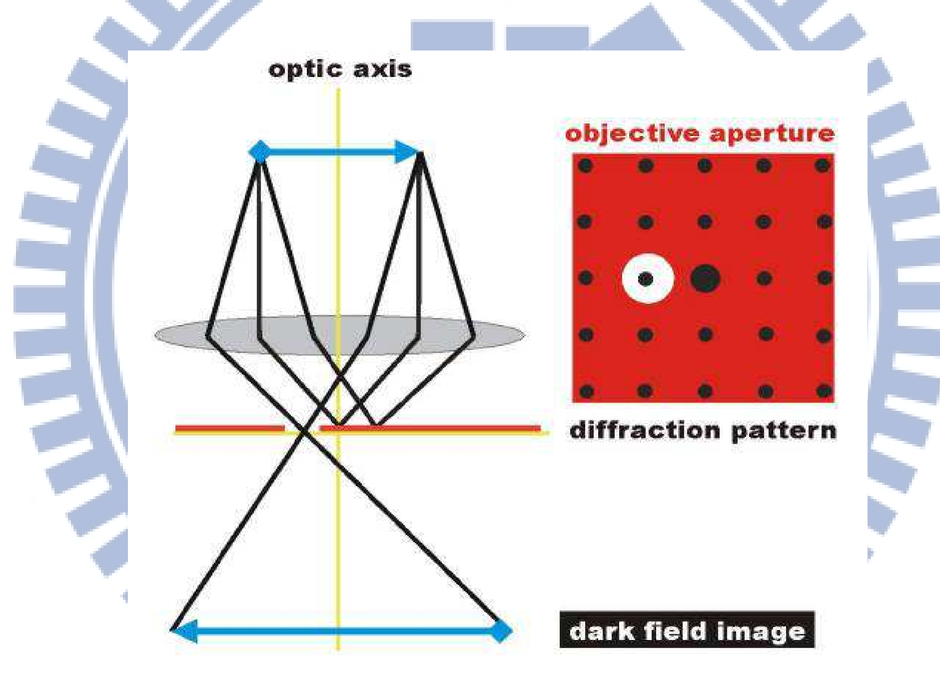

Fig. 2-8 Selected area electron diffraction (http://www.microscopy.ethz.ch/)

2.4.1-2 Two beam analysis

The inverse fast Fourier transformation (IFFT) of TEM SAED is the technology by electromagnetic lens. The image mode is often done by utilizing either the primary beam for bright field or any one of diffracted beams for dark field imaging. To obtain the best contrast image for threading dislocation and partial dislocation

(stacking faults) analysis, the "two-beam" case with only one "particular diffraction reflex" excited; i.e., the Bragg condition is only met for one diffraction vector *g*, is preferred.

Dislocations are visible or exhibit great contrast in IFFT of TEM SAED image along one diffraction vector if $\vec{g} \cdot \vec{b} \neq 0$, where $\vec{b}$ and $\vec{g}$ are the Burgers vector and the one diffraction vector which our observed. Used two-beam analysis by controlling the different diffraction vectors and observing the contrast, we can determine the dislocation types. The possible mechanisms of plastic relaxation in wurtzite material as a function of the initial strain states, the mechanisms responsible for the plastic relaxation in the structure have already been studied and the different slip systems and dislocations have been described in c-plane wurtzite heterostructures [**12, 13**].

2.4.2 Atomic force microscopy (AFM)

Atomic force microscope (AFM) or scanning force microscope (SFM) was invented by Binnig, Quate and Gerber in 1986. Similar to other scanning probe microscopes, the AFM raster scans a sharp probe over the surface of a sample and measures the changes in force between the probe tip and the sample shown Fig 2-9. Demonstrated resolution is on the order of fractions of a nanometer. AFM consists of a cantilever with a sharp tip (closed to nanometers), which is used to scan the sample surface. When the tip is brought into the vicinity of the sample surface, the force between the tip and the surface deflected results from the bending of the cantilever by an optical lever technique: a laser beam is focused on the back of a cantilever and reflected into a photodetector. For AFM, the measured forces include mechanical contact force, van der Waals force, electrostatic force, and magnetic force depending on the scanning modes. Additional quantities may be measured simultaneously through the use of specialized types of probe. The sample is

mounted on a piezoelectric device to move the sample along the z direction for scanning the sample.

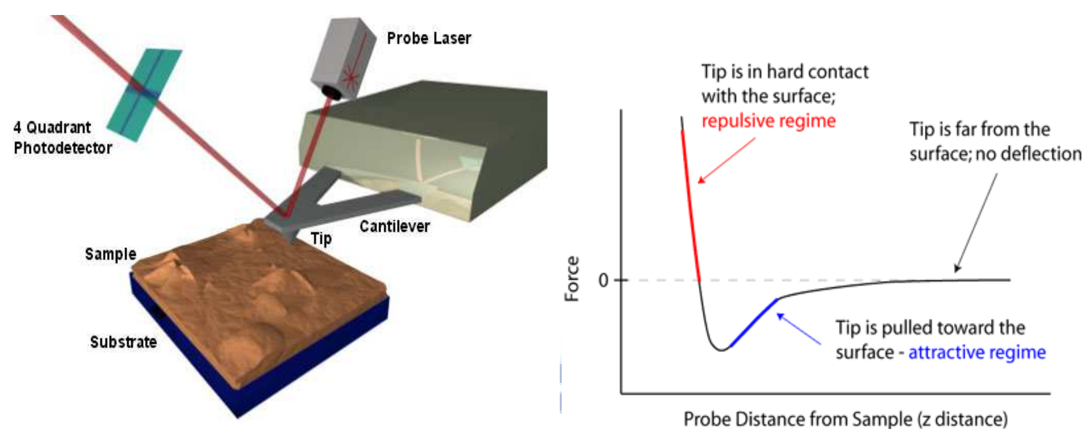

Fig. 2-9 Scheme of an atomic force microscope and the force-distance curve characteristic of the interaction between the tip and sample (http://www.nanoscience.com/education/afm.html).

There are three typical types of AFM imaging, which are:

(1) *Contact mode*: the most common method of operation of the AFM and is useful for obtaining 3D topographical information on nanostructures and surfaces. As the name suggests, the tip and sample remain in close contact as the scanning proceeds. However, the hard tip remaining in contact with the sample exists that large lateral forces may damage the surface of the sample.

(2) *Tapping mode:* Unlike the operation of contact mode, where the tip is in constant contact with the surface, in tapping mode the cantilever is driven to oscillate up and down at near its resonance frequency by a small piezoelectric element mounted in the AFM tip holder similar to non-contact mode. The amplitude of this oscillation is greater than 10 nm, typically near 100 nm. This method of "tapping" depresses the damage of the tip compared to the amount done in contact mode. Because the contact time is a small fraction of its oscillation period, the lateral forces are reduced dramatically. Tapping mode is usually preferred to image samples to improved lateral

resolution that are weakly bound to the surface or samples that are soft (polymers, thin films).

(3) *Noncontact mode*: The cantilever is oscillated above the surface of the sample at distance such that it is no longer in the repulsive regime but in the attractive regime of the inter-molecular force curve. The operation of non-contact imaging is quite difficult in ambient conditions because of the existing thin layer of water on the tip and the surface.

The choice different AFM mode is based on the surface characteristics of interest and on the hardness/stickiness of the sample. Contact mode is most useful for hard surfaces; a tip in contact with a surface, however, is subject to contamination from removable material on the surface. Excessive force in contact mode can also damage the surface or blunt the probe tip. Tapping mode is well suit for imaging soft biological specimen and for samples with poor surface adhesion (DNA and carbon nanotubes). Non-contact mode is another useful mode for imaging soft surfaces.

2.5 Fundamental optical characterizations

2.5.1 Photoluminescence (PL) characterization

Photoluminescence (PL) is a process in which a substance absorbs photons and then re-radiates photons. In quantum mechanics, this can be described as an excitation to a higher energy state and then a return to a lower energy state accompanied by the emission of a photon. The energy of the emitted photons is thus related to the difference in energy levels between the two energy states involved in the transition between the excited state and the equilibrium state. Available electronic states and allowed transitions between states are determined by the rules of quantum

mechanics. PL spectrum can be used not only to measure the electronic transition but also to identify the impurity types or defects. Existence of impurities and defects in the samples produces characteristic spectral features. In addition, the line width of each PL peak is an indication of sample quality, even though such analysis has not yet become highly quantitative [**14**]. PL is a nondestructive method of probing the electronic structure of materials and has become an important technique for the semiconductor industry owing to its powerful and sensitive ability to characterize impurities and defects in semiconductors, which affect material quality and device performance.

2.5.1-1 General concept of PL [15, 16]

PL emission requires that the system be in a nonequilibrium condition and photo-excitation is adapted to produce the hole-electron pairs in semiconductors. The electronic ground state of a perfect semiconductor consists of completely filled valance band and completely empty conduction band. If we start from the above-defined ground state and excite one electron to the conduction band, we simultaneously create a hole in the valance band. In this sense, an optical excitation is considered as a two-particle transition. The same argument holds for the recombination process. An electron in the conduction band can return radiatively or nonradiatively back to the valance band only if there is a free space, i.e., a hole, available there. Two quasi-particles annihilate in the recombination process. The optical properties of a semiconductor can thus be described in terms of the excited states of an N-particle problem. The quanta of these excitations are called excitons, which are further classified into Frenkel exciton and Wannier exciton according to the spatial distribution of their associated wavefucntions. These so-called Frenkel excitons cannot be described in the effective mass approximation. For Wannier

excitons, their Bohr radii, defined as the mean distance between electron and hole, are larger compared to the lattice constant. This condition is met in most II-VI, III-V, and column IV semiconductors. Thus, we will focus on the Wannier excitons in this work.

Based on the effective mass approximation, the system of an electron-hole pair can be treated as a hydrogen-like problem with Coulomb potential $\frac{-e^2}{4\pi\varepsilon|r_h - r_e|}$. Excitons in semiconductors form, to a good approximation, a hydrogen-like series of states below the gap. Using the ground state and excited state energies and assuming that the exciton has a hydrogen-like set of energy levels, the exciton binding energy can be calculated from

$$E_{ex}(n,k) = E_{gap} - \frac{E_B}{n^2} + \frac{(\hbar k)^2}{2M}, \tag{2-5}$$

where n is the principal quantum number, E_B is the exciton binding energy, $M = m_e + m_h$, and $k = k_e + k_h$ are translational mass and wave vector of the exciton, respectively. E_B can also be expressed in terms of the low-frequency dielectric constant ε_0 and the reduced exciton mass μ_{ex} as

$$E_B = \frac{e^4 \mu_{ex}}{2\hbar^2 \varepsilon_0^2} = 13.6 \frac{\mu_{ex}}{\varepsilon_0^2}, \quad \mu_{ex} = \frac{m_e m_h}{m_e + m_h}. \tag{2-6}$$

In this section, a brief review on the characteristic features from bulk ZnO in a typical low temperature PL spectrum. Including the high energy side of the bound excitons, free exciton transitions appear with the A-, B- and C-valence band positioned above 3.37 eV, various bound exciton recombination at near band edge (excitons bound to neutral donors or acceptors) followed by longitudinal optical (LO) phonon replicas with an energy separation of 72 meV. At lower energies from 3.34

to 3.31 eV two-electron satellite (TES) recombination of the neutral donor bound excitons are observed. Then, donor-acceptor-pair (DAP) transition at ~3.22 eV followed by phonon replicas again, green, yellow, and intrinsic defect emissions are also discussed.

2.5.1-2 Free excitons

The optical properties of a semiconductor are connected with both intrinsic and extrinsic effects. The intrinsic excitonic transitions in PL measurement are typically in the 3.376–3.450 eV range. The wurtzite ZnO conduction band is mainly constructed from the *s*-like state having Γ_7^c symmetry, whereas the valence band (VB) is a *p*-like state, which is split into three bands due to the influence of crystal field and spin-orbit interactions [**17, 18**]. The optical intrinsic absorption and emission spectra are therefore dominated by transitions involving these three valence bands (VBs) and the conduction band (CB) that relate the free-exciton transitions from the CB to these three VB labeled by A- (heavy hole), B- (due to the light hole), and C-band (due to the crystal-field split) usually. The band diagram for the zinc blende and the wurtzite ZnO structures is shown in Fig. 2-10, the three VB, A-, B- and C-, for wurtzitic ZnO are denoted Γ_9, Γ_7, and Γ_7, respectively [**18**]. In previous reports, the three VB symmetry, A-Γ_9, B-Γ_7, and C-Γ_7, in ZnO are observed intrinsic exciton transitions in low temperature PL, magnetoluminescence and reflectance measurements [**19-23**].

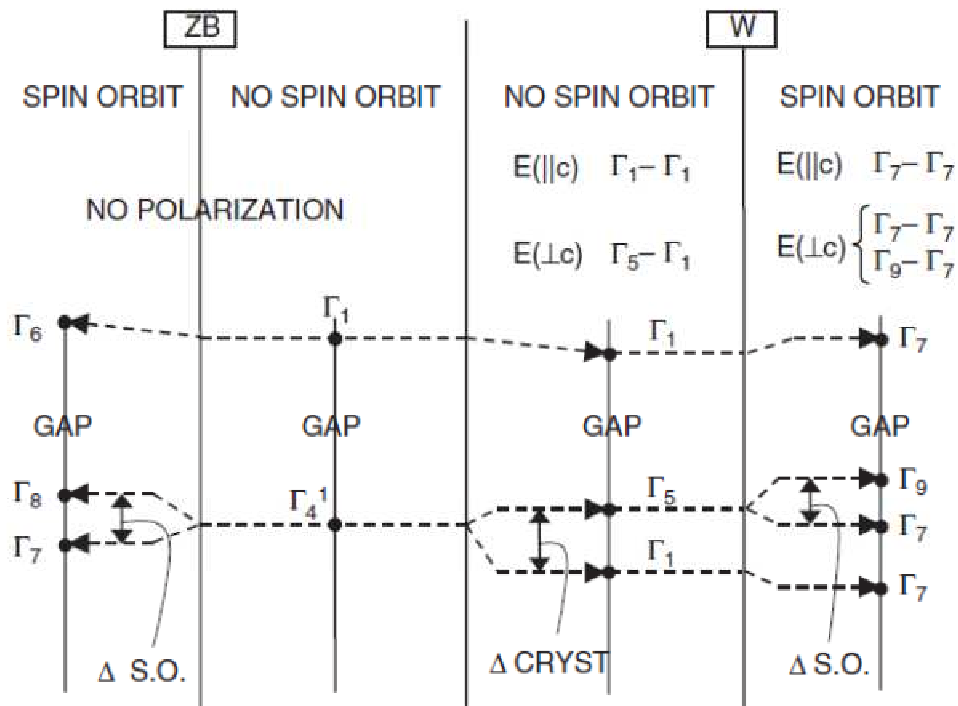

Fig. 2-10 Band structure and selection rules for ZB and W structures. Crystal field and spin-orbit splitting are indicated schematically. Transitions rules, which are allowed for various polarizations of electric field vector with respect to the *c*-axis, are indicated [**18**].

Group theory arguments and the direct product of the group representations of the band symmetries (Γ_7 for the CB, Γ_9 for the A-VB, upper Γ_7 for B-VB, and lower Γ_7 for C-VB) result in the following intrinsic exciton ground states symmetries:

$$\Gamma_7 \times \Gamma_9 \rightarrow \Gamma_5 + \Gamma_6 \, , \quad \Gamma_7 \times \Gamma_7 \rightarrow \Gamma_5 + \Gamma_1 + \Gamma_2 \, .$$

The Γ_5 and Γ_6 exciton ground states are both doubly degenerate, whereas Γ_1 and Γ_2 are both singly degenerate. The free exciton transitions of wurtzite structure should follow the selection rules: Γ_5 and Γ_1 are allowed transitions with $\vec{E} \perp \hat{c}$ and $\vec{E} \parallel \hat{c}$ polarizations, respectively, where $\vec{E}$ is the electric field of incident light

and $\hat{c}$ denotes the crystallographic c-axis, but the Γ_6 and Γ_2 are forbidden. Figure 2-11 shows the selection rules of transitions for wurtzite ZnO follow the specially polarized optical transitions at 4.2K [**24**].

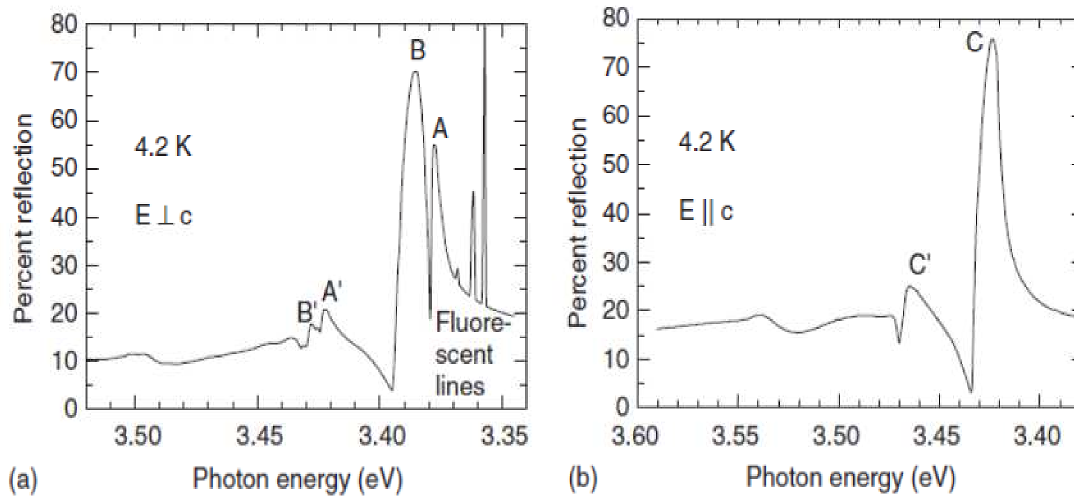

Fig. 2-11 Reflection spectra from ZnO at 4.2K for (a) $\vec{E} \perp \hat{c}$ and $\vec{E} \parallel \hat{c}$. [**24**]

The different excited conditions ($\vec{E} \perp \hat{c}$ or $\vec{E} \parallel \hat{c}$) reflect different optical transitions (A-, B- or C-excitons) from ZnO, furthermore, the different transition bands exist different excitonic absorption features. The different absorption coefficients of A-, B- and C-excitons were reported in Ref. **25**. Figure 2-12 shows the A- and B-excitons, which have stronger absorption coefficient than C-exciton that implies in the same pumping condition the excited A- and B-excitons could generate more photon numbers than C-exciton.

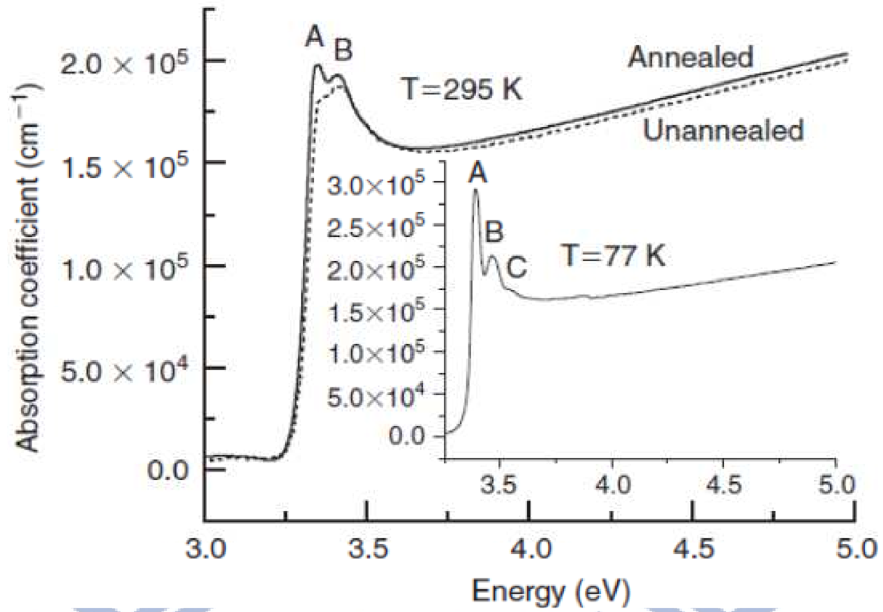

Fig. 2-12 Absorption coefficient of ZnO for annealed (solid lines) and without annealed (dotted line) shows at room temperature. The inset shows the absorption coefficient for the annealed sample at 77 K. [**25**]

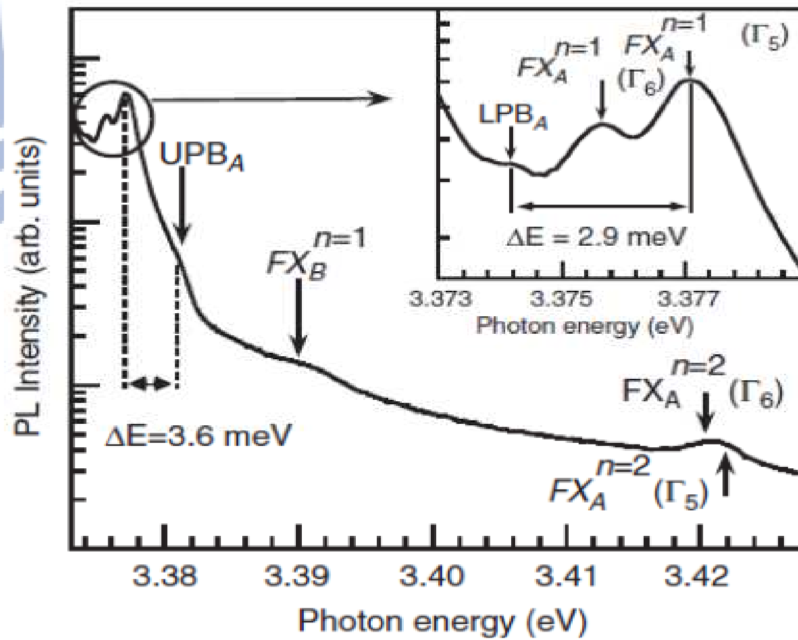

Fig. 2-13 Free excitonic fine structure region of the PL spectrum at 10K for a ZnO substrate. [**26**]

For unpolarized light, ground and first excited states of free A- and B-excitons

along with a weak C-excitons feature are observed at $FX_A^{n=1} = 3.377$, $FX_B^{n=1} = 3.390$ and $FX_C^{n=1} = 3.433$ eV, respectively [**26**]. The position of the first excited state $FX_A^{n=2} = 3.421$ eV and thereby the binding energy of the free A-excitons (~ 60 meV) were also confirmed by reflectivity spectra. Additionally, the reflection minima at 3.427 eV and 3.433 eV were assumed related to the second and the first excited states of the free A- and B-excitons, respectively. The PL spectrum range above 3.373 eV at 10K in the $\vec{E} \perp \hat{c}$ polarization geometry for a high quality ZnO crystal is shown in Fig. 5-13. The free A-excitons are observed at $FX_A^{n=1} = 3.3771$ eV and $FX_A^{n=1} = 3.3757$ eV for Γ_5 and Γ_6 band symmetry, respectively, associated first excited state emissions are observed at $FX_A^{n=2} = 3.422$ eV and $FX_A^{n=2} = 3.4202$ eV. Although exciton emissions should be forbidden at k = 0 in the adapted experimental polarization condition, they are still observed. This could be attributed to the finite momentum of the photons. Geometrical effects such as not having the sample orientation exactly perpendicular to the electric field may be another reason for observing transition. According to the energy difference between the ground state and the excited state peak positions, the exciton binding energy and band gap energy can be derived. The energy difference of about 45 meV gives free A-excitons binding energy of 60 meV and band gap energy of 3.4371 eV at 10 K. Based on the reported energy separation of the free A- and B-excitons (in the range of 7.5–13 meV) [**19, 26**, **27**], we assigned the weak emission centered at 3.3898 eV, which is about 12.7 meV apart from the A-excitons, to the B-excitons transition. The energy of crystal field between free A- and C-excitons is around 45 meV [**19**, **24**, **28**].

2.5.1-3 Bound excitons and Two-electron satellites [26]

There are a few imperfections in the high quality crystals, such as ion vacancy, interstitials and substitutional atoms (either native or intentionally introduced) exist with a density less than 10^{12} cm^{-3}. Similar to the way that free carriers can be bound to (point-) defects, it is found that excitons can also be bound to defects as shown in Fig. 2-14. A free hole can combine with a neutral donor to form a positively charged excitonic ion. In this case, the electron bound to the donor still travels in a wide orbit around the donor. The associated hole moves in the electrostatic field of the "fixed" dipole, it is determined by the instantaneous position of the electron, it also travels about this donor. Therefore, this complex is called a "bound exciton". Bound excitons are extrinsic excitations related to dopants, native defects, or complexes, which usually generate various electronic states in the band-gap, and therefore influence both optical absorption and emission processes. The binding energy of the excitons bound to defects are often quite small, typically a few ten meV. Therefore, the bound excitons are observed at low temperature resulting from small binding energy. A basic assumption in the description of the bound excitons states for neutral or charged donors and acceptors binding excitons is a dominant coupling of the like particles in the bound exciton states. In high quality ZnO bulk, the shallow neutral donor- (acceptor-) bound excitons (D^0X or A^0X) often dominate because of the presence of donors or acceptors due to intrinsic and doped impurities or shallow donor-(acceptor-)-like defects. The recombination of bound excitons gives rise to sharp lines with a photon energy characteristic of each defect. Many sharp donor- and acceptor-bound exciton lines were observed in the LT-PL spectra of ZnO in a narrow energy range between 3.348 and 3.374 eV, as seen in Fig. 2-15.

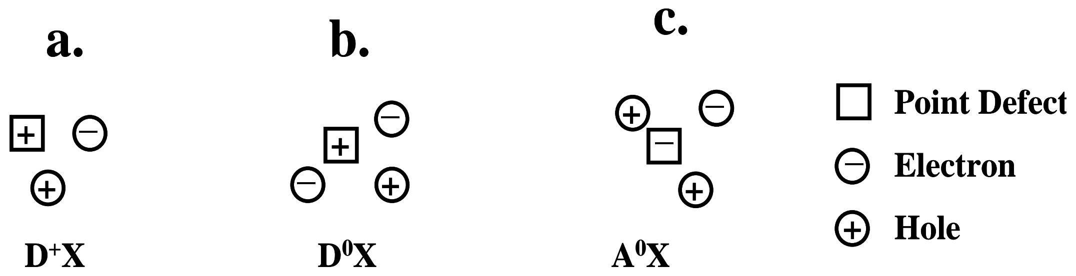

Fig. 2-14 Free carriers bound to point defects.

The outstanding peaks at 3.3598 ($D_1^0X_A$), 3.3605 ($D_2^0X_A$), 3.3618 ($D_3^0X_A$), 3.3650 ($D_4^0X_A$), and 3.3664 ($D_5^0X_A$) eV are defined to the A-excitons bound to neutral donors. Based on the energy separation between $FX_A^{n=1}(\Gamma_5)$ and the D^0X peaks, the binding energies of the D^0X associated with different donors, in the range of 10 to 20 meV, can be derived. On the high-energy side of the neutral D^0X, transitions between 3.3664 and 3.3724 eV have been attributed to the excited states or excited rotator states of the neutral-donor-bound excitons. These excited states are analogous to the rotational states of the H molecule. In the lower energy side of the PL spectrum, A^0X at 3.3564 ($A_1^0X_A$), 3.353($A_2^0X_A$), and 3.3481 eV ($A_3^0X_A$) are also observed that due to acceptor-bound exciton emissions. Relatively strong emission line at 3.3724 eV is attributed to the transition due to the B-free exciton bound to the same main neutral donor ($D_2^0X_B$). The energy separation between this peak and the main peak at 3.3605 eV (I_6) is around 12 meV, which is consistent with the energy splitting of the A- and B-excitons.

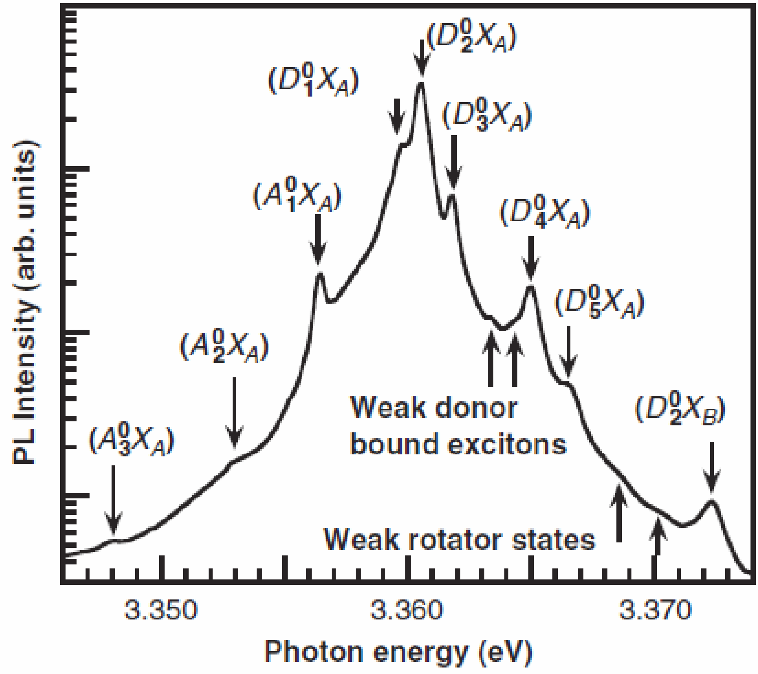

Fig. 2-15 Bound excitonic region of the 10K PL spectrum for a forming gas annealed ZnO substrate. [**26**]

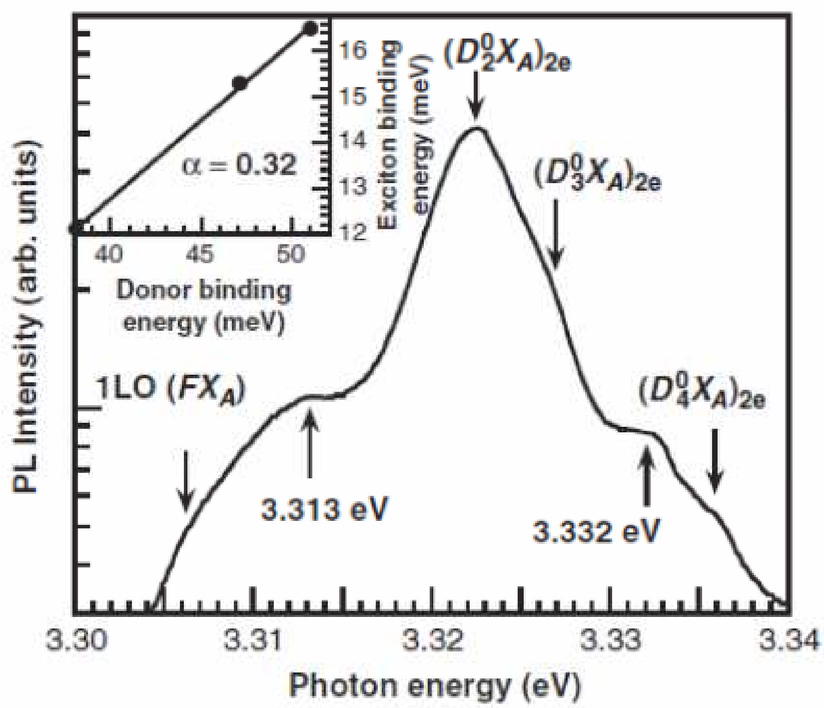

Fig. 2-16 PL spectrum at 10K for ZnO substrate in the TES region of the main bound exciton lines. Inset shows the donor binding energy is proportional to the exciton binding energy. [**26**]

The 3.3660–3.3665 eV transition along with the 3.3674 eV transition have also been attributed to the ionized donor bound exciton complexes, based on the splitting in magnetic field [**29**]. An increase in the intensity of the 3.3605 eV (I_6) emission line with increased Al concentration in ZnO based on the Al-implantation indicates that the I_6 transition is attributed to the Al impurity [**30**]. The 3.3598 eV(I_8) neutral donor bound exciton line was observed to be prominent in Ga-doped epitaxial ZnO films reported Ga-donor bound exciton recombination [**29**]. The 3.3564 (I_9) and 3.3530 eV (I_{10}) emission lines were thought related to Na and Li impurities, since they were typically observed in films doped with these elements [**31**].

When another free electron is bound D^0X to the excited-state is called the two-electron satellite (TES) transition in the spectral region of 3.32–3.34 eV. These transitions involve optical recombination of an exciton bound to a neutral donor, leaving the donor in the excited state, thereby leading to a transition energy which is less than the D^0X energy by an amount equal to the energy difference between the first excited and ground states of the donor. The energy difference between the ground-state D^0X and its TES state (excited states) determines the donor binding energy and catalog the different species present in the material. When the central cell corrections are also neglected, the donor excitation energy from the ground state to the first excited state equals to 3/4 of the donor binding energy, E_D.

The two-electron satellite (TES) transitions region is shown in Fig. 2-16 for bulk ZnO sample. The strong peak and its shoulder at 3.3224, 3.3268 and 3.3364 eV are the TES peaks, $(D_2^0X_A)_{2e}$, $(D_3^0X_A)_{2e}$ and $(D_4^0X_A)_{2e}$, associated with the stronger neutral donor bound exciton, the excited state of the donor whose ground state emission $D_3^0X_A$ and the neutral donor whose ground state $D_4^0X_A$. The energy

separation between the ground state and the corresponding excited states, the regions of donor binding energies are calculated as 38-51 meV.

In addition, the energy separation between TES and correspond to D^0X follow the empirical Haynes rule. Teke *et al*. [**26**] from the energy difference between the free exciton and the ground-state D^0X determined the localization energies as 16.6 meV (for 3.3605 eV), 15.3 meV (for 3.3618 eV), and 12.1 meV (for 3.3650 eV). According to the Haynes rule, the binding or localization energy of the D^0X is proportional to the binding energy of the corresponding donor, $E_{loc} = \alpha E_B$. They gave a Haynes' proportionality constant, $\alpha = 0.32$, which is closed to the other reports [**22, 32**].

2.5.1-4 Donor-acceptor pair (DAP) and LO-phonon replicas

The spectral region of 2.95-3.32 eV containing the donor-acceptor-pair (DAP) and LO-phonon replicas of the corresponding transitions from ZnO at 10K is shown in Fig. 2-17. LO-phonon replicas noted with separation of 71–73 meV due to the LO-phonon energy of ZnO [**33**]. The position at 3.306 eV labeled by 1LO (FX_A) approximately matches the expected value for the 1LO-phonon replica of the free exciton peak (~72 meV apart from the FX_A peak). The second and third order LO phonon replicas of FX_A labeled by 2LO (FX_A) and 3LO (FX_A), respectively, are very weak in the PL spectrum, as marked by upward arrows. Resolving the second and higher order LO replicas is even harder because the energy position (3.218–3.223 eV) falls in the spectral region where the donor-acceptor pair (DAP) transition and its LO phonon replicas are expected to appear (will be described in the following section). In fact, the radiative recombination peak at 3.217 eV is attributed to the

DAP; its first, second, and third LO-phonon replicas also show at 3.145, 3.073, and 3.001 eV, respectively. Two close peaks at 3.2898 and 3.2920 eV can be barely resolved, those are about 72 meV below the D^0X lines at 3.3605 and 3.3650 eV and assigned as the first LO-phonon replicas of the corresponding D^0X. The weak interaction between optical phonons and donor-related bound excitons makes LO-phonon replicas expected to be roughly two orders of magnitude less intense than the D^0X lines. The relatively broad peak is the first LO-phonon around 3.280 eV replica associated with the most intense A^0X line (3.3564 eV). The first, second, and third order LO-phonon replicas of the TES are also clearly observed in the PL spectra, those positioned at 3.252 3.182, and 3.112 eV are labeled as 1LO, 2LO, and 3LO-TES, respectively.

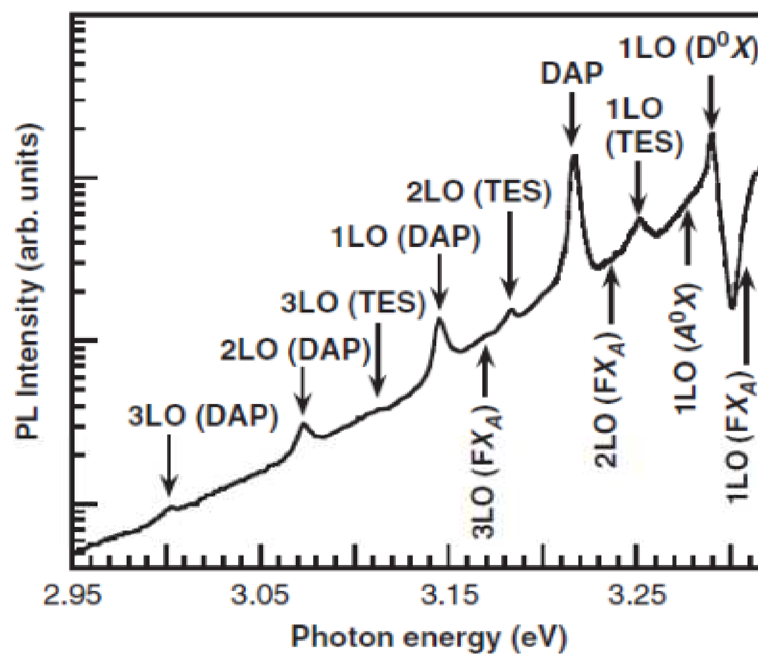

Fig. 2-17 PL spectrum for ZnO substrate at 10K in the region where donor-acceptor pair transition and LO-phonon replicas are expected to appear. [**26**]

2.5.1-5 Defect emissions [34]

In ZnO material, there are some native point defects, oxygen vacancies (V_O), zinc

interstitials (Zn_i), zinc vacancies (V_{Zn}) and oxygen interstitials (O_i). Oxygen vacancies (V_O), which have most often been cited as the cause of unintentional doping, are deep rather than shallow donors observed green luminescence and have high formation energies in ZnO. Zinc interstitials (Zn_i) are shallow donors, but they also have high formation energies in undoped ZnO. Zinc vacancies (V_{Zn}) are deep acceptors and probably related to the frequently observed green luminescence. Oxygen interstitials (O_i) have high formation energies; they can occur as electrically neutral split interstitials in *p*-type materials or as deep acceptors at octahedral interstitial sites in *n*-type ZnO. V_O and Zn_i have most often been mentioned as sources of *n*-type conductivity in ZnO.

The nature of the green-band luminescence appearing, centered between 2.4 and 2.5 eV, in undoped ZnO usually is attributed to the V_O as the defects. The green-band with a characteristic fine structure is most likely related to copper impurities, whereas the structureless green band with nearly the same position and width may be related to a native point defect such as V_O or V_{Zn} [**35-38**].

2.5.2 Raman scattering measurement

Raman scattering is an inelastic scattering process. When laser encountered the material the interaction inelastically with vibration (phonon) modes and produces outgoing photons which have an energy shift different from the incoming corresponding to phonon energy are called Raman scattering photons. All the Raman modes energies, intensities, line shape and width, as well as polarization behavior can be used to characterize the lattice and impurities.

2.5.2-1 Crystal structures [39]

ZnO is a II-VI compound semiconductor whose ionicity resides at the borderline

between covalent and ionic semiconductor. The crystal structures shared by ZnO are wurtzite, zinc blende, and rocksalt. At ambient conditions, the thermodynamically stable phase is wurtzite. The wurtzite structure has a hexagonal unit cell with two lattice parameters, *a* and *c*, in the ratio of *c*/*a*=1.633 and belongs to the space group of C_{6v}^{4} or $P6_{3mc}$. A schematic representation of the wurtzitic ZnO structure is revealed in Fig. 2-18. The structure is composed of two interpenetrating hexagonal-close-packed sub-lattices, each of which consists of one type of atom displaced with respect to each other along the threefold c-axis by the amount of *u*=3/8 in fractional coordinates (the *u* parameter is defined as the bond length or the nearest-neighbor distance parallel to the *c* axis). Each sublattice includes four atoms per unit cell, in which everyone atom of one kind (group-II) is surrounded by four of the other kind (group VI) or vice versa, coordinating at the edges of a tetrahedron. In a real ZnO crystal, the wurtzite structure deviates from the ideal arrangement, by changing the *c/a* ratio or the *u* value. It should be pointed out that a strong correlation exists between the *c/a* ratio and the *u* parameter. When the *c/a* ratio decreases, the *u* parameter increases in such a way that those four tetrahedral distances remain nearly constant through a distortion of tetrahedral angles due to long-range polar interactions.

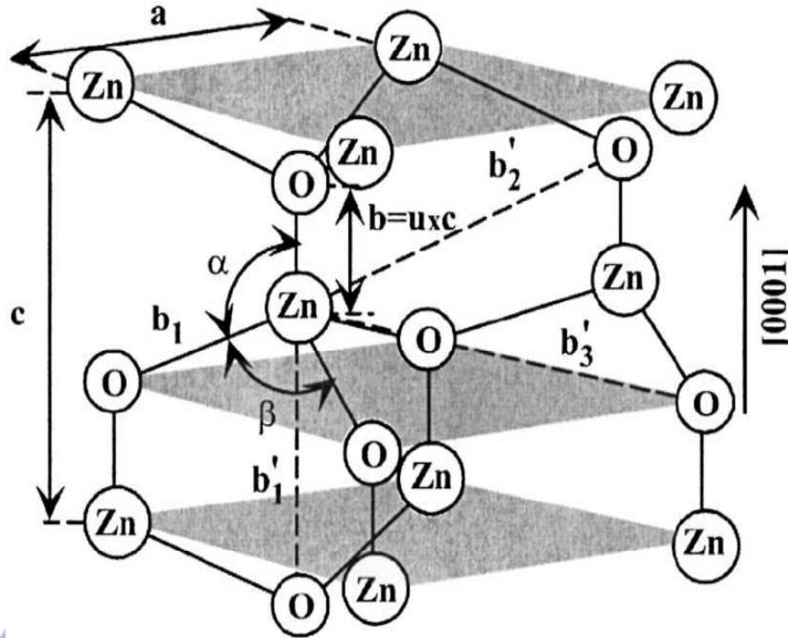

Fig. 2-18 Schematic representation of a wurtzitic ZnO structure having lattice constants *a* and *c*; *u* parameter (0.375 in ideal) is the bond length, and α and β (109.47° in ideal) are the bond angles. [**39**]

The lattice parameters of any crystalline material are commonly and most accurately measured by high-resolution XRD. Several groups reported the measured and calculated lattice parameters, *c*/*a* ratio, and *u* parameter for ZnO crystallized wurtzite structures. The lattice constants for *a* and *c* mostly range from 3.2475-3.2501 Å and 5.2042-5.2075 Å. The *c/a* ratio and *u* parameter vary in a slightly wider range, from 1.593-1.6035 and from 0.383-0.3856, respectively. The deviation from that of the ideal wurtzite crystal is probably due to lattice stability and ionicity. It has been reported that free charge is the dominant factor responsible for expanding the lattice proportional to the deformation potential of the conduction band minimum and inversely proportional to the carrier density and bulk modulus. The point defects such as zinc interstitial, oxygen vacancies, and extended defects, such as threading dislocations, also increase the lattice constant, albeit to a lesser extent in the

heteroepitaxial layers.

2.5.2-2 Selection rules and phonon modes [40, 41]

The different wavelength phonon branches in a given crystal correspond to different symmetries of vibration of the atoms in the unit cell and are characterized by irreducible representations of the space group of the crystal lattice. If the wavelengths of the Raman phonons are assumed to be effectively infinite, then the crystal point group can be used in classifying the phonon symmetries. This infinite wavelength assumption is not valid for Raman-active phonons, which are also infrared active, and this type of vibration will be discussed separately in the following section.

The selection rules for Raman-active phonons can be determined by standard group-theoretical methods described in detail by Heine [42], who based his work on the polarizability derivative theory of Born and Bradburn. The result of this approach is that a phonon can participate in a first-order Raman transition if and only if its irreducible representation is the same as one of the irreducible representations which occur in the reduction of the representation of the polarizability tensor. The irreducible representations, by which the components of the polarizability tensors are conveniently listed by Herzberg *et al*. for the set of molecular point groups, include 32 crystal point groups.

The particular modes of Raman scattering depend on the directions of incidence and observation relative to the principal axes of the crystal. The angular variation of the scattering gives information about the symmetry of the lattice vibration responsible. The anisotropy of the scattering can be predicted for a vibration of any given symmetry by standard group-theoretical methods.

In wurtzite ZnO, the number of atoms per unit cell is four, and there are total 12 phonon modes, one longitudinal acoustic, two transverse acoustic, three longitudinal

optical (LO), and six transverse optical (TO) modes. The hexagonal ZnO structure with C_{6v}^4 symmetry, group theory predicts eight phonon modes at Γ-point of the Brillouin zone, $2A_1$, $2B_1$, $2E_1$ and $2E_2$. One set of A_1 and E_1 modes are acoustic, the other are optical modes. The A_1 and E_1 modes and the two E_2 modes are Raman active while the B_1 modes are silent. The A_1 and E_1 modes are polar, resulting in a splitting of the LO and TO modes. The Raman tensors for the wurtzite structure are as follows:

$$A_1(z) = \begin{pmatrix} a & 0 & 0 \\ 0 & a & 0 \\ 0 & 0 & b \end{pmatrix}$$

$$E_1(x) = \begin{pmatrix} 0 & 0 & c \\ 0 & 0 & 0 \\ c & 0 & 0 \end{pmatrix}, \; E_1(y) = \begin{pmatrix} 0 & 0 & 0 \\ 0 & 0 & c \\ 0 & c & 0 \end{pmatrix} \tag{2-7}$$

$$E_2^{(low)} = \begin{pmatrix} d & 0 & 0 \\ 0 & -d & 0 \\ 0 & 0 & 0 \end{pmatrix}, \; E_2^{(high)} = \begin{pmatrix} 0 & d & 0 \\ d & 0 & 0 \\ 0 & 0 & 0 \end{pmatrix}.$$

Here *x*, *y* or *z* in brackets after an irreducible representation indicates the active direction of vibration and the direction of polarization. Such vibrations occur only in piezo-electric crystals (i.e., crystals with no center of inversion symmetry). In crystals, which do have a center of inversion symmetry, only even-parity vibrations, whose representations have a subscript *g*, can be Raman active and only odd-parity (subscript *u*) vibrations can be IR active. This fact leads to the important complementary nature of IR absorption and Raman effect measurements. Directly above each irreducible representation is a matrix, which gives the non-vanishing components of the Raman tensor, $R^u_{a_1,a_2}$. The different elements of the matrices are the nine components of the tensor obtained by allowing both a_1 and a_2 to take on the

values x, y and z. Here x, y, and z are the crystal principal axes chosen to be identical with the principal axes x_1, x_2 and x_3 defined for all the crystal classes. The component μ of the phonon polarization for the case of IR active vibrations is the quantity given in brackets after the irreducible representation symbol. Table 2-1 summarizes a list of observed zone-center optical-phonon modes for wurtzite ZnO [**43**].

At the Γ point, the vibrational modes in ZnO wurtzite structures can be seen that the existence of the following optic phonon modes: A_1+2 B_1+ E_1+2E_2. A_1 and E_1 modes are both Raman and IR active, while two E_2 modes only Raman active, and $B_1^{(low)}$ and $B_1^{(high)}$ modes are neither Raman or IR active. In addition, the nonpolar E_2 modes are have two frequencies: $E_2^{(high)}$ is related to the vibration of oxygen atoms and $E_2^{(low)}$ is associated with the Zn sublattice. The displacement vectors of the phonon normal modes are illustrated in Fig. 2-19. For the lattice vibrations with A_1 and E_1 symmetry, the atoms move parallel and perpendicular to the *c*-axis, respectively.

Table 2-1 Phonon modes frequencies for wurtzite ZnO [**43**]

ω_0 (cm^{-1}) present work	ω_0 (cm^{-1}) reported	Assignments
96	101^{a,b}	E_{2L}
198	208^{a,b}	$2E_{2L}$
330	332^{a}	$[E_{2L}-E_{2H}]$
364	—	LVM
436	437^{a}	E_{2H}
478	—	LVM
504	509,^{c} 507^{d}	$[E_{1T}+E_{2L}]$
520	516, 513^{c}	$2B_{1L}$
580	577^{a}	A_{1L}
655	645^{a,d}	$[E_{2L}+B_{1H}]$
866	857^{c}	$[E_{1T}+E_{2H}]$
1154	1149,^{b} 1160^{a}	$2A_{1L}$ or $2E_{1L}$

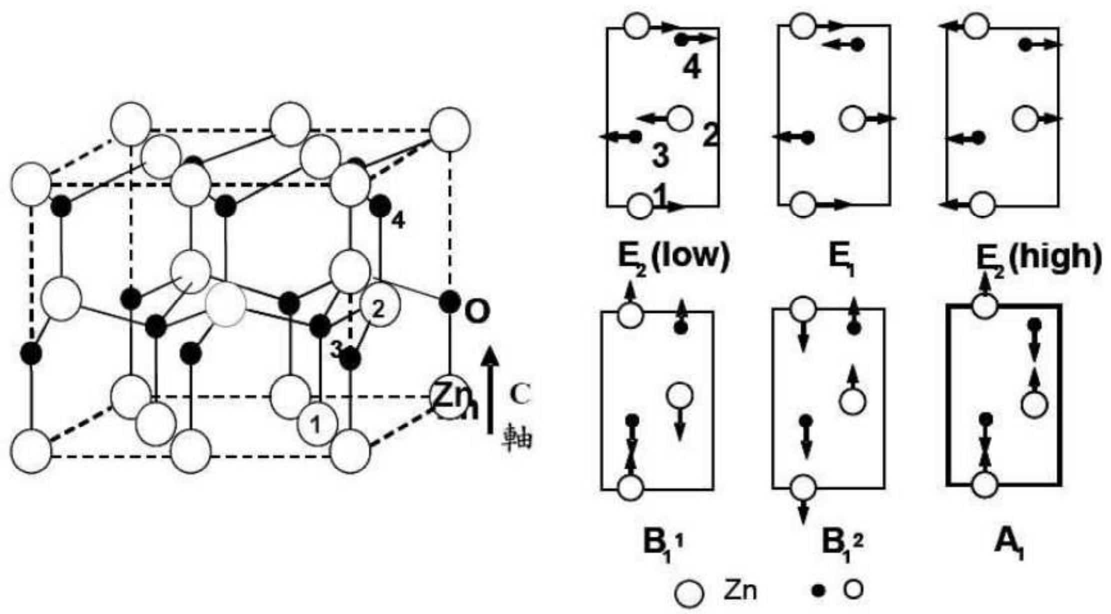

Fig. 2-19 Displacement vectors of the phonon modes in ZnO wurtzite structure. [**44**]

1896

References

1. K. Rajiv, Singh and J. Narayan, Phys. Rev. B, 41, 8843 (1990).

2. K.Y. Cheng, Proc. IEEE, 11 (1997).

3. Chauveau *et al.* J. Appl. Phys. 104, 073535 (2008).

4. J. W. Mathews and A. E. Blakeslee, *J. Cryst. Growth* 27, 188 (1974).

5. J. W. Mathews, "*Epitaxial Growth, Part B, Materials Science Series*" (Academic, New York, 1975).

6. J. Narayan and S. Sharan, *Mater. Sci. Eng.* B 10, 261 (1991).

7. J. Narayan and B. C. Larson, *J. Appl. Phys.* 93, 278 (2003).

8. W.-R. Liu, Y.-H. Li, W. F. Hsieh, C.-H. Hsu, W. C. Lee, Y. J. Lee, M. Hong and J. Kwo, Cryst. Growth Des. 9, 239 (2009).

9. D. B. Wiliams and C. B. Carter, "*Transmission Electron Microsdopy"* (Plenum Press, New York, 1996).

10. C. O. Dunn, and E. F. Koch, *Acta metall.* 5, 548 (1957).

11. Carlo Lamberti , "Characterization of Semiconductor Heterostructures and Nanostructures", Elsevier, 2008.

12. S. Srinivasan, L. Geng, R. Liu, F. A. Ponce, Y. Narukawa, and S. Tanaka, Appl. Phys. Lett. 83, 5187 (2003).

13. J.-M. Chauveau, P. Vennéguès, M. Laügt, C. Deparis, J. Zuniga-Perez, and C. Morhain, J. Appl. Phys. 104, 073535 (2008).

14. S. Perkowitz, *Optical characterization of semiconductors: infrared, Raman, and Photoluminescence spectroscopy* (Sidney Perlpwotz, USA, 1993).

15. C. F. Klingshirn, "*Semiconductor Optics*" (Springer, Berlin, 1997).

16. M. Ueta, H. Kanzaki, K. Kobayashi, Y. Toyozawa, and E. Hanamura, "*Excitonic Processes in Solids*" (Springer-Verlag, Berlin, 1984).

17. A. Mang, K. Reimann, and St. Rübenacke, Solid State Commun. 94, 251 (1995).

18. J. L. Birman, Phys. Rev. Lett. 2, 157 (1959).

19. D. C. Reynolds, D. C. Look, B. Jogai, C. W. Litton, G. Cantwell, and W. C. Harsch,Phys. Rev. B 60, 2340 (1999)

20. W. R. L. Lambrecht, A. V. Rodina, S. Limpijumnong, B. Segall, and B. K. Meyer, Phys. Rev. B 65, 075207 (2002).

21. A. V. Rodina, M. Strassburg, M. Dvorzak, U. Haboeck, A. Hoffman, A. Zeuner, H. R. Alves, D. M. Hofmann, and B. K. Meyer, Phys. Rev. B 69, 125206 (2004).

22. K. Thonke, T. Gruber, N. Teofilov, R. Schönfelder, A. Waag, and R. Sauer, Physica B 308, 945 (2001).

23. C. Boemare, T. Monteiro, M. J. Soares, J. G. Guilherme, and E. Alves, Physica B 308, 985 (2001).

24. D. G. Thomas, J. Phys. Chem. Solids 15, 86 (1960).

25. J. F. Muth, R. M. Kolbas, A. K. Sharma, S. Oktyabrsky, and J. Narayan, J. Appl. Phys. 85, 7884 (1999).

26. A. Teke, Ü. Özgür, S. Do˘gan, X. Gu, H. Morkoç, B. Nemeth, J. Nause, and H. O. Everitt, Phys. Rev. B 70, 195207 (2004).

27. W. Y. Liang and A. D. Yoffe, Phys. Rev. Lett. 20, 59 (1968).

28. S. F. Chichibu, T. Sota, G. Cantwell, D. B. Eason, and C.W. Litton, J. Appl. Phys. 93, 756 (2003).

29. B. K. Meyer, H. Alves, D. M. Hofmann, W. Kriegseis, D. Forster, F. Bertram, J. Christen, A. Hoffmann, M. Strassburg, M. Dworzak, U. Haboeck, and A.V. Rodina, Phys. Stat. Sol. (b) 241, 231 (2004).

30. M. Schilling, R. Helbig, and G. Pensl, J. Lumin. 33, 201 (1985).

31. C. Gonzales, D. Block, R. T. Cox, and A. Hervé, J. Cryst. Growth 59, 357 (1982).

32. H. Alves, D. Pfisterer, A. Zeuner, T. Riemann, J. Christen, D. M. Hofmann, and B.

K. Meyer, Optical Materials 23, 33 (2003).

33. Y. P. Varshni, Physica 34, 149 (1967); L. Wang and N. C. Giles, J. Appl. Phys. 94, 973 (2003).

34. A. Janotti and Chris G. Van de Walle, Phys. Rev. B 76, 165202 (2007).

35. B. Guo, Z. R. Qiu, and K. S.Wong, Appl. Phys. Lett. 82, 2290 (2003).

36. H.-J. Egelhaaf and D. Oelkrug, J. Cryst. Growth 161, 190 (1996).

37. K. Vanheusden, C. H. Seager, W. L. Warren, D. R. Tallant, and J. A. Voigt, Appl. Phys. Lett. 68, 403 (1996).

38. S. A. Studenikin, N. Golego, and M. Cocivera, J. Appl. Phys. 84, 2287 (1998).

39. Ü. Özgür, Ya. I. Alivov, C. Liu, A. Teke, M. A. Reshchikov, S. Doğan, V. Avrutin, S.-J. Cho, and H. Morkoç, J. Appl. Phys. 98, 041301 (2005).

40. R. Loudon, Adv. Phys. 50, 813 (2001).

41. M. A. Stroscio and M. Dutta, "*Phonons in Nanostructures*" (Cambridge university press, United Kingdom 2001).

42. V. Heine, in: Group Theory in Quantum Mechanics (Per-gamon, New York, 1960).

43. J. D. Ye, S. L. Gu, S. M. Zhu, S. M. Liu, Y. D. Zheng, R. Zhang, Y. Shi, Q. Chen, H. Q. Yu, and Y. D. Ye, Appl. Phys. Lett. 88, 101905 (2006).

44. A. P. Jephcoat, R. J. Hemley, H. K. Mao, R. E. Cohen, and M. J. Mehl, Phys. Rev. B 37, 4727 (1988).

Chapter 3 Experimental procedures and characterization technique

3.1 Growth nonpolar ZnO epilayers

A lot of growth methods have been prepared for growth ZnO epitaxial layers, such as RF sputtering, atmospheric pressure halide vapor phase epitaxy (AP-HVPE), metal organic chemical vapor deposition (MOCVD), molecular beam epitaxy (MBE) and pulse laser deposition (PLD). Among growth methods, PLD is an advantage growth ZnO due to ultra-clean, simplicity, and no need for corrosive gas. High-quality epilayers of ZnO can be obtained at lower growth temperature (600 °C) relatively to MBE or MOCVD result from high kinetic energy (10-100 eV) plasma, besides, the atom sources of Zn and O can be obtained from the ZnO target directly without extra oxygen supply.

3.1.1 Cleaning process of substrate and target arrangement

Two different planes of 2" high quality sapphires, *r*-plane and *m*-plane wafers, were used for ZnO growth. Before surface treatment, the substrates were cut into an area of 10x10 mm^2 and then cleaned by using the following steps:

I. Rinsed in D. I. water in 5 min.

II. Rinsed in Acetone solutions by a supersonic oscillator in 5 min.

III. Repeated step I, then rinsed in IPA (Isotropic Alcohol) solutions by a supersonic oscillator in 5 min.

IV. Repeated step I, then dried with the gas of N_2.

V. Immerse in H_2SO_4 : H_2O_2 = 3:1 at 80℃ for 10 min.

VI. Repeated step IV.

After the surface treatment, the substrates were mounted on the substrate holder and

transferred into the deposition chamber.

A commercial hot-pressed stoichiometric ZnO target with purity of 5N (99.999%) is used as the ZnO source and the target size is 1'' × 3 mm. Before deposition, the laser beam was sent onto the ZnO target to remove the contamination on the target surface.

3.1.2 Operation arrangement of laser-MBE deposition

After the surface cleaning, the substrate was mounted on the substrate holder and put into the load-lock chamber with a base pressure below 2×10^{-7} torr. Using transfer arm the substrate holder was then transferred from the load-lock chamber into the deposition chamber, which has base pressure of 1×10^{-8} torr. We used a focusing lens (f = 40 cm) to converge the KrF excimer laser (λ = 248 nm) beam through a laser window onto the target, which makes 45 degree to the normal of the target shown in Fig. 3-1. The repetition rate and pulse duration of excimer laser are at 6-10 Hz and 25 ns, was focused to produce an energy density ~ 6 $J\cdot cm^{-2}$ on ZnO (5N) target which located in front of the substrate holder at a distance of 4.5 cm. In order to grow uniform layer, the laser beam was scanned over the target surface by a moving reflection mirror, which is carried by a step motor. At the same time, both the target holder and the sample holder rolled during deposition to growth uniform film. The substrate is heated with a halogen light bulb through a programmable temperature controller, the controller region of the substrate temperature were varied from room temperature (RT) to 700 °C. The nonpolar ZnO films were deposited without flowing oxygen, under which a background chamber pressure of 3×10^{-8} torr was maintained. Table 3-1 lists the growth conditions for ZnO epilayers on different substrates.

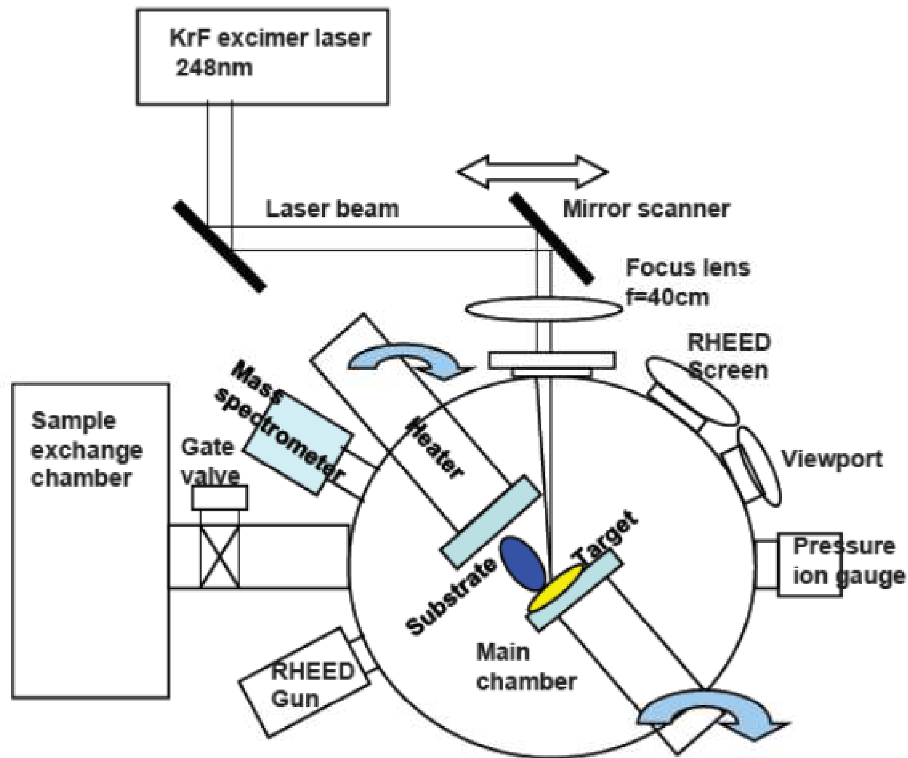

Fig. 3-1 Layout of the PLD growth system

Table 3-1 List the parameters of growth for ZnO epilayers

Substrates	Growth Temperature	Growth Rate	Typical thickness
r-plane Al_2O_3	*300-500 ℃*	*0.47 Å /s*	*~ 500 nm*
m-plane Al_2O_3	**400-600℃**	**0.57 Å /s**	**~ 500 nm**
m-plane Al_2O_3	**LT: ~200℃** **HT: 600℃**	**0.53 Å /s** **0.56 Å /s**	**~ 400 nm**

3.2 Structural and lattice dynamics characterization of the ZnO films

3.2.1 X-ray diffraction (XRD)

The crystal structure of the nonpolar ZnO films was measured by XRD, which were performed with a four-circle diffractometer as illustrated in the schematic (Fig. 3-2) at the beamlines BL17B, BL07A and BL13A of National Synchrotron Radiation Research Center, (NSRRC) Taiwan, with the incident wavelength 1.1272, 1.0335 and 1.027 Å, respectively. A NaI scintillation detector is mounted on the 2θ circle away from the sample. Two pairs of slits located between the sample and a detector yielding a typical resolution of 4 x10^{-3} $Å^{-1}$. The other three degrees of freedom, ϕ, χ, and θ circles control the sample orientation of a four-circle diffractometer. The combination of χ and θ which are mutual perpendicular determines the tilting angle between the surface normal and incident x-ray.

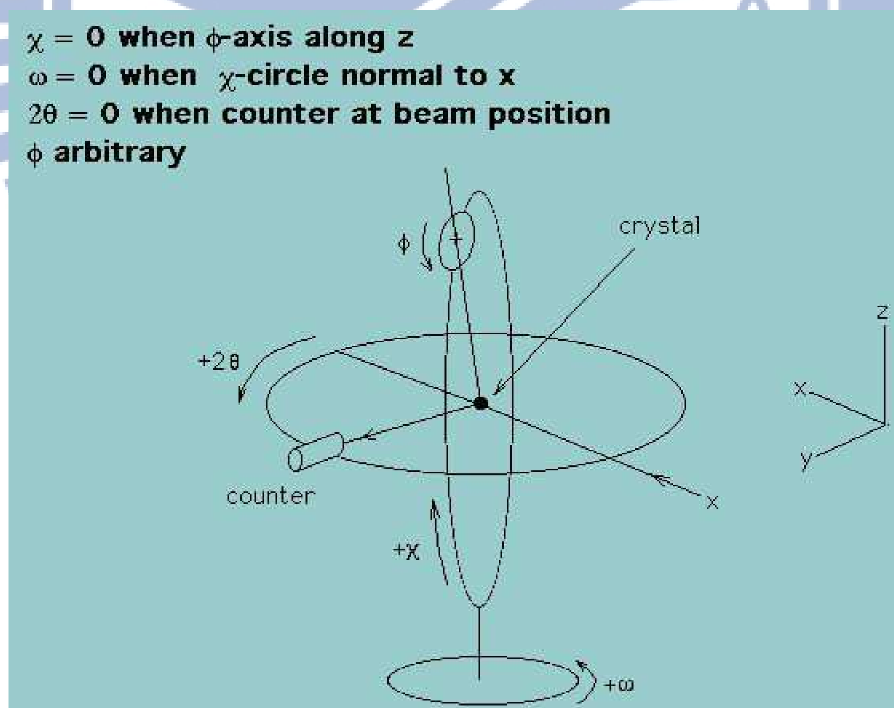

Fig. 3-2 Schematic of a four-circle diffractomter

3.2.2 Transmission electron microscopy (TEM)

Complementary to XRD measurements, transmission electron microscopy (TEM) micrographs were also taken for structural defect analysis. The TEM samples with the thickness of about 80±10 nm were prepared by dual-beam focused ion beam (DB-FIB) with gallium ion source. Cross sectional TEM images and SAED patterns were taken using a JEM-2100F/JEOL TEM at 200 keV shown in Fig. 3-3. The resolution of point and line are below 1.9 and 1 Å, respectively.

Fig. 3-3 Appearance of JEM-2100F TEM system

3.2.3 Raman spectroscopy

The Raman spectrometer consists mainly of three components: a laser system serves as a powerful excitation source, a computer controlled spectrometer for wavelength analysis of the inelastically scattered light. The micro-Raman system was performed in the backscattering geometry with a confocal Olympus (BX-40) optical microscope. The scattered light was dispersed by the HORIBA iHR-550 (Jobin–Yvon, France) monochromator system and detected a liquid nitrogen cooled charge coupled device (CCD) at 140 K. Raman spectroscopy was carried out using Ar+ laser (Coherent INNOVA 90) as the excitation light source at a wavelength of

488 nm with power of 40 mW. The best spectral resolution of Raman measurements is 0.4 cm^{-1}.

The polarized mirco-Raman spectra with excitation wavelength of He–Ne laser (632.8nm) were recorded by a LabRam HR800 (Jobin–Yvon, France) spectrometer with an automatized *XZ* table of acquisition.

3.3 Surface morphology measurement-- Atomic force microscopy

The surface morphology and the roughness of nonpolar ZnO films were measured by an atomic force microscope (AFM). The atomic force microscope is one of two-dozen types of scanning probe microscope (SPM), which measures a local property, such as morphology, electrification, magnetism and optical emission, by probe or "tip" very close to the sample. The small distance of the probe and sample makes possibility to measure the local signal. To acquire an image, the probe scans over the sample while measuring the small signal locally. The resulting resembles an image on a television screen in that both consist of many rows or lines of information placed one above the other. It is unlike the traditional microscopes that the scanned-probe systems do not use the lenses, so the size of the probe rather than diffraction effects generally limits their resolution. AFM can measure the sample morphology by recording cantilever deflection error or the feedback output height. To calculate by software, two signals often produce the actual topography, but it gives a well-adjusted feedback loop and the error signal may be too small to consider.

3.4 Measurements of optical properties

3.4.1 Photoluminescence system (PL)

For photoluminescence (PL) measurement, we used a He-Cd laser (Kimmon

IK5552R-F) with wavelength of 325 nm as the pumping source. The schematic of the PL system is shown in Fig 3-4. The excitation laser beam was directed normally and focused onto the sample surface with power being varied with an optical attenuator. The spot size on the sample is about 200 μm. Optical emissions were collected and coupled into a 0.32 m focal-length monochromator (TRIAX 320) with a 1200 lines/mm grating, the spectrometer is equipped with a CCD (CCD-3000) and photomultiplier tube (PMT-HVPS) operating voltage of 950 V. Before measuring the PL spectra, we calibrate the monochromator by the standard fluorescent lamps. The PL measurement is recorded at the resolution of 0.1 nm with 0.1 sec of integration time. According to the measurement condition, the laser filter marked red region in Fig. 3-4 would be changed to bandpass filter (335-425 nm) or added polarizer with pass band ranging from 300-400 nm. The temperature-dependent PL measurements were carried out using a closed cycle cryogenic system. A closed cycle refrigerator was used to set the temperature anywhere between 13 K and 300 K.

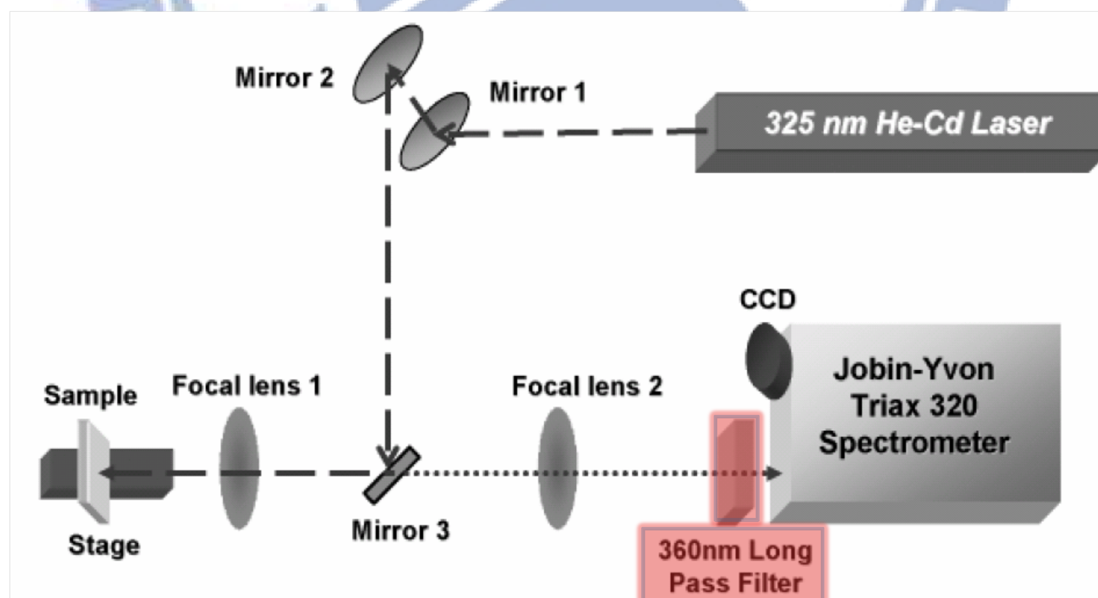

Fig. 3-4 Layout of PL system

3.4.2 Optical reflection (OR) system

Optical reflection (OR) measurements are routinely used to determine the optical transition bands. OR spectra were made using a broad-band light (Xenon lamp) and the reflection light was collected by a fiber bundle and coupled into monochromator (TRIAX 320) with a 1200 lines/mm grating and detected by a UV-sensitive PMT. When the polarized OR measurement, the UV polarizer put in front of the aperture to vary different polarizations of incident light source. Figure 3-5 is a schematic diagram showing the absorption system.

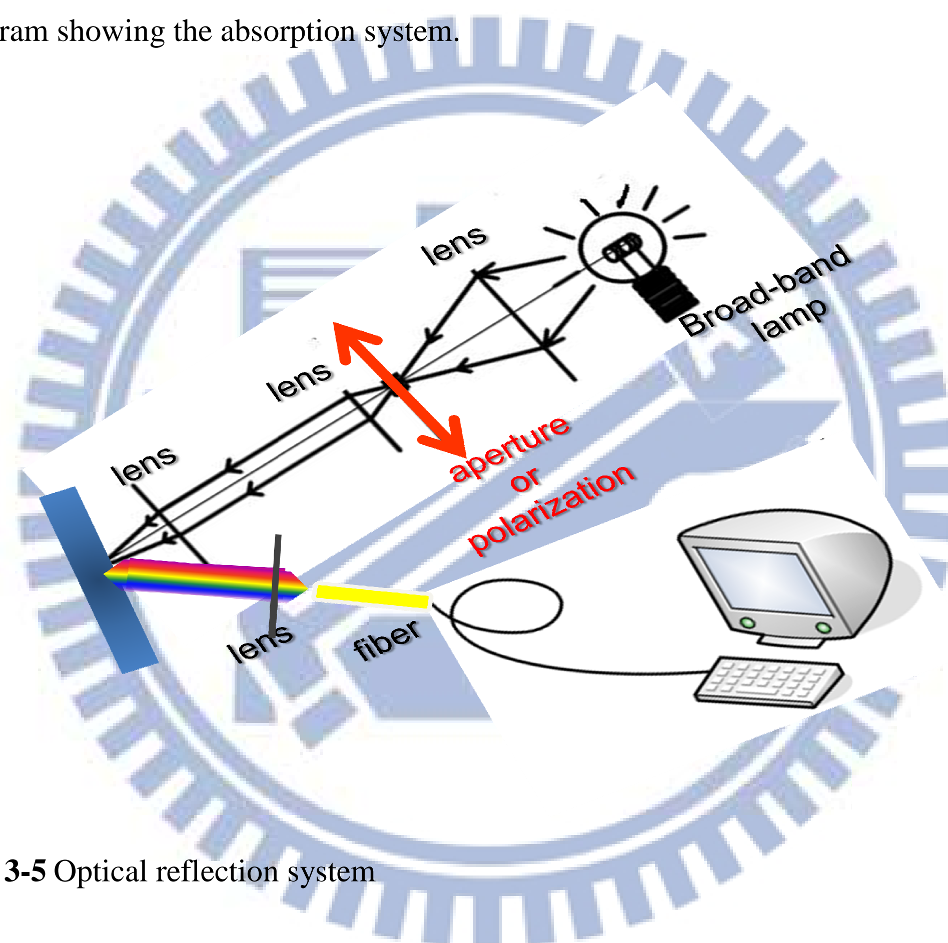

Fig. 3-5 Optical reflection system

Chapter 4 Anisotropic biaxial strains induced crystal symmetry breaking in nonpolar *a*-ZnO on *r*-sapphire

4.1 Introduction

From the *r*-sapphire substrate and the *a*-plane ZnO surfaces, in-plane lattice constants of *a*-ZnO and *r*-sapphire are 5.629 Å along $ZnO[1\bar{1}00]$, 5.2069 Å along $ZnO[0001]$, 4.756 Å along $Al_2O_3[11\bar{2}0]$ and 5.1272 Å along $Al_2O_3[\bar{1}101]$, respectively. The *a*-ZnO in-plane parameters are larger than those of *r*-sapphire, inducing an initial compressive strain of ZnO in both directions. A strong anisotropy is observed in *a*-ZnO grown on *r*-sapphire that resulting from lattice mismatch is of 1.55% along the ZnO *c*-axis and the other is large as 18.3% along the perpendicular direction $ZnO[1\bar{1}00]$ [**1**]. However, considering the domain matching model (DMM) between *m* planes of ZnO and *m*+1 planes in sapphire, $(m+1)d_{Al_2O_3} = md_{ZnO}$, is relaxed the initial strain. The domain matching with five $ZnO(1\bar{1}00)$ planes onto six $Al_2O_3(11\bar{2}0)$ planes achieve strain-relaxation along $ZnO[1\bar{1}00]$ to reduce initials strain to -1.37%. Using lattice matching (LM) and domain match (DM) modes, there still are anisotropic strains, which are 1.55% and -1.37% along $ZnO[0001]$ and $ZnO[1\bar{1}00]$, respectively. Moreover, the biaxial anisotropic strain on nonpolar *a*-ZnO should be influenced on optical properties.

In previous investigations, the polarization dependence of the near-band-edge optical reflection (OR), photoluminescence (PL), and photoreflectance (PR) spectra in nonpolar ZnO show that the orientation and the anisotropic strain of ZnO play special roles in determining the polarization selectivity and properties of excitonic transitions.

[**2,3**] The transitions of free excitons A and B are allowed for light polarization *E* perpendicular to the *c* axis and the free-exciton C band is allowed for *E* parallel to the *c* axis for C_{6V} wurtzite ZnO. Koida *et al.* [**3**] reported that the anisotropic strains change the crystal symmetry and the A, B, and C exciton transitions can no longer be used. Therefore, nomenclature E_1, E_2, and E_3 for the ground states of the three excitons have been used by Ghosh *et al.* [**4**] to describe the exciton transitions in the nonpolar GaN. The theoretical calculation reveals the biaxial strain on nonpolar-oriented plane in GaN systems breaks the crystal symmetry to change the optical transitions [**4, 5**]. In this chapter, we grew ZnO films on *r*-plane sapphires using laser-MBE. XRD was used to determine the change of crystal structure. And polarized micro-Raman, optical reflectance (OR) and photoluminescence (PL) spectra were measured to observe the frequency shifts of vibration modes and the optical properties to further confirm the structure of the nonpolar ZnO film. We expect finding the relationship of the crystal structure change with the optical properties of the nonpolar ZnO epifilms.

4.2 Crystallographic orientation of *a*-ZnO on *r*-sapphire

Figure 4-1 illustrates a X-ray diffraction (XRD) radial scan along the surface normal using four-circle diffractometer at the beamline BL13A of NSRRC having incident wavelength of 1.0305 Å. In addition to the $\left(02\bar{2}4\right)$ reflection from the *R*-sapphire substrate, there is only a single ZnO $\left(11\bar{2}0\right)$ reflection and its harmonic observed that confirms *a*-plane orientation of the ZnO layer. We also performed azimuthal-scans across the ZnO $\{10\bar{1}0\}$ and sapphire $\{20\bar{2}2\}$ off-normal reflections, as shown in Fig. 1(b), to examine the in-plane orientation relation. The

two peaks with 180° apart are the $(10\bar{1}0)$ and $(01\bar{1}0)$ reflections of ZnO and two peaks of sapphire $(20\bar{2}2)$ and $(\bar{2}202)$, respectively. The coincidence of the angular positions of ZnO $(10\bar{1}0)$ and sapphire $(20\bar{2}2)$ yields the in-plane epitaxial relationship of $ZnO[0001] \| Al_2O_3[0\bar{1}11]$. The small values of full width at half maximum (FWHM) of θ-rocking scans at the ZnO $(11\bar{2}0)$ normal reflection, 0.20°-0.27° depending on azimuth, and of Φ-scan across ZnO $\{10\bar{1}0\}$ non-specular reflections of 0.5° manifest high structural perfection of the as-grown film. However, Zhang *et al*. [**6**] has reported that there is a tilted 0.3° between $ZnO\left(11\bar{2}0\right)$ and $Al_2O_3\left(02\bar{2}4\right)$ substrate and rotated about 7° around the normal of the sample surface. The large misalignment should interfere the optical measurements because the *a*-ZnO epilayer is sensitive to the excitation polarization with respect to the in-plane crystalline direction. We also check the titling angle between *a*-plane ZnO and *r*-Al_2O_3. Figure 4-2 shows the misalignment of *a*-ZnO on *r*-Al_2O_3 when the radical scans of surface normal along $ZnO[11\bar{2}0]$ and $Al_2O_3[01\bar{1}2]$, respectively. The huge difference of intensity indicates the misalignment of surface normal between Al_2O_3 and ZnO. From the data of XRD radical scans and azimuthal-scans, we can illustrate the complete reciprocal space of *a*-ZnO on *r*-Al_2O_3 in Fig. 4-3. The red and purple circles represent the reciprocal lattice points of *r*-Al_2O_3 and *a*-ZnO, respectively. The $ZnO(\bar{1}100)$ plane aligns with the $Al_2O_3(2\bar{1}\bar{1}0)$ plane perfectly. However, there is misalignment of the $ZnO\left(11\bar{2}0\right)$ (surface normal) with the $ZnO\left(0002\right)$ (in-plane). The reason of the titling angle is further discussion in the following section.

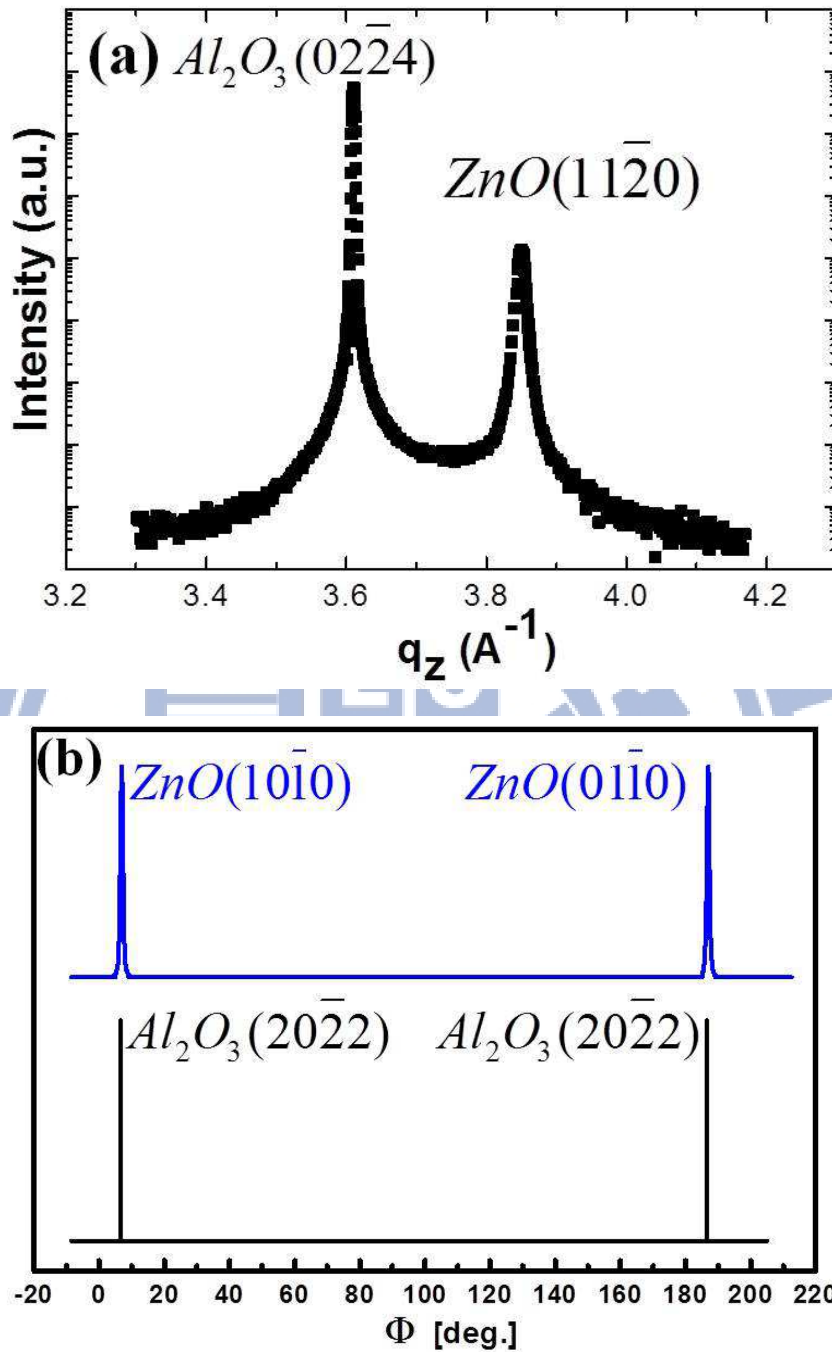

Fig. 4-1 (a) XRD radial scan along surface normal, in which only the ZnO $(11\bar{2}0)$ and sapphire $(02\bar{2}4)$ reflections were observed and (b) shows azimuthally *Φ*-scans across the ZnO $\{10\bar{1}0\}$ and sapphire $\{20\bar{2}2\}$ off-normal reflections.

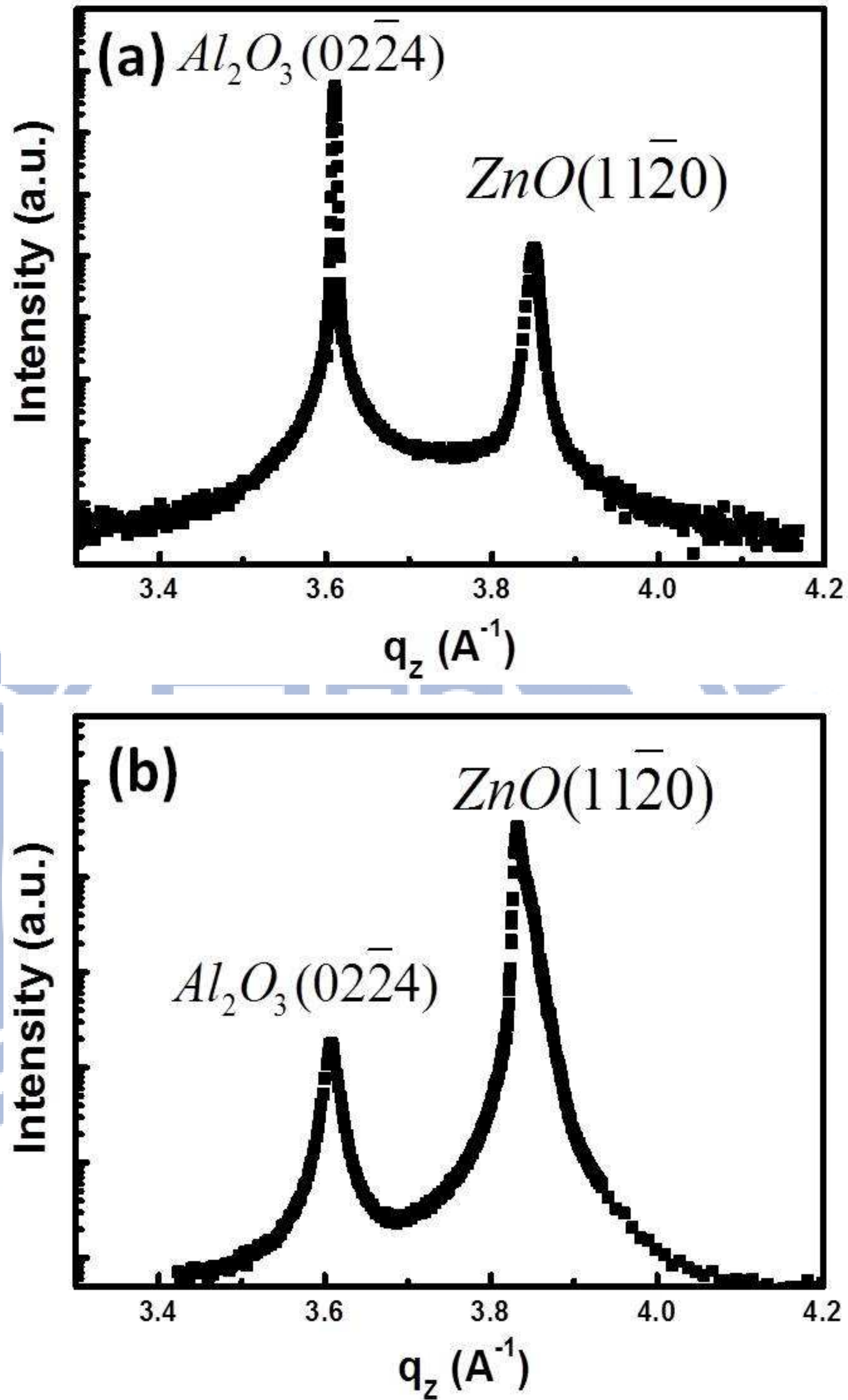

Fig. 4-2 The radical scans of surface normal along (a) $Al_2O_3[01\bar{1}2]$ and (b) $ZnO[11\bar{2}0]$, respectively.

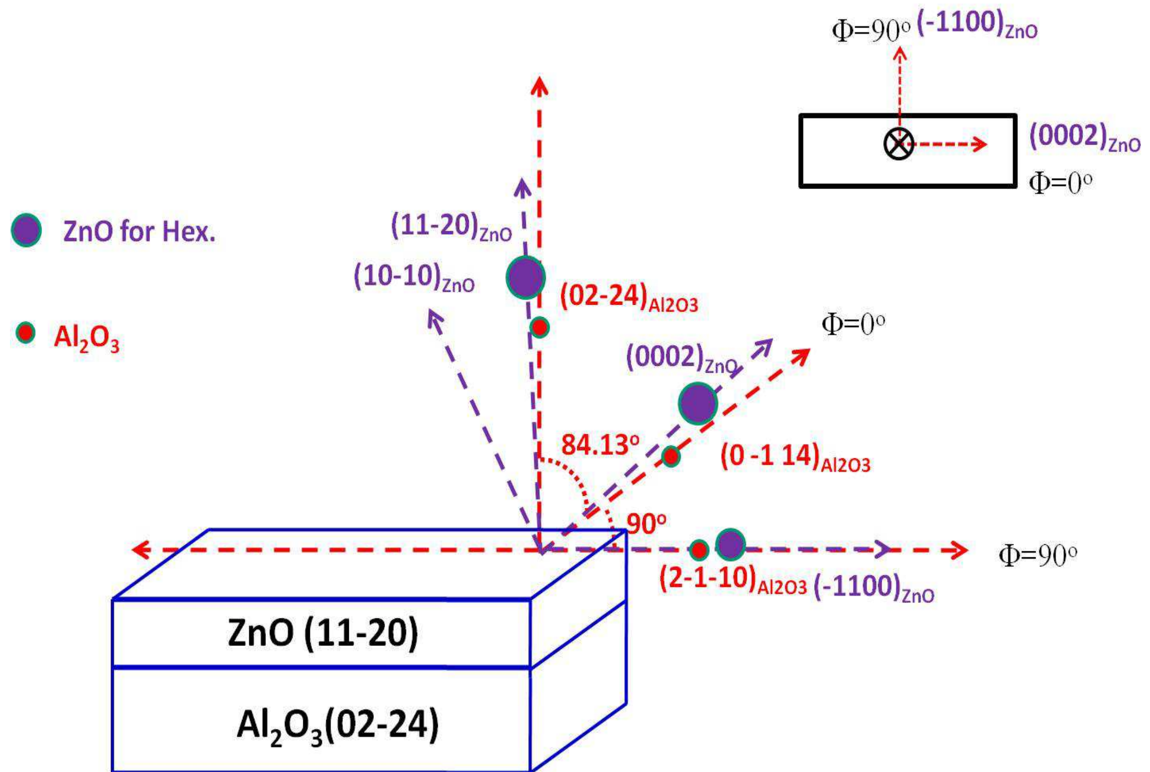

Fig. 4-3 Schematic illustrates the reciprocal spaces of *a*-ZnO/ *r*-Al_2O_3, the red and purple circles represent the reciprocal lattice point of *r*-sapphire and *a*-ZnO, respectively.

The XRD surface-normal scans show the misalignment between *r*-Al_2O_3 and *a*-ZnO. In addition to the titling angle we want to know the titling with respect to the substrate. Shown in Fig. 4-4(a) with color symbols are the Φ dependence of the mis-orientated tilting angles of the sapphire optical plane (black) and the surface normal of ZnO film (red) as well as the FWHM of the rocking curve (blue) of the ZnO $(11\bar{2}0)$ plane growth at 400℃. The sapphire optical plane is not completely centered but with an offset of 0.95° that is attributed to the substrate miscut and the ZnO normal surface had a slight tilting angle of 1.25° to the same Φ angle as in Ref. **6**. The small misalignment of the ZnO film was further confirmed by the polarized optical measurements that will be discussed later on. We observed the maximal

miscut of r-Al_2O_3 and the misalignment of $ZnO(11\bar{2}0)$ is about 0.0303° and is 0.3135° at Φ=45°. The upshot towards Φ=45° implies the misalignment of ZnO is attributed to the miscut of r-Al_2O_3. Furthermore, FWHM of $(11\bar{2}0)$ ZnO unequally distributed over the Φ angle shows anisotropic feature in crystal structure. The ω-rocking curve of $ZnO(11\bar{2}0)$ shown in Fig. 4-4(b) has the FWHM of 0.2029° and 0.2673 at Φ=0° and 90°. The small values of ω-rocking FWHMs indicate the high quality of a-ZnO on r-Al_2O_3. The rocking curve of $ZnO(11\bar{2}0)$ shows asymmetric distribution with different Φ angle implies the strain is anisotropy.

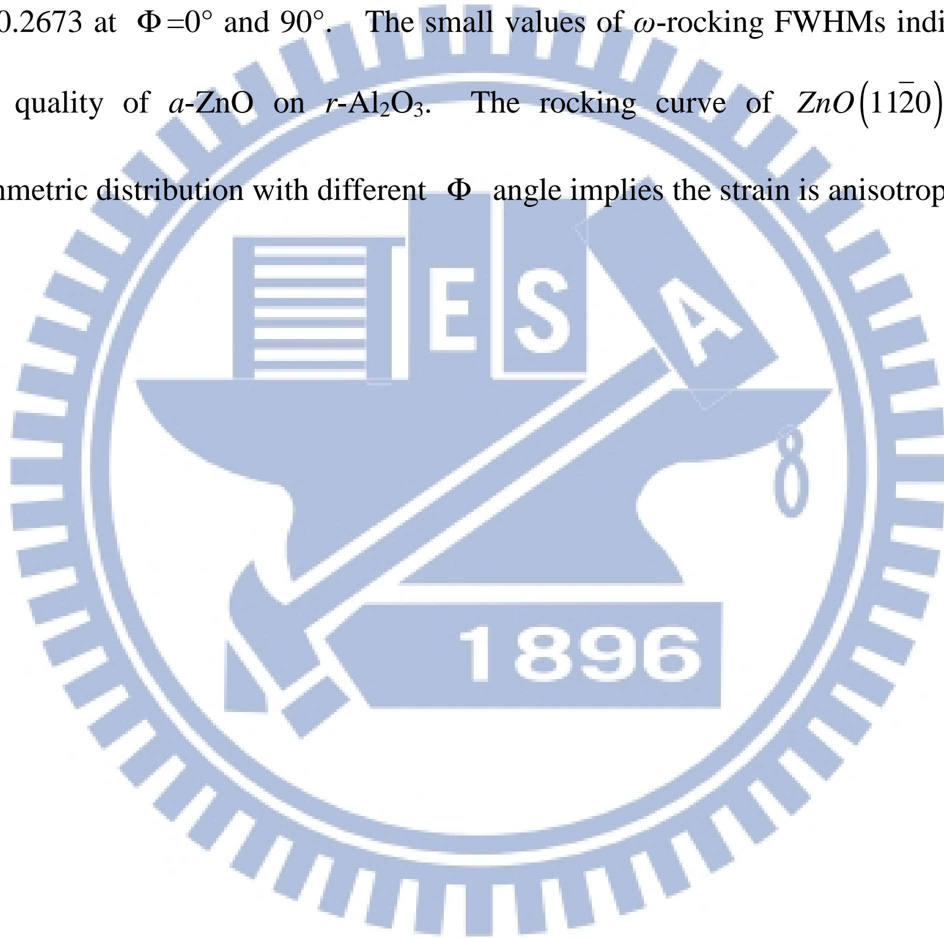

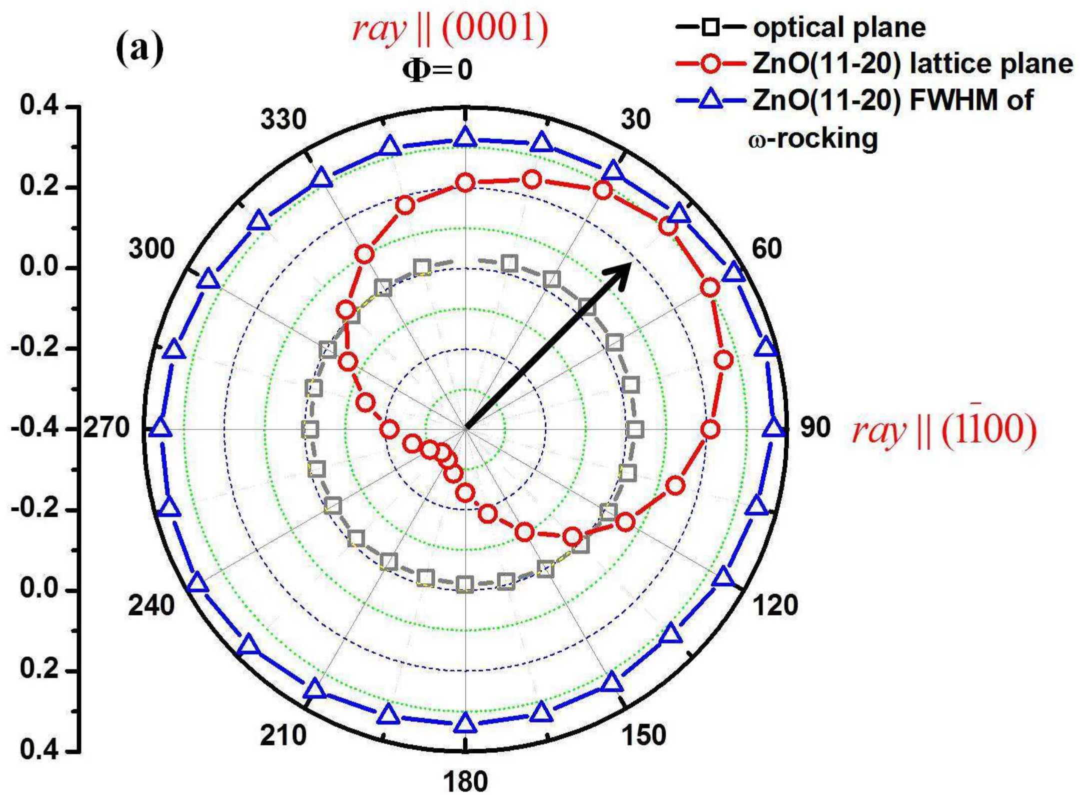

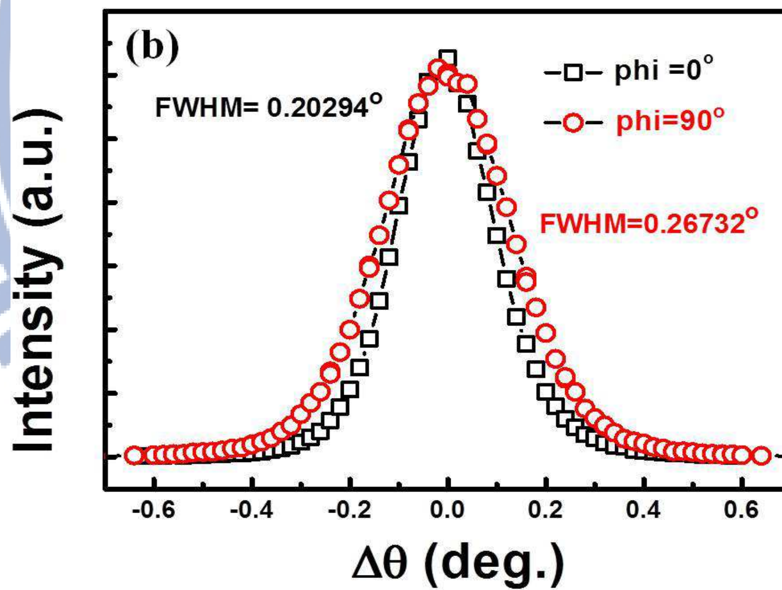

Fig. 4-4 (a) With different Φ, the miscut of *r*-Al2O3 optical plane (black) and misalignment of $ZnO(11\bar{2}0)$ (red) as well as the FWHM of the rocking curve (blue) of the $ZnO(11\bar{2}0)$ plane growth at 400℃, respectively. The black arrow directs the maximum miscut and misalignment at Φ =45°. (b) The rocking curves of

$ZnO\left(11\bar{2}0\right)$ shows the anisotropic distribution.

4.3 Anisotropic strain versus the growth temperature

In order to observe the change of structural properties with the growth temperature, we calculate the lattice constants of *a*-ZnO thin films grown at different temperatures from the XRD measurements in Fig. 4-5(a). The dash blue and red lines are lattice constants *a* and *c* for the ZnO wafer, which are 3.2438 Å and 5.20364 Å determined from XRD measurement. The corresponding strains of *a*-ZnO films calculated from the lattice constants of the film a_i^f and that of the undeformed bulk ZnO a_i^o can be determined by $\varepsilon_{ii} = (a_i^f - a_i^0)/a_i^0$. It is tensile strained along the *a*-axis or along $ZnO[1\bar{1}00]$ ($\varepsilon_{aa} \approx 0.34\% > 0$) and is compressive along the c-axis ($\varepsilon_{cc} \approx -0.374\% < 0$). Furthermore, the dependence of in-plane strain of *a*-ZnO on the growth temperature is shown in Fig. 4-5(b). The inhomogeneous strains by Williamson-Hall plot are $\varepsilon_{\perp c} > 0.194\%$ and $\varepsilon_{\parallel c} > 0.163\%$, the values of in-plane strains along *c*-axis and vertical to *c*-axis are different. The homogeneous and inhomogeneous strains are relaxed toward bulk values with increasing the growth temperature. In addition, we also observe the rocking curve become more asymmetric with increasing growth temperature. The decreasing strain and increasing rocking curve anisotropic with enhanced growth temperature should result from the strain relaxation. The strong anisotropic biaxial strain leads to the lattice deformation from hexagonal to rectangular one and the crystal structure changes from hexagonal to orthorhombic that causes change of transition bands [**4, 7**]. Therefore, the nonpolar *a*-ZnO film has anisotropic strain that could change the structure from hexagonal toward orthorhombic.

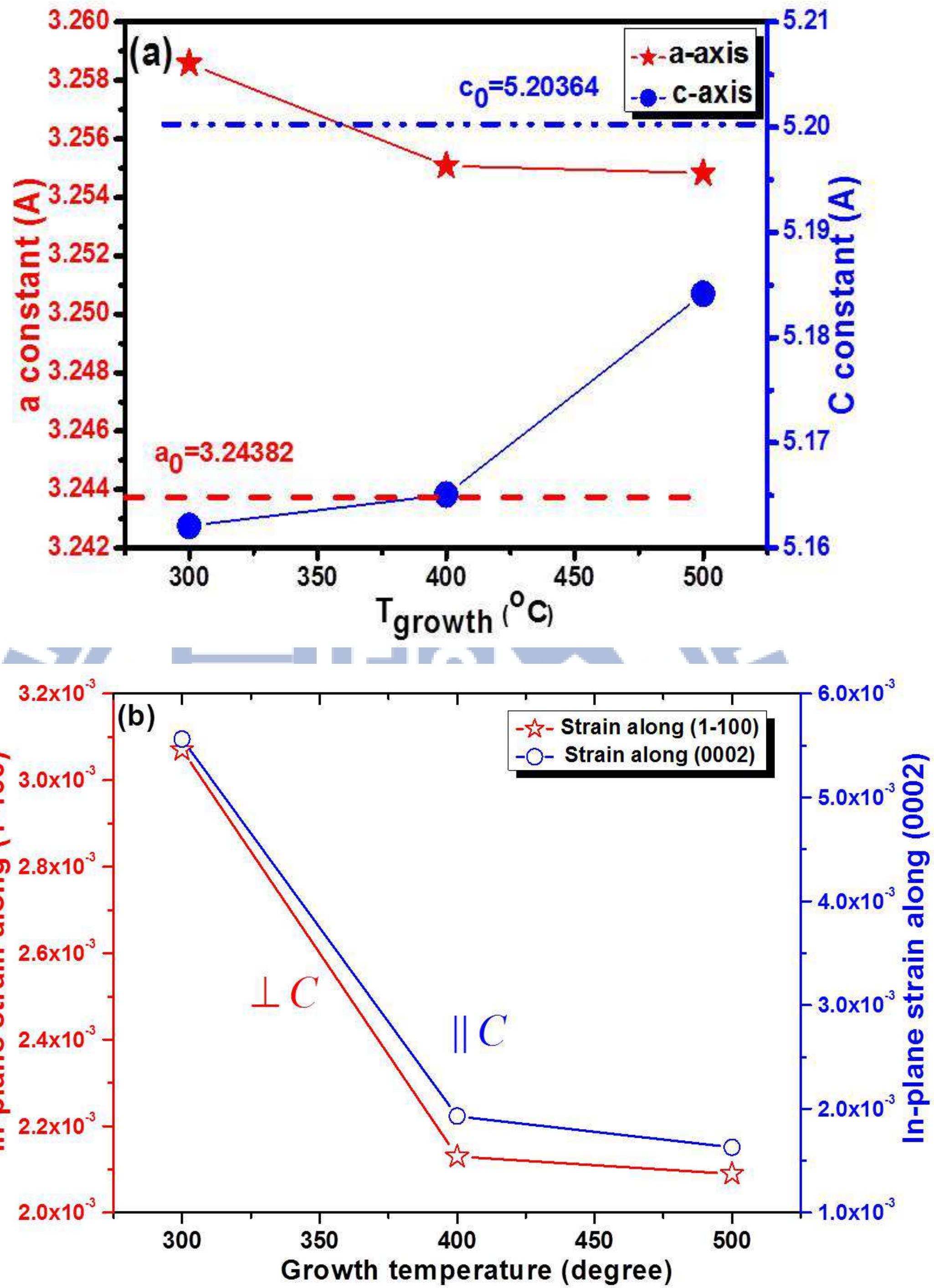

Fig. 4-5 (a) The lattice constant of *a*-ZnO and (b) in-plane strains along *c*-axis and normal *c*-axis with different growth temperature. The dash line of red and blue are the lattice constant for ZnO wafer. (a) and (b) also show anisotropic strains and strain relaxed with high temperature grown.

4.4 The influence of anisotropic strains on optical properties in *a*-ZnO

4.4.1 Polarized Raman measurement

Deriving from peak positions, we determined the inter-planar spacing *d* associated with three mutually orthogonal planes, $(11\bar{2}0)$, $(1\bar{1}00)$, and (0002), of the ZnO epi-layer grown at 400℃ are 1.6374, 2.8185, and 2.582 Å, respectively. The deviation of the ratio $d_{(1\bar{1}00)}/d_{(11\bar{2}0)}$ = 1.721 from the expected value for a hexagonal lattice, $\sqrt{3}$, signifies the breaking of hexagonal symmetry and the transformation of the lattice into an orthorhombic one by the matrix, [7]

$$\begin{pmatrix} h \\ k \\ l \end{pmatrix}_{orth.} = \begin{pmatrix} h \\ k \\ l \end{pmatrix}_{hex.} \begin{pmatrix} 1/2 & -1/2 & 0 \\ 1/2 & 1/2 & 0 \\ 0 & 0 & 1 \end{pmatrix}. \quad (4\text{-}1)$$

Defining the p-$[1\bar{1}00]$, a-$[11\bar{2}0]$, and c-[0001] axes of the wurtzite ZnO lattice as the three orthogonal axes *x, y* and *z* of the orthorhombic lattice. The strains along the three orthorhombic axes are 0.33%, 0.96%, and -0.76%, respectively. It manifests the ZnO layer is under a tensile strain along the growth direction, i.e., *y*-axis; laterally the lattice is tensile-strained along the nonpolar *x*-axis and compressively stressed along the polar *z*-axis, which are in agreement with the results reported by Saraf *et al.* [7]. The anisotropic strains make the crystalline structure distorted from hexagonal symmetry transform to orthorhombic; the schematic diagram of the distorted ZnO unit cell in *x*-*y* plane show in Fig. 4-6, where the dashed and solid lines are labeled as wurtzite ZnO and distorted ZnO with the same volume, respectively. The angles between *y*-axis and the other axis are 30.63° and 32.41° in *x*-*y* and *y*-*z* planes,

respectively, which should be 30° and 31.969° for hexagonal structure. The anisotropic strains distorted the wurtzite ZnO unit cell cause the distorted unit cell of ZnO, showing the two-fold symmetry. The distorted unit cell satisfies the point group C_{2V} symmetry and conflicts with the C_{6V} symmetry, so the crystal symmetry of nonpolar *a*-ZnO with anisotropic strains should change from the C_{6V} to C_{2V}.

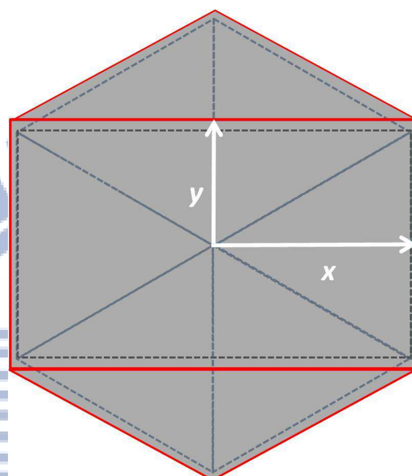

Fig. 4-6 The unit cells of wurtzite ZnO and distorted ZnO are labeled as dash and solid lines, where y- and x-axes are the orthorhombic axes.

Raman scattering is governed by the polarization dependent selection rules imposed by the crystal symmetry and is sensitive to strain state. Using the polarized Raman spectroscopy, we examine the effect of biaxial in-plane strain in nonpolar *a*-ZnO epi-layer to its excitonic transitions. The polarized Raman spectra taken under the four distinct backscattering geometries, Ⅰ, Ⅱ, Ⅲ, and Ⅳ, are shown in Fig. 4-7. The micro-Raman peaks at 378.3, 417.0, 429.4, 576.1, and 644.1 cm^{-1} originate from the sapphire substrate. The optical phonon modes with C_{6V}^{4} point symmetry include $A_1 + 2B_1 + E_1 + 2E_2$, in which B_1 modes are silent and the others are Raman active. Examining the two Raman peaks at ~100.6 and ~443.0 cm^{-1}, which correspond to E_2 modes of wurtzite ZnO [**8**], we observed red shift for $E_2^{(low)}$ mode

but blue shift for $E_2^{(high)}$ mode with respect to the bulk values (101 and 437 cm^{-1}). In addition, we observed various strain states of the samples with different growth temperatures that the position of $E_2^{(high)}$ mode is close to the bulk value when it is grown at high temperature. The reason is that the more strain is relaxed at high growth temperature that is consistent with the XRD measurement.

Since the $E_2^{(low)}$ mode has a very small pressure coefficient and is not conspicuously affected by the strain, the $E_2^{(high)}$ mode is adapted for accurate strain determination [**9**]. The $E_2^{(high)}$ mode is sensitive to the strain within the wurtzite basal plane, in which a compressive stress leads to an increase of $E_2^{(high)}$ vibration frequency [**10, 11**]. Therefore, our Raman results imply a compressive strain within the basal plane and a tensile strain along the *c*-axis, provided that the wurtzite crystal structure is assumed. However, this is inconsistent with our XRD observations, i.e., biaxial tensile strain within the *x-y* plane and compressive strain along the *c*-axis. This contradiction can be resolved by changing the crystal structure from hexagonal to orthorhombic symmetry because anisotropic biaxial strains within the basal plane can further lift the symmetry in this nonpolar plane of the wurtzite structure [**4, 5**].

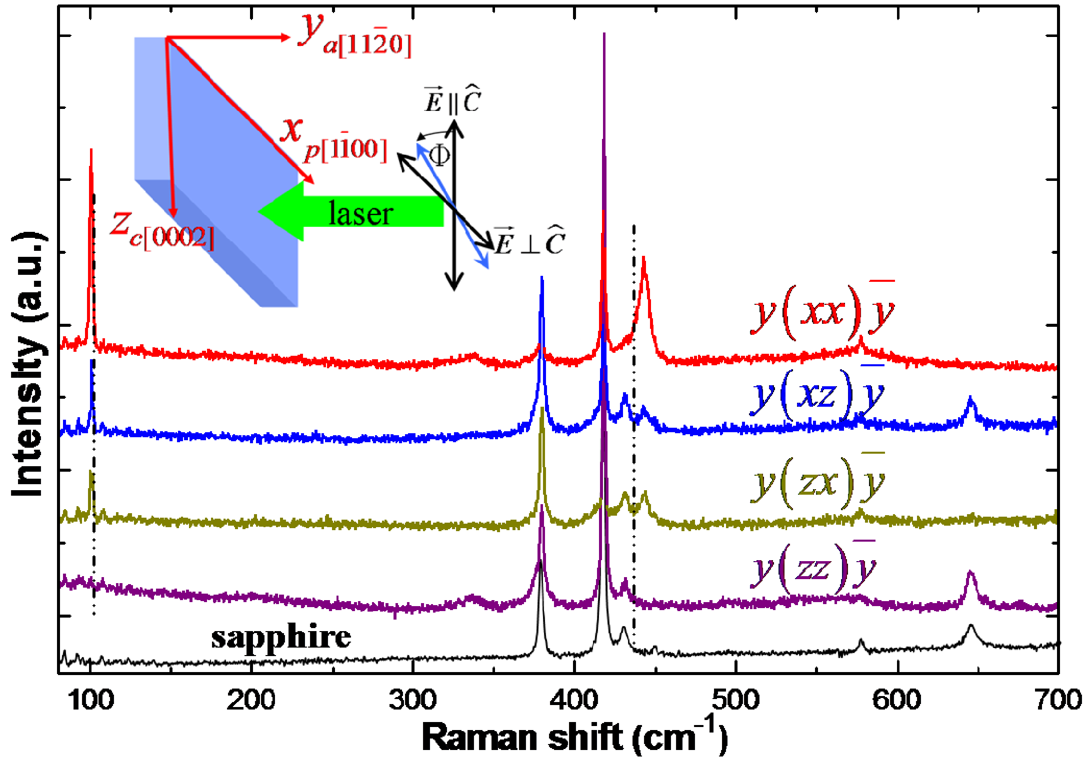

Fig. 4-7 Polarized Raman spectra taken in 4 distinct backscattering configurations. A spectrum of bare sapphire substrate is also plotted for comparison. The dashed lines at 101 and 436 cm^{-1} mark respectively the positions of $E_2^{(low)}$ and $E_2^{(high)}$ modes of bulk ZnO. A schematic of the scattering geometry is also shown in the inset.

The E_2 modes of a crystal with wurtzite structure have non-vanishing Raman scattering matrix elements of $E_2^{(low)}=(\alpha_{xx}, -\alpha_{yy})$ and $E_2^{(high)}=(\alpha_{xy}, \alpha_{yx})$, where x and y are polarization directions along the hexagonal crystallographic p-$[1\bar{1}00]$ and a-$[11\bar{2}0]$ directions [**12-14**]. If the a-plane ZnO epi-layer still maintained the C_{6V}^4 symmetry, we would expect observing the $E_2^{(low)}$ mode only in (xx) and (yy) polarization configurations and the $E_2^{(high)}$ mode only in (xy) and (yx) polarization configurations. Contrarily, for a crystal with the C_{2V} symmetry, there

are 24 $(7A_{1g}+5B_{1g}+7B_{2g}+5B_{3g})$ Raman active modes with the corresponding Raman matrix elements $A_{1g}=(\alpha_{xx},\alpha_{yy},\alpha_{zz})$, $B_{1g}=(\alpha_{xy},\alpha_{yx})$, $B_{2g}=(\alpha_{xz},\alpha_{zx})$, and $B_{3g}=(\alpha_{yz},\alpha_{zy})$ [**12, 15**]. Under the current experimental geometry with laser traveling along the *y*-axis, the B_{1g} and B_{3g} modes were not accessible. The peaks at 100.7 and 443.6 cm^{-1} appear in both Ⅱ and Ⅲ configurations are of B_{2g} symmetry. Two nearby peaks at 100.5 and 442.7 cm^{-1} were observed in the Ⅰ configuration suggesting they are the A_{1g} modes. Although the peak positions of the A_{1g} and B_{2g} modes are very close, we distinguished those modes by the polarized selection rules and their intensities because the B_{2g} modes are expected to be significantly weaker than the A_{1g} modes [**15**]. So, in the Ⅰ configuration, these two Raman peaks are attributed to the A_{1g} mode; in Ⅱ and Ⅲ configurations, they are attributed to the B_{2g} modes. Based on the A_{1g} Raman tensor, the 100.5 and 442.7 cm^{-1} peaks should also appear in the Ⅳ configuration but we didn't observe them. This phenomenon was also reported by Iliev *et al.* [**15**] on an orthorhombic structure. The *a*-GaN epilayers has also reported the Raman tensors of C_{6V}^{4} symmetry breaking to C_{2V} symmetry when the strained anisotropy arrives $|\varepsilon_{xx}-\varepsilon_{yy}|\sim 6\times10^{-3}$ [**16**]. Besides, the broad peak at ~340 cm^{-1} appears in Ⅰ and Ⅳ configurations that also attributed to the A_{1g} mode from the Raman tensor. The observed polarization dependence of the Raman spectra of the *a*-ZnO epi-layer is consistent with the breaking of C_{6V}^{4} symmetry and the polarization selection rules of an orthorhombic structure with C_{2V} symmetry.

4.4.2 Optical emission properties of a-ZnO

Due to the wurtzite symmetry breaking, we would expect different optical properties of biaxially strained *a*-ZnO films from that of ZnO bulk. To further examine the influence of symmetry change on the optical properties of ZnO films, we performed optical reflectance (OR) measurement at 13 K as presented in Fig. 4-8(a). Two transitions at 3.402 and 3.440 eV were observed respectively in $E \perp c$ and $E \parallel c$ configurations and their energies are larger than those of the *A*, *B*, and *C* excitons of bulk ZnO [**2, 4**]. We assigned the former to E_1 and the latter to E_2 transitions [**2, 4**]. There are a lot of reports shown that the strain states in ZnO layers also influence on the exciton transition energy, the trend of free-exciton transition energy with strain ε_{zz} variation state in polar ZnO is linear increasing [**17-20**]. On the other hand, the free exciton transition energies decrease with increasing the biaxial tensile strain. The biaxial strain is tensile ($\varepsilon_{xx}, \varepsilon_{yy} > 0$) and strain of *c*-axis is compressive ($\varepsilon_{zz} < 0$) in our *a*-ZnO epilayers, the trend of optical transition energy is opposite to the rule of free exciton transitions that should be red-shift with biaxial tensile strain. However, the crystal symmetry changed from C_{6V} to C_{2V} satisfying the trend of the change of exciton transition energies to E_1 and E_2 bands, which are the special transition bands based on the C_{2V} symmetry. The contradicted trend of the free exciton transition energies in our result confirms the anisotropic strains make the crystal symmetry breaking of wurtzite (C_{6V}^4) to the orthorhombic (C_{2V}). Furthermore, the E_1 and E_2 emissions were also observed in PL spectra. Shown in Fig. 4-8(b) are the polarized PL spectra taken with the polarization angle Φ at 0°, 30°, 60°, and 90° with respect to the crystalline *c*-axis. The increasing intensity ratio of the main PL peaks at 3.386 and 3.358 eV as increasing Φ is also complied with the

polarization selection rules for E_1 and E_2 transitions [**2**]. The particular PL peaks energies show different from PL transition peaks for hexagonal ZnO. The change of optical transitions results from the anisotropic strains that make the crystal symmetry breaking of C_{6V}^4 (Hex.) to C_{2V} (Orth.).

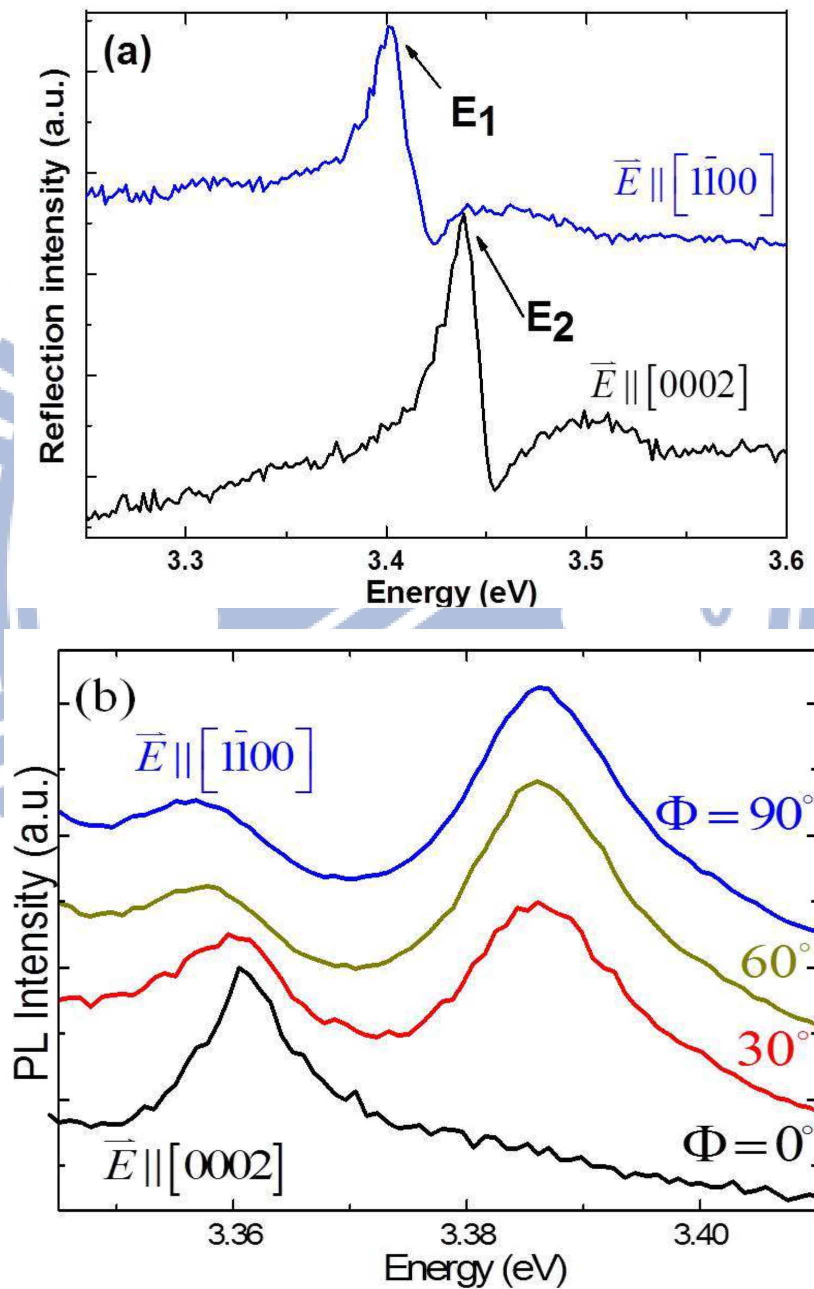

Fig. 4-8 (a) polarized optical reflection and (b) polarized PL spectra of the *a*-ZnO epi-layer taken in various polarization configurations at 13K.

Moreover, the biaxial anisotropic strain in the films could be dependent on the thickness of the ZnO and on the specific deposition conditions. In the case of ZnO grown on r-sapphire, the thickness for full structure relaxation is typically in the order of a few microns due to the large mismatches in lattice constants and thermal expansion coefficient. In addition to our ZnO/*r*-sapphire system (15 nm $<$ thickness $<$ 1.2 μm), similar symmetry change has been reported on systems grown by MOCVD (300 nm $<$ thickness $<$ 2 μm) and by PLD (thickness ~ 1 μm) [**2, 7, 21**]. Besides, same observation was also reported on wurtzite GaN grown on *r*-sapphire. As the layer thickness does not exceed a few microns, above which the film may recover the bulk wurtzite structure, the observed symmetry change is a common phenomena and not sensitive to the growth method and the details of deposition conditions.

4.5 Summary

The nonpolar *a*-ZnO films on *r*-sapphire have significant residual anisotropic strains induced by lattice and thermal expansion mismatches. The XRD results reveal *a*-ZnO epilayers on R-sapphire with a small tilting angle and show in-plane anisotropic biaxial strain. As determined by XRD and Raman spectra, the lattice of ZnO epi-layers grown at high temperatures is more relaxed. The in-plane anisotropic strain causes crystal symmetry breaking from wurtzite (C_{6V}^4) to orthorhombic (C_{2V}). This is a common phenomenon for *a*-ZnO and *a*-GaN epi-layers grown on *r*-sapphire with thickness not exceeding a few microns, above which the film may recover the bulk wurtzite structure. This structure transformation accounts for the observed blue-shifted $E_2^{(high)}$ Raman mode of the ZnO epi-layer subjected to a tensile strain in the basal plane. The violation of

selection rules observed in polarized Raman spectra is attributed to the change of crystal symmetry from hexagonal wurtzite structure to orthorhombic one and is also confirmed by PL and OR measurements. The PL and OR measurements observed for the E_1 and E_2 transitions, whose energies are larger than that of the bulk ZnO. The polarization dependence of polarized Raman, OR and PL spectra all agree with the polarization selection rules associated with C_{2V} symmetry.

References

1. J.-M. Chauveau, P. Vennégués, M. Laügt, C. Deparis, J. Zuniga-Perez, and C. Morhain, J. Appl. Phys. **104**, 073535 (2008).

2. T. Koida, S. F. Chichibu, A. Uedono, T. Sota, A. Tsukazaki and M. Kawasaki, Appl. Phys. Lett. **84**, 1079 (2004).

3. Y. S. Nam, S. W. Lee, K. S. Baek, S. K. Chang, J.-H. Song, J.-H. Song, S. K. Han, S.-K. Hong, and T. Yao Appl. Phys. Lett. 92, 201907 (2008).

4. S. Ghosh, P. Waltereit, O. Brandt, H. T. Grahn, and K. H. Ploog, Phys. Rev. B **65**, 075202 (2002).

5. B. Gil and A. Alemu, Phys. Rev. B **56**, 12446 (1997).

6. B. P. Zhang, Y. Segawa, K. Wakatsuki, Y. Kashiwaba and K. Haga. Appl. Phys. Lett., 79, 3953, (2001).

7. G. Saraf, Y. Lu,and T. Siegrist Appl. Phys. Lett. 93, 041903 (2008).

8. S. Zhou, J. Zhou, T. Huang, S. Li, J. Zou, J. Wang, X. Zhang, X. Li, and Rong Zhang, J. Cryst. Growth **303**, 510 (2007).

9. S. Tripathy, S. J. Chua, P. Chen, and Z.L.Miao, J. Appl. Phys. **92**, 3503 (2002).

10. G. W. Cong, H. Y. Wei, P. F. Zhang, W. Q. Peng, J. J. Wu, X. L. Liu, C. M. Jiao, W. G. Hu, Q. S. Zhu, and Z. G. Wang, Appl. Phys. Lett. **87**, 231903 (2005).

11. J. M. Wagner and F. Bechstedt, Phys. Rev. B **66**, 115202 (2002).

12. E.W. Stephen, B. C. Norman, H.D. Lawrence, *Introduction to Infrared and Raman Spectroscopy p.135* (Academic Press, New York, 1965).

13. J. M. Calleja and M. Cardona Phys. Rev. B **16**, 3753 (1977).

14. F. Decremps, J. Pellicer-Porres, A.M. Saitta, J. -C. Chervin, and A.Polian, Phys. Rev. B **65**, 092101 (2002)

15. M. N. Iliev, M. V. Abrashev, H.-G. Lee, V. N. Popov, Y. Y. Sun, C. Thomsen, R. L. Meng, and C. W. Chu, Phys. Rev. B **57**, 2872 (1998).

16. M. Katsikini, J. Arvanitidis, D. Christofilos, S. Ves, G. P. Dimitrakopulos, G. Tsiakatouras, K. Tsagaraki, and A. Georgakilas, Phys. Status Solidi A **209**, 1085 (2012).

17. Th. Gruber, G. M. Prinz, C. Kirchner, R. Kling, F. Reuss, W. Limmer, and A. Waag, J. Appl. Phys., **96**, 289 (2004).

18. T. Makino, T. Yasuda, Y. Segawa, A. Ohtomo, K. Tamura, M. Kawasaki, and H. Koinuma, Appl. Phys. Lett., **79**, 1283 (2001).

19. A. B. M. A. Ashrafi, N. T. Binh, B.-P. Zhang, and Y. Segawa, Appl. Phys. Lett., **84**, 2814 (2004).

20. A.B.M.A. Ashrafi, B.-P. Zhang, N.T. Binh, K. Wakatsuki, and Y. Segawa, J. Cryst. Growth **275**, 2439 (2005).

21. Y. S. Nam, S. W. Lee, K. S. Baek, S. K. Chang, J. H. Song, J. H. Song, S. K. Han, S. K. Hong, and Takafumi, Appl. Phys. Lett. **92**, 201907 (2008).

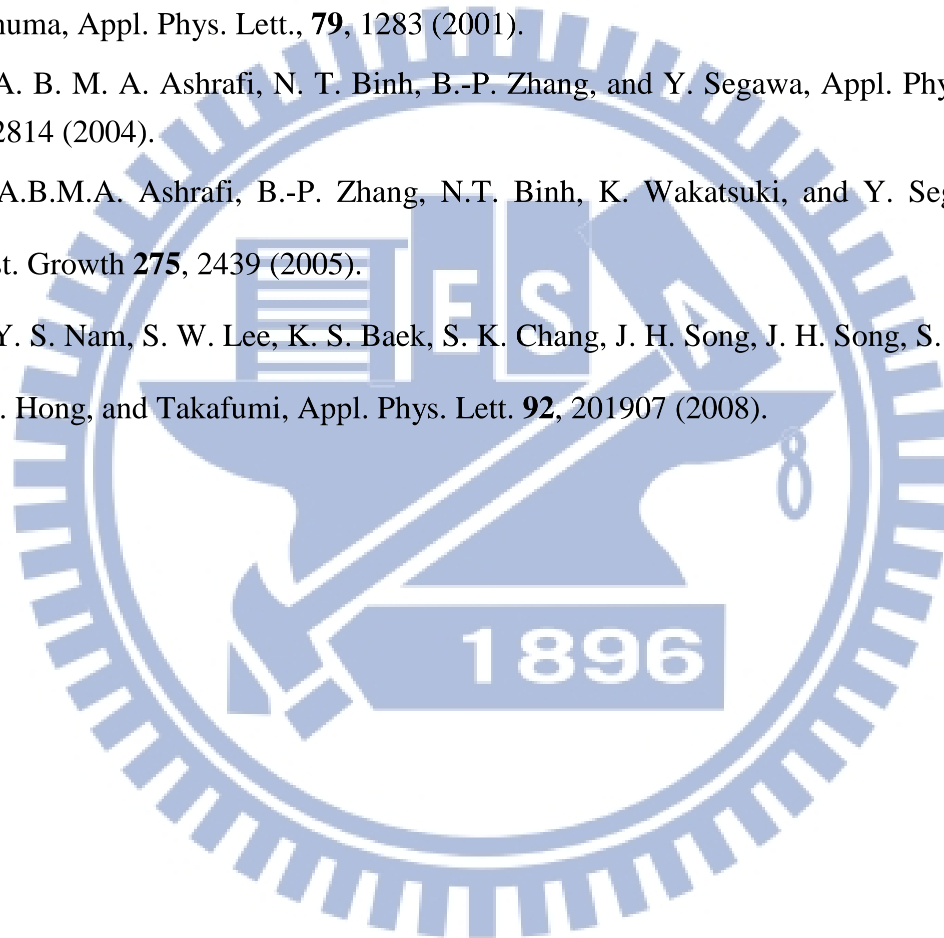

Chapter 5 Influence of extra domain on crystalline and optical properties in nonpolar *m*-ZnO epifilms on *m*-sapphires

5.1 Introduction

In order to reduce the quantum-confined Stark effect (QCSE), due to the piezoelectric and spontaneous polarizations along the growth direction consisting of Zn and O layer-by-layer to improve the quantum efficiency of optoelectronic devices, growth of non-polar ZnO, such as *a*-plane $(11\bar{2}0)$ and *m*-plane $(1\bar{1}00)$, has been proposed. For the *a*-ZnO films grown on *r*-sapphire substrate, we showed in the previous chapter that the *a*-ZnO layers are subjected to significant anisotropic residual strain induced by the mismatches of lattice and thermal expansion [**1, 2**]. The in-plane anisotropic strain leads to the change of crystal symmetry from wurtzite toward orthorhombic. This symmetry transformation accounts for the observed distinct optical transition in polarized optical reflection and photoluminescence (PL) spectra [**2, 3**]. These effects are the drawbacks if one is planning to design quantum wells for ultraviolet (UV) light emitting devices (LED) and laser diodes (LD).

As to *m*-ZnO, previous works showed that it's difficult to grow high-quality ZnO epi-films on *m*-sapphire with pure *m*-plane orientation. Domains with (0002), $(1\bar{1}02)$ and $(1\bar{1}03)$ orientations often coexist with the major $(1\bar{1}00)$ oriented ones [**4-8**]. However, rare report on the epitaxial relationship of the extra domain with the *m*-ZnO matrix and no report, to the best our knowledge, correlating the existence of extra domain with the optical property of *m*-ZnO films. Therefore, in this chapter, we first determine the epitaxial relationship of the extra domain and the *m*-ZnO by XRD and evaluate the extra domain content from the peak intensity ratio of the extra

domain to the *m*-ZnO. Determination of crystal axes of both the *m*-ZnO and extra domain is essential for investigating polarized PL with respect to the crystal structure. We observed a broad-band emission at ~ 3.17 eV, which may result from the interface defects trapped excitons at the boundaries between the $(1\bar{1}03)_{ZnO}$ domains and the *m*-ZnO matrix, is strongly correlated with the extra domain content.

5.2 The crystal properties of *m*-ZnO on *m*-plane sapphire

Figure 5-1 illustrates the typical scattered intensity distribution of a XRD radial scan along the surface normal at different growth temperature. Pronounced diffraction peaks of ZnO $(1\bar{1}00)$, $(2\bar{2}00)$ and sapphire $(3\bar{3}00)$ reflections confirm the *m*-plane orientation of the ZnO film. The red curve in Fig. 5-1(a) is the radial scan of the *m*-plane sapphire wafer. In addition, a broad shoulder and evident peak at ~ 4.253 (Å^{-1}) in Figs. 5-1(a) and (b) respectively, close to the angular position of ZnO $(1\bar{1}03)$ reflection, indicates the possible existence of extra domains with $(1\bar{1}03)$ normal. From XRD radial scan data, Fig. 5-1(a) shows the weaker and broad shoulder of the $(1\bar{1}03)_{ZnO}$ when growth at 500℃; as grown at 400℃, Fig. 5-1(b) shows outstanding and shaper peak with respect to Fig. 5-1(a). It implies the dependence of amount of extra $(1\bar{1}03)_{ZnO}$ domains on the growth temperature. On the other hand, the azimuthal scan across the *m*-ZnO off-normal $\{10\bar{1}0\}$ reflections, depicted in the inset of Fig. 5-2, show two sets of peaks rotating 90° from each other. The intense pair with their angular positions coinciding with those of sapphire {0006} reflections are the $(10\bar{1}0)$ and $(01\bar{1}0)$ reflections of the *m*-ZnO layer which are 180 degree apart, manifesting the $(1\bar{1}00)[11\bar{2}0]_{ZnO} \parallel (1\bar{1}00)[0001]_{sapphire}$ epitaxial

relationship. These two weak peaks are attributed to the $(1\bar{1}00)$ reflections originating from two extra $(1\bar{1}03)$-oriented domains, whose $[1\bar{1}03]$ axes are titled away from the surface normal by ~1° toward the ±*c*-axis of the *m*-ZnO layer, respectively. This ~1° tilting may easily lead to the missing of the $(1\bar{1}03)_{ZnO}$ domains if judging from the commonly performed $\theta-2\theta$ scan alone. Comparing with the different growth temperature samples from Fig. 5-1 and Fig. 5-2, the intensity ratios of the surface normal and the off normal peaks for the main *m*-ZnO and extra $(1\bar{1}03)_{ZnO}$ domains differ by about triple; the *m*-ZnO film grown at 400℃ has larger percentage of extra $(1\bar{1}03)$-oriented domains than grown at 500℃. The differences of those strains between $(1\bar{1}00)_{ZnO}$ and $(11\bar{2}0)_{ZnO}$ for all of the *m*-ZnO films are smaller than 6×10^{-3}. Notice that the anisotropic strain achieves this value should break the crystal symmetry from wurtzite structure to an orthorhombic one [**9**].

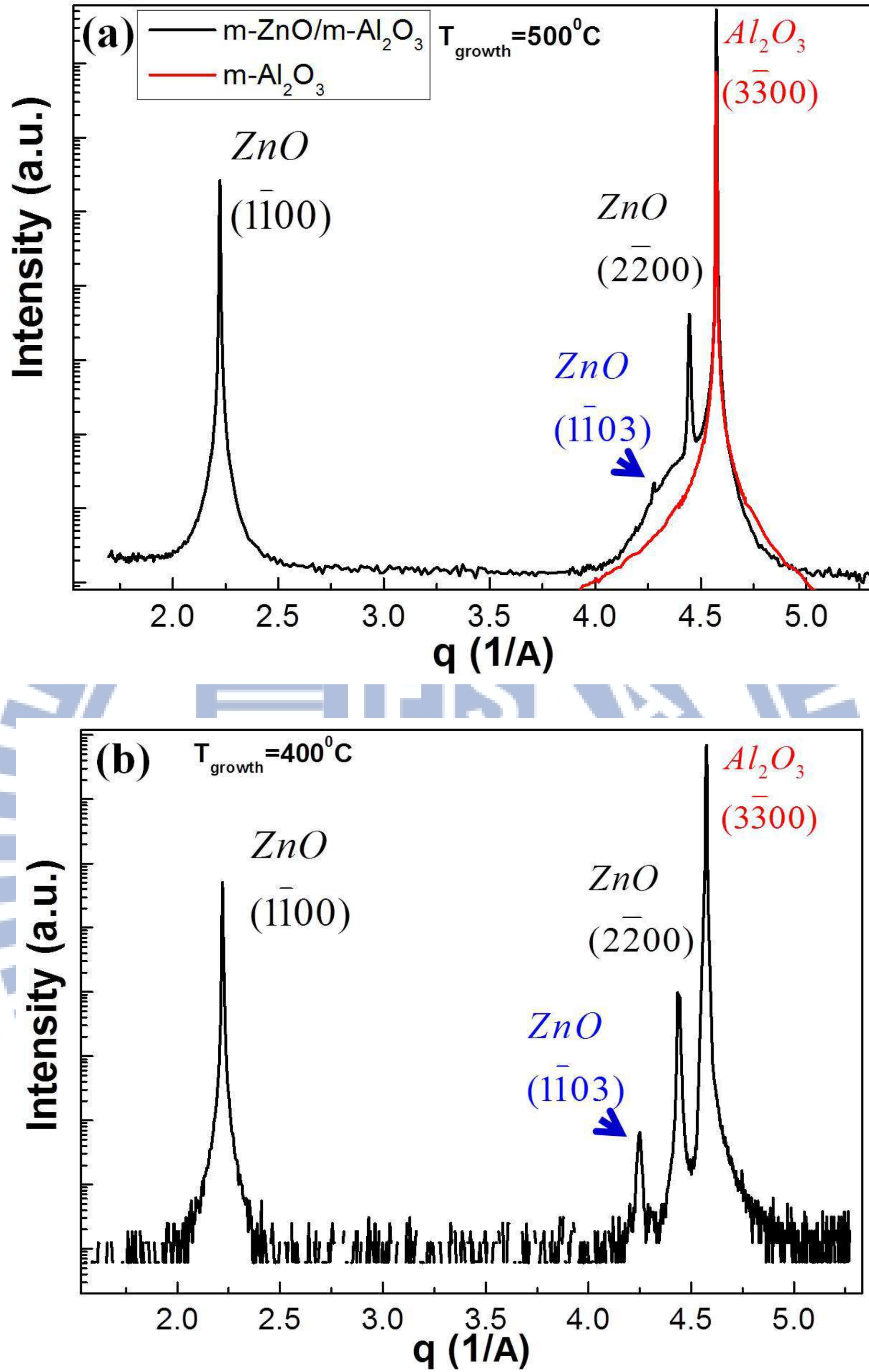

Fig. 5-1 XRD radial scans along the surface normal of *m*-ZnO/*m*-sapphire grown at two temperatures. (a) 500℃ and (b) 400℃. The red curve is the radial scan of *m*-sapphire wafer.

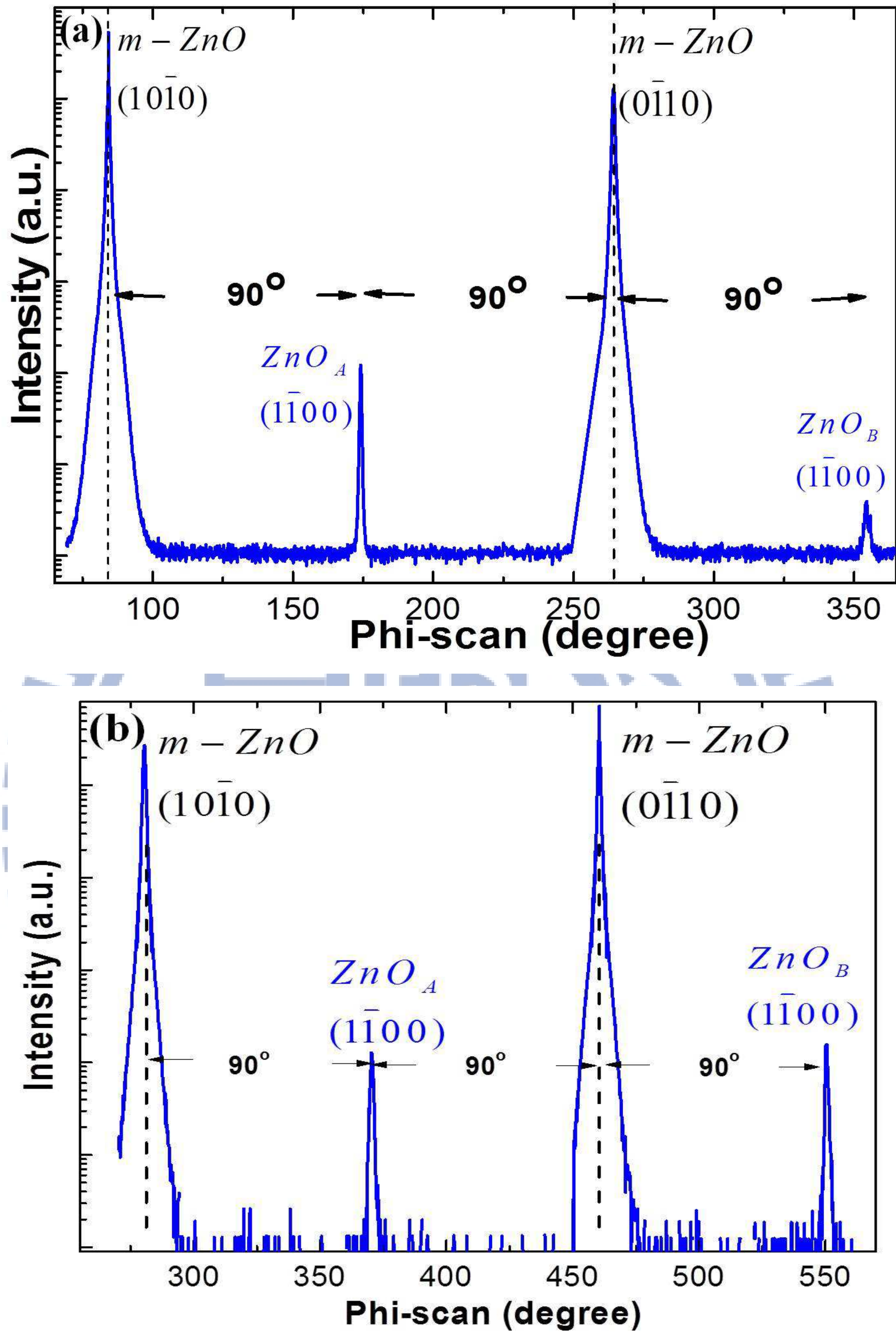

Fig. 5-2 Azimuthal scans across *m*-ZnO $\{10\bar{1}0\}$ off-normal reflections for growth temperatures at (a) 500℃ and (b) 400℃. The angular positions of sapphire{0006} reflections are marked by dashed lines as references.

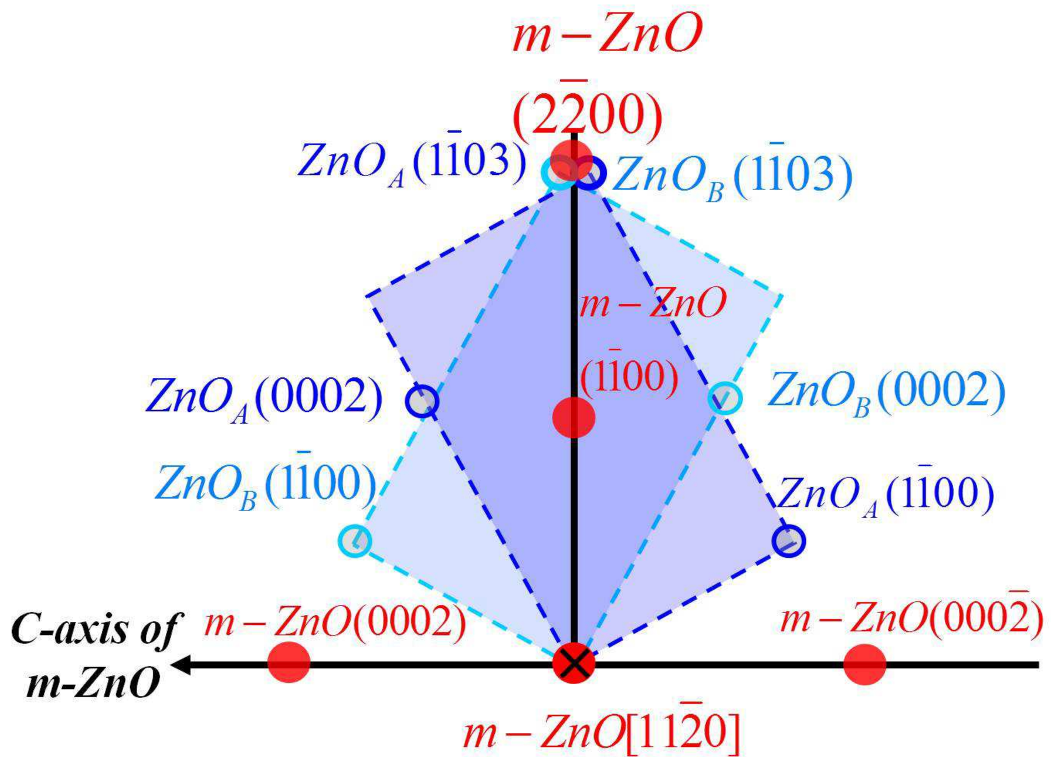

Fig. 5-3 Schematic of the diffraction pattern plotted along the $[11\bar{2}0]_{ZnO}$ zone axis. The Bragg reflections associated with the *m*-ZnO matrix and $(1\bar{1}03)_{ZnO}$ domains are depicted by red solid-circles and blue hollow-circles, respectively. Two $(1\bar{1}03)_{ZnO}$ domains share the same $[11\bar{2}0]_{m-ZnO}$ axis with the *m*-ZnO matrix but are rotated by ±59° around the $[11\bar{2}0]_{ZnO}$ axis, respectively.

After further analysis, we found the $(11\bar{2}0)$ planes of the *m*-ZnO matrix and the $(1\bar{1}03)$-oriented domains are parallel to each other. The relative orientations of the ZnO domains with respect to the sapphire substrate are illustrated in Fig. 5-3. A schematic of the diffraction pattern is on sapphire *h*-*k* plane. The red circles are the Bragg reflections of the main *m*-ZnO layer; the blue dash rectangles and open circles depict the two extra domains and the corresponding diffraction peaks. The cross

section along $[11\bar{2}0]_{ZnO}$ of the main domain and extra domains are labeled as *m*-ZnO domain by red circles and extra $(1\bar{1}03)$ domains by blue open-circles, respectively. The extra domains aligned along the $[11\bar{2}0]_{ZnO}$ axis of main domain and revolved about 60° around $[11\bar{2}0]_{ZnO}$ axis to both sides separately. Finally, the new epitaxial relationship of *m*-ZnO, extra domains and *m*-Al_2O_3 each other is rewritten by: $ZnO(1\bar{1}00) \| ZnO_{A,B}(1\bar{1}03) \| Al_2O_3(3\bar{3}00)$ and $ZnO[0002] \| ZnO_{A,B}[1\bar{1}0\bar{1}] \| Al_2O_3[11\bar{2}0]$. Judging from the content of $(1\bar{1}03)_{ZnO}$ domains and structural perfection of the *m*-ZnO matrix, we found the structural quality of the ZnO layers depends on the growth temperature; the sample grown at 500°C exhibits the best structure properties among the studied samples. The lattice constants of both the *a*- and *c*-axes of *m*-ZnO and $(1\bar{1}03)_{ZnO}$ domains derived from the XRD data are much less than 1% of the bulk values, showing small strains; the $(1\bar{1}03)_{ZnO}$ domains show the free strain within 0.12%. The existence of $(1\bar{1}03)_{ZnO}$ domains that behaves as a strain free provides space for strain relaxation of the *m*-ZnO matrix.

By comparing the XRD peak intensity of the near specular $(1\bar{1}03)_{ZnO}$ reflection of the $(1\bar{1}03)_{ZnO}$ domains and the specular $(1\bar{1}00)_{ZnO}$ reflection of the *m*-ZnO matrix, with taking into account the structure factor in Fig. 5-4, we estimated the intensity ratio of $(1\bar{1}03)_{ZnO}/(1\bar{1}00)_{ZnO}$ with various growth temperatures to be less than 3.8×10^{-4}. The intensity ratio of the *m*-ZnO and $(1\bar{1}03)_{ZnO}$ peaks is much lower than that in the powder diffraction pattern (JCPDS card 75-0576). Moreover, its content depends on the growth temperature, whose shape of the intensity ratio is dropped into

the center from both sides that is similar to Kim *et al.* [**4**]. We can see the sample grown at 500 °C shows the highest ratio with the least $(1\bar{1}03)_{ZnO}$, which implies the highest purity.

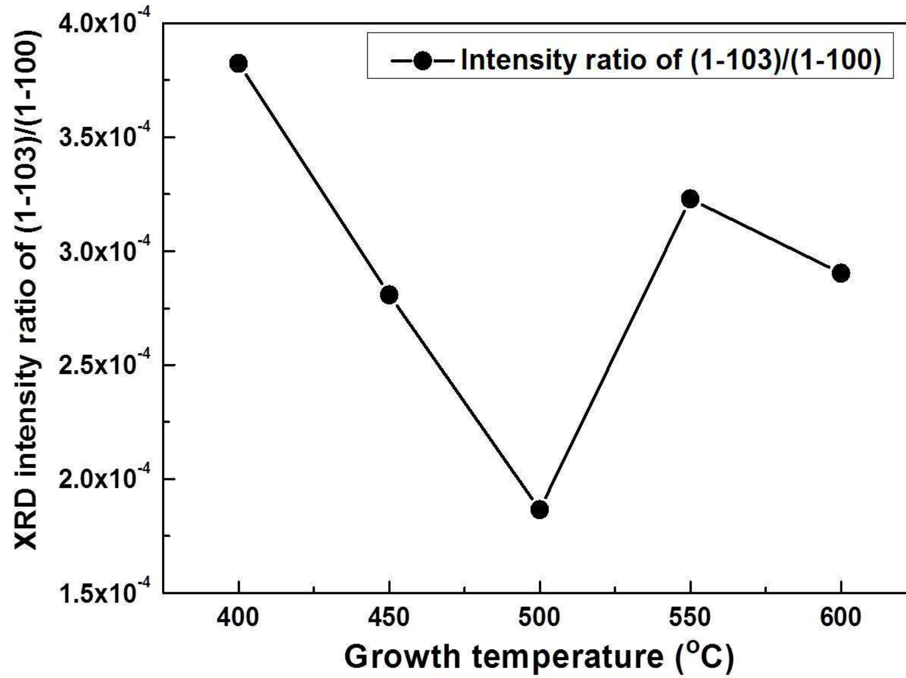

Fig. 5-4 Plots of the peak intensity ratio of $(1\bar{1}03)_{ZnO}/(1\bar{1}00)_{ZnO}$ with different growth temperature.

5.3 The defect states in *m*-ZnO

We also took cross-sectional TEM images under various geometries. Bright-field (BF) micrographs of the sample grown at 600°C recorded along the ZnO [0002] zone axis is shown in Fig. 5-5 (a). It has relatively high $(1\bar{1}03)_{ZnO}$ domains content and shows almost single domain or uniform image of ZnO layer. A selected area electron diffraction (SAED) pattern of the squared region near the *m*-ZnO/sapphire interface along ZnO $[11\bar{2}0]$ zone axis as Fig. 5-5(b) reconfirms the epitaxial

relationship determined by XRD. In contrast to the higher content of the $(1\bar{1}03)_{ZnO}$ -domain, the TEM image of the *m*-ZnO grown at 200°C by MBE in Fig. 7 of Ref. **4** shows the size of $(1\bar{1}03)_{ZnO}$ domain is ~50 nm having the XRD intensity ratio of $(1\bar{1}03)_{ZnO}/(1\bar{1}00)_{ZnO}$ of about 350, read from Fig. 3 of Ref. **4**. It corresponds to the $(1\bar{1}03)_{ZnO}/(1\bar{1}00)_{ZnO}$ intensity ratio of ~ 2.8×10^{-3}. No obvious feature associated with the $(1\bar{1}03)_{ZnO}$ domains is observed in our samples by both the BF TEM micrographs and the SAED patterns in Fig. 5-5 that manifests the relatively small size and low content of the $(1\bar{1}03)_{ZnO}$ domains. And the $(1\bar{1}03)_{ZnO}/(1\bar{1}00)_{ZnO}$ intensity ratio may be used as an indicator of the relative $(1\bar{1}03)_{ZnO}$ -domain content.

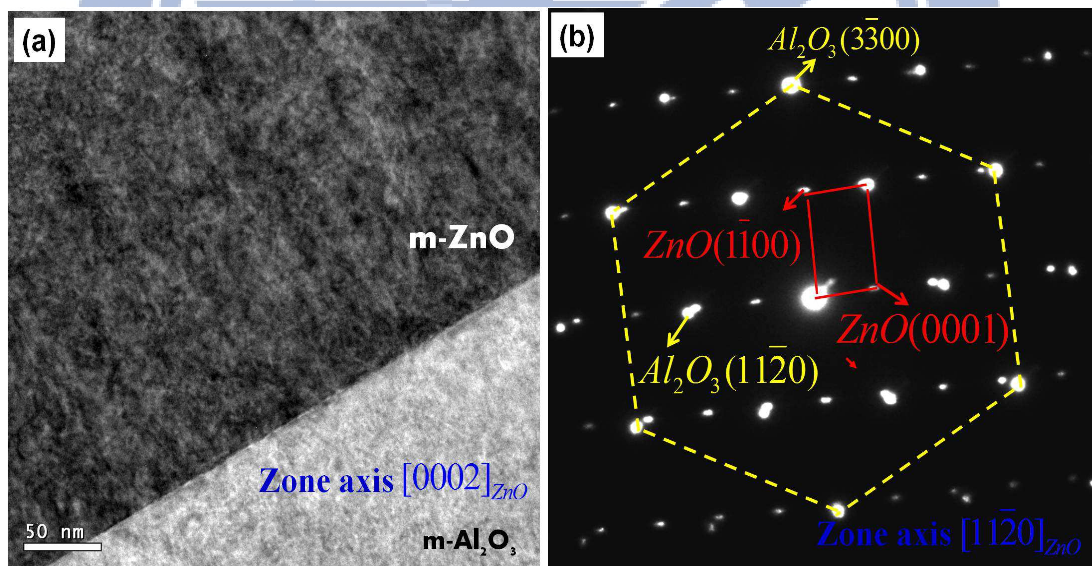

Fig. 5-5 A cross-sectional TEM bright field micrograph (a) and a SAED pattern (b), , taken at the *m*-ZnO/sapphire interface along the $[0002]_{ZnO}$ and $[11\bar{2}0]_{ZnO}$ zone axis. The lattices of *m*-ZnO and *m*-sapphire are marked, respectively, by solid and dashed lines.

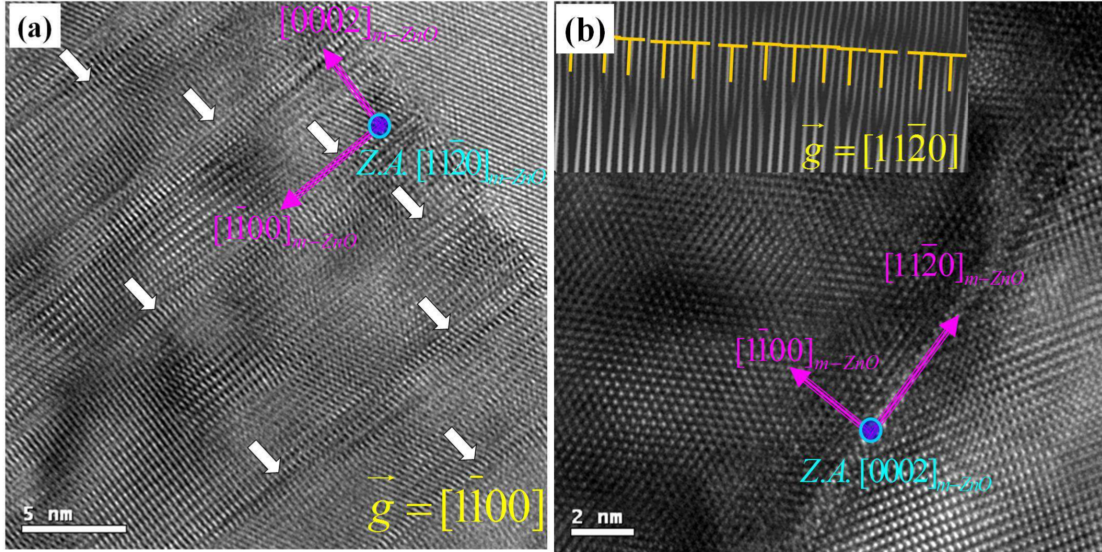

Fig. 5-6 The HRTEM micrographs taken along the (a) $[11\bar{2}0]_{ZnO}$ and (b) $[0002]_{m\text{-}ZnO}$ zone axis at *m*-ZnO/sapphire interface. The observed stacking faults in (a) were determined to be an intrinsic type-I_1 stacking fault. The inset in (b) shows a Fourier filtered image of the interface where the misfit dislocations are marked by ⊥.

It is well known that non-polar ZnO epi-films suffer from large density of stacking faults (SF) [**5, 10-14**]. There are four types of basal-plane SFs, which have been previously reported in wurtzite ZnO including the extrinsic SFs [**15, 16**]. According to the extinction rules, the stacking faults are out of contrast when $\bar{g} \bullet \bar{R}$ is equivalent to an integer. The appearance of these basal-plane SFs often accompanies various types of partial dislocations, including Frankel partial, Shockley partial (I_2) and Frankel–Shockley partial (I_1) dislocations having Burgers vector of $\vec{b} = \frac{1}{2}[0001]$, $\vec{b} = \frac{1}{3}\left[1\bar{1}00\right]$ and $\vec{b} = \frac{1}{6}\left[2\bar{2}03\right]$, respectively. Among them, the extrinsic SFs are present along with the Frankel partial dislocations [**14, 17**]. In *c*-plane and *a*-plane ZnO epilayers were reported the principal SFs are the Frankel partial with $\vec{b} = \frac{1}{2}[0001]$ and Frankel–Shockley partial with $\vec{b} = \frac{1}{6}\left[2\bar{2}03\right]$,

respectively. [**13, 14**] High resolution TEM images of the *m*-ZnO/sapphire interface were taken along two orthogonal zone-axes to examine the structure defects of the samples. In Fig. 5-6(a), taken with the $[11\bar{2}0]_{ZnO}$ zone axis and diffraction vector $\vec{g}=[1\bar{1}00]_{ZnO}$, many basal stacking faults (BSFs), marked by arrows, initiated from the ZnO/sapphire interface were identified. From the contrast analysis, the observed variation of dependent contrast indicates that the BSFs in the *m*-plane ZnO film belong to intrinsic type I_1 and/or I_2. We cannot further distinguish between these two types owing to insufficient information. However, Ref. 5 found the BSFs belong to intrinsic Frankel–Shockley partial dislocations (type-I_1) with a Burgers vector $\vec{b}=\frac{1}{6}\left[\bar{2}203\right]$ from HRTEM. This type of SFs has the lower energy from the theoretical calculation and experiment result [**18, 19**]. The density of BSFs is estimated to be $\sim 5\times10^5\,\mathrm{cm}^{-1}$, similar to what reported in other works [**11, 12**]. The micrograph recorded along $(0002)_{ZnO}$ zone axis with $\vec{g}=\left[11\bar{2}0\right]_{ZnO}$, shown in Fig. 5-6(b), reveals the highly perfect atomic arrangement of the ZnO layer. The inset shows the Fourier filtered image of the interface region. The nearly periodically arranged misfit dislocations, noted by extra half-planes inserted in the ZnO film, illustrate the domain matching epitaxial (DME) growth with four $\left(11\bar{2}0\right)_{ZnO}$ planes matching three $\left(0006\right)_{sapphire}$ planes along the $\left[11\bar{2}0\right]_{ZnO}$ direction and the DME growth has significantly reduced the lattice mismatch to induce strain along this direction.

5.4 Optical properties associated with domain interfaces in *m*-ZnO

In order to investigate the influence of the $(1\bar{1}03)_{ZnO}$ domains to the optical properties of the *m*-ZnO epi-films, the low temperature PL (LT-PL) spectra taken at

13 K, shown in Fig. 5-7, of the samples grown at different temperatures were measured. The deep level emission centered around 2.2 eV, commonly known as the defect emissions attributed to the zinc interstitial or oxygen vacancies [**20-22**], is negligible. Two dominant features are observed in the spectra: a sharp near-band edge (NBE) emission centered around 3.36 eV and a weak broadband one around 3.17 eV noted as SX. The characteristic emission of ZnO BSFs is at 3.31 eV, whose shape similar to a Gaussian has full width at half maximum (FWHM) around 7 meV at low temperature [**23**] that can be thus ruled out as the origin of the SX band. The intensity of the broad SX emission exhibits strong sample dependence and is positively correlated with $(1\bar{1}03)_{ZnO}$ domain content. This correlation is demonstrated by the variation of the XRD intensity of the $(1\bar{1}03)_{ZnO}$ reflection associated with the $(1\bar{1}03)_{ZnO}$ domains normalized to that of the $(1\bar{1}00)_{ZnO}$ reflection associated with the *m*-ZnO (stars) and the intensity of the SX emission normalized to the NBE emission (filled circles), shown in the inset of Fig. 5-7. The two curves show similar trend as a function of sample growth temperature. Moreover, thermal annealing of the 450°C sample at 850°C in 1 atm oxygen ambient for two hours significantly suppresses the SX band in the PL spectrum, depicted by the black curve in Fig. 5-7. It is accompanied with a more than 60% decrease of the XRD intensity of the reflections associated with the $(1\bar{1}03)_{ZnO}$ domains relative to that with *m*-ZnO. These observations obviously reveal that the origin of the SX band is related to the $(1\bar{1}03)_{ZnO}$ domains and thermal treatment effectively diminishes the $(1\bar{1}03)_{ZnO}$ domain content.

Because both the *m*-plane and $(1\bar{1}03)_{ZnO}$ oriented ZnO have the same crystalline structure with small strain, they are not expected to give rise to distinct PL features.

The SX band is thus unlikely to originate from the $(1\bar{1}03)_{ZnO}$ domain itself. In light of the previous study of ZnO nanowires, Reparaz *et al.* [**24**] attributed the broad band in the PL spectra to the surface-bound exciton (SX) emission which shifted to the low energies accompanied by increasing emission intensity as the wire diameter decreased. The surface-bound states and defects localized in the interface between $(1\bar{1}03)_{ZnO}$ and $(1\bar{1}00)_{ZnO}$ regions may be responsible for the SX emission at 3.17 eV in this case.

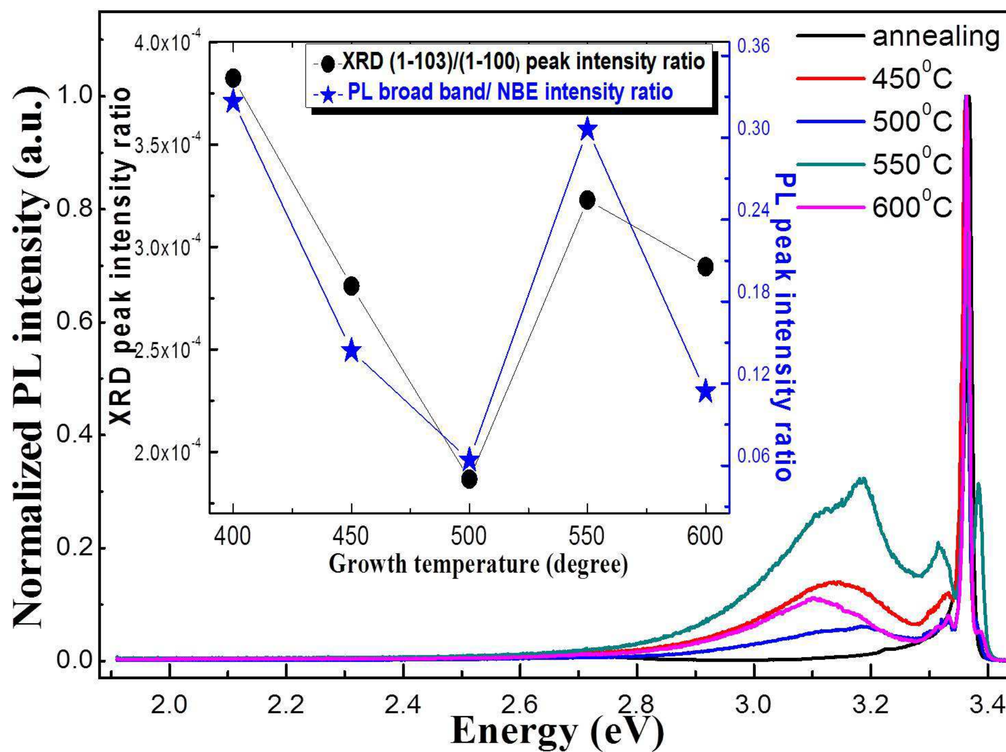

Fig. 5-7 PL spectra of the samples grown at different temperatures measured the spectra show a strong NBE and a broad-band emission without the deep level transitions. A spectrum of the sample annealed at 850°C in O_2 is depicted by the black curve, where the SX band is suppressed. The inset shows the XRD intensity ratio of the $(1\bar{1}03)_{ZnO}$ reflection associated with the $(1\bar{1}03)_{ZnO}$ domains to the $(1\bar{1}00)_{ZnO}$ reflection of the *m*-ZnO (●) and the PL intensity ratio of SX/NBE (★) as a function of sample growth temperature.

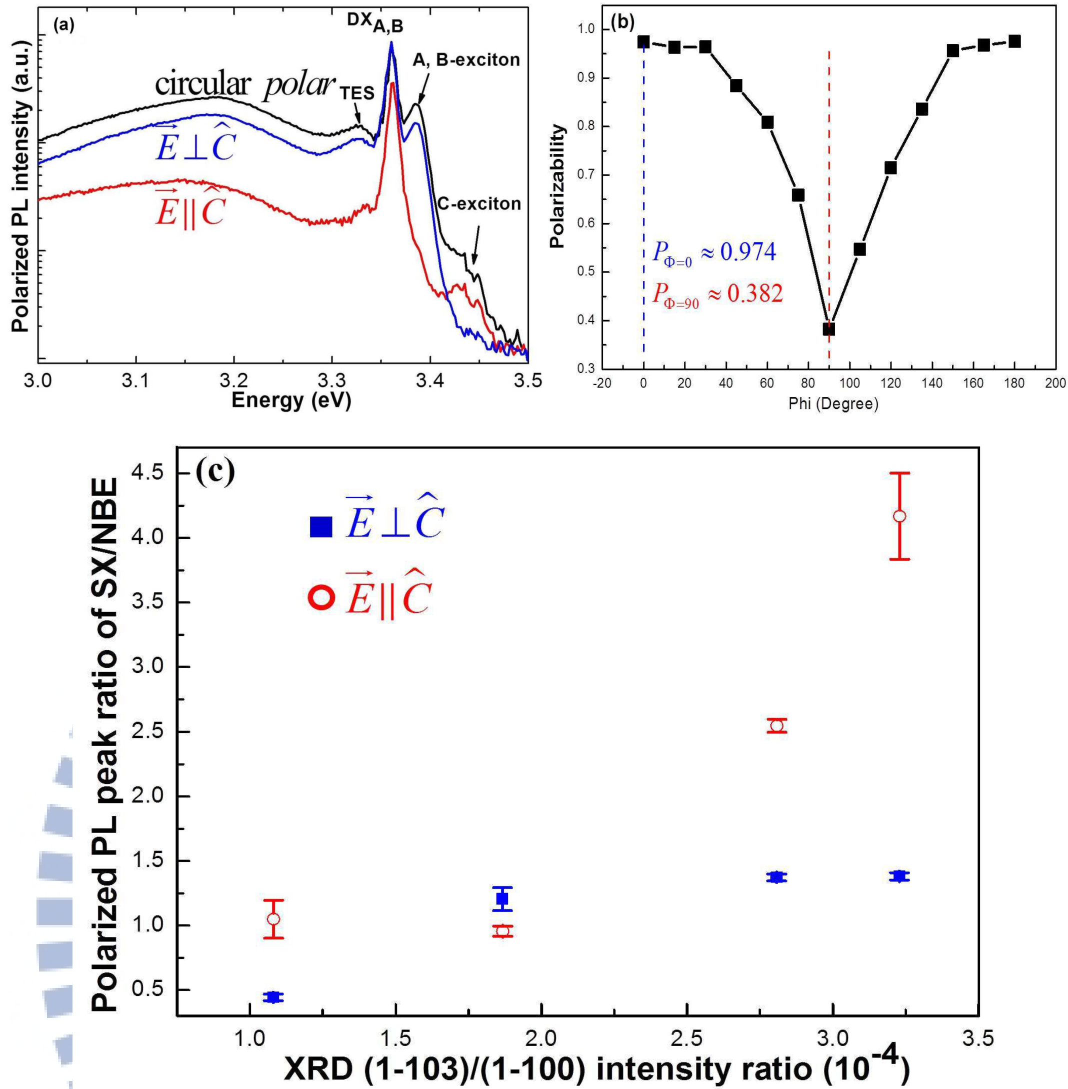

Fig. 5-8 (a) The polarized spectra of the sample grown at 450°C taken in various polarization configurations at 13 K and (b) the polarizability versus the excited polarization direction, where Φ=0° and Φ=0° mean the electric field vertical and parallel the *m*-ZnO *c*-axis. (c) The polarized PL peak (integrated) ratio of I_{SX}/I_{NBE} with different $(1\bar{1}03)_{ZnO}$ content at 13K.

We also compared the XRD θ-2θ scans of the annealing and the as-grown samples and found the FWHMs of *m*-ZnO peaks decrease obviously after annealing. It is attributed to grain-size increase and strain relaxation. Note that the strains of the as-grown samples have already been much less than 1%. However, the FWHM of

$(1\bar{1}03)_{ZnO}$ domains showing strain free according to the as-grown radius scan has slightly increased after annealing. With decreasing the $(1\bar{1}03)_{ZnO}$ domain content and grain size in *m*-ZnO epilayers by different growth conditions and thermal treatment, the diminished SX emission at 3.17 eV conspicuously results from reducing the surface-bound states attributed to the interface defects in Fig. 5-7.

To further examine the nature of the emissions, we performed polarized LT-PL measurements. Figure 5-8(a) illustrates the polarized LT-PL spectra of the 450°C-grown sample, Fig. 5-8(b) is the polarizability dependent on the polarized excitation and Fig. 5-8(c) shows the LT-PL peak ratio of I_{SX}/I_{NBE} dependent on the $(1\bar{1}03)_{ZnO}$ domains content with different polarized measurements. The exciton peaks located at 3.379, 3.388 and 3.443 eV are, respectively, attributed to free A-, B- and C-excitons (FX_A , FX_B and FX_C) in Fig. 5-8(a). The other NBE emission around 3.36 eV is originated from the neutral donor-bound excitons; the emission band at 3.33 eV is ascribed to the two-election satellite (TES) and phonon transition. The neutral donor should be attributed to the element of Cd and Ca from the chemical analysis of the ZnO target. It is known that the FX_A and FX_B are excited when the excitation polarization is perpendicular to the *c*-axis (E⊥c) of ZnO, whereas the FX_C is active when the polarization is parallel to the *c*-axis (E||c). We can calculated the degree of polarization: $P = \left(I_{\perp C} - I_{\parallel C} \right) / \left(I_{\perp C} + I_{\parallel C} \right)$, where $I_{\perp C}$ and $I_{\parallel C}$ are the intensity of excitation polarization vertical and parallel to the *c*-axis of *m*-ZnO in Fig. 5-8(b). The degrees of polarization are 0.974 and 0.382 when excited polarization is vertical and parallel to the *c*-axis, which is sensitive to the excited polarization. According to the crystalline orientation determined by XRD, the E-field is perpendicular to the *c*-axes of both the $(1\bar{1}03)_{ZnO}$ and $(1\bar{1}00)_{ZnO}$ regions in the E⊥c geometry and thus the

FX_A/FX_B emission is pronounced but the FX_C is not visible. In the E||c geometry, the E-field is parallel to the *c*-axis of *m*-ZnO but has a component of sin(χ), where χ ~59° is the angle made between the *c*-axes of the *m*-ZnO and $(1\bar{1}03)_{ZnO}$ domains, projected onto the $[1\bar{1}00]$ axis of the $(1\bar{1}03)_{ZnO}$ domains. Therefore, in additional to the FX_C emission mainly coming from the *m*-ZnO, there exist a tiny bump at 3.379 eV corresponding to the FX_A/FX_B emission from the $(1\bar{1}03)_{ZnO}$ domains, whose weak intensity again reveals the small content of the $(1\bar{1}03)_{ZnO}$ domains. The relative intensities of the FX emissions confirm the much larger absorption cross-sections of the FX_A/FX_B than the FX_C.

To confirm the SX emission is correlated with the content of $(1\bar{1}03)_{ZnO}$ domains, we compared the peak (integrated) ratio (I_{SX}/I_{NBE}) of SX to NBE emissions under different polarization excitations with the XRD intensity ratio of $(1\bar{1}03)_{ZnO}/(1\bar{1}00)_{ZnO}$ in Fig. 5-8(c). We found the increase in I_{SX}/I_{NBE} as increasing $(1\bar{1}03)_{ZnO}/(1\bar{1}00)_{ZnO}$ is shown for the E||c excitation, but is insensitive for the E⊥c excitation. Because both the *m*-ZnO matrix and $(1\bar{1}03)_{ZnO}$ domains being excited through both FX_A and FX_B transitions contribute strong NBE and SX emissions due to the large absorption cross-sections for these two domains for the E⊥c excitation, the value of I_{SX}/I_{NBE} is insensitive to variation of the $(1\bar{1}03)_{ZnO}/(1\bar{1}00)_{ZnO}$ or the content of $(1\bar{1}03)_{ZnO}$ domains. For the E||c excitation, the *m*-ZnO matrix excited the FX_C transitions was shown less NBE emission, the $(1\bar{1}03)_{ZnO}$ domains still existed partial higher absorption cross-sections of the FX_A/FX_B. The higher ratio of I_{SX}/I_{NBE} with the higher $(1\bar{1}03)_{ZnO}$ domain content and on the E||c condition shown the larger ratio of

I_{SX}/I_{NBE} result from the mainly SX emission attributed to the surface boundary in interface between $(1\bar{1}03)_{ZnO}$ domains and *m*-ZnO matrix. In this scenario, the PL peak ratio of I_{SX}/I_{NBE} reflects the probability of observing surface trapping emission and is consequently proportional to the boundary area between $(1\bar{1}03)_{ZnO}$ domains and *m*-ZnO matrix which is positively correlated with the $(1\bar{1}03)_{ZnO}$ domain content. The much higher I_{SX}/I_{NBE} in the E||c geometry should be related to the higher binding efficiency of excitons to the interfacial states originated from the $(1\bar{1}03)_{ZnO}$ domains due to the larger surface-to-volume ratio and smaller size of the $(1\bar{1}03)_{ZnO}$ domains.

5.5 Summary

Small amount of $(1\bar{1}03)_{ZnO}$ domains were found in the *m*-plane ZnO films grown on *m*-sapphire by pulsed laser deposition which provide strain relaxation of the *m*-ZnO matrix behaving as a low strain layer. The XRD results reveal the presence of small amount of $(1\bar{1}03)_{ZnO}$-oriented domains almost strain-free in the *m*-ZnO matrix with slightly strained and each other epitaxial relaxation ship between the extra $(1\bar{1}03)_{ZnO}$, *m*-plane ZnO and sapphire. And the *a*-axes of both the $(1\bar{1}03)_{ZnO}$ domains and the *m*-ZnO matrix are aligned with the *c*-axis of the sapphire substrate. The *c*-axis of the $(1\bar{1}03)_{ZnO}$ domains rotates by about ±59° against the common *a*-axis of the *m*-ZnO. The TEM results not only confirm the $(1\bar{1}00)$ plane dominates the ZnO film but also the strain-relaxation is achieved by the domain matching and extra $(1\bar{1}03)_{ZnO}$ domain along $[11\bar{2}0]$ and $[0002]$, respectively. We can clearly find many SFs from the interface of *m*-ZnO and *m*-Al_2O_3 along

$[11\bar{2}0]$ zone axis, which determined to be an intrinsic type-I ZnO basal-plane stacking fault. In the other direction, $[0002]$ zone axis, there are a lot of misfit dislocations, which are four $(11\bar{2}0)_{ZnO}$ planes matching to three $(0006)_{Al_2O_3}$ planes to relax crystal strain that confirms the results of XRD. The peak positions of the free A-, B- and C-exciton emissions in the PL spectra are close to that of bulk ZnO as a result of the $(1\bar{1}03)_{ZnO}$-oriented domains providing the strain relaxation mechanism. Through carefully correlating low-temperature polarized PL spectra with the XRD peak intensity ratio of $(1\bar{1}03)_{ZnO}/(1\bar{1}00)_{ZnO}$ of the samples grown at different temperatures and after thermal treatment, we found that the broad-band emission around 3.17 eV may result from the interface defects trapped excitons at the boundaries between the $(1\bar{1}03)_{ZnO}$ domains and the *m*-ZnO matrix. The broad-band emission is attributed to the emission from the surface-bound excitons (SX), which are captured on the boundaries between the *m*-plane and $(1\bar{1}03)_{ZnO}$-oriented domains. The more $(1\bar{1}03)_{ZnO}$ domains in the *m*-ZnO layer cause the more surface boundaries that makes the stronger SX emission. The larger surface-to-volume ratio for the more extra domains makes the SX emission increase.

References

1. G. Saraf, Y. Lu, and T. Siegrist, Appl. Phys. Lett. **93**, 041903 (2008).

2. C. C. Kuo, W.-R. Liu, W. F. Hsieh, C.-H. Hsu, H. C. Hsu, and L. C. Chen, Appl. Phys. Lett. **95**, 011905 (2009).

3. T. Koida, S. F. Chichibu, A. Uedono, T. Sota, A. Tsukazaki, and M. Kawasaki, Appl. Phys. Lett. **84**, 1079 (2004).

4. J.-H. Kim, S. K. Han, S. I. Hong, S.-K. Hong, J. W. Lee, J. Y. Lee, J.-H. Song, J. S. Park and T. Yao, J. Vac. Sci. Technol. B **27**, 1625, (2009).

5. J. W. Lee, J.-H. Kim, S. K. Han, S.-K. Hong , J. Y. Lee, S. I. Hong and T. Yao, J. Cryst. Growth **312**, 238 (2010).

6. E. Cagin, J. Yang, W. Wang, J. D. Phillips, S. K. Hong, J. W. Lee, and J. Y. Lee, Appl. Phys. Lett. **92**, 233505 (2008).

7. T. Moriyama and S. Fujita, Jpn. J. Appl. Phys., Part 1 **44**, 7919 (2005).

8. J. Zuniga-Perez, A. Rahm, C. Czekalla, J. Lenzner, M. Lorenz, and M. Grundmann, Nanotechnology **18**, 195303 (2007).

9. M. Katsikini, J. Arvanitidis, D. Christofilos, S. Ves, G. P. Dimitrakopulos, G. Tsiakatouras, K. Tsagaraki, and A. Georgakilas, Phys. Status Solidi A **209**, 1085 (2012).

10. J.-M. Chauveau, P. Vennéguès, M. Laügt, C. Deparis, J. Zuniga-Perez, and C. Morhain, J. Appl. Phys. **104**, 073535 (2008).

11. W.-L. Wang, C.-Y. Peng, Y.-T. Ho, S.-C. Chuang, and Li Chang, J. Vac. Sci. Technol. A **29**, 031001 (2011).

12. S. K. Han, J.-H Kim, S.-K. Hong, J.-H. Song, J.-H. Song, J. Wook Lee, J. Y. Lee, S. I. Hong, T. Yao, J. Cryst. Growth **312**, 2196 (2010).

13. S. K. Han, S-K Hong, J. W. Lee, J. G. Kim, M. Jeong, J. Y. Lee, S. I. Hong, J. S. Park, Y. E. Ihm, J.-S. Ha and Takafumi Yao, Thin Solid Films **519** , 6394 (2011)

14. K-P Liu, K-Y Yen, P-Y Lin, J-R Gong, K-D Wu and W-L Chen, J. Vac. Sci. Technol. A **29**,03A101-1, (2011).

15. C. Stampfl and Chris G. Van de Walle, Phys. Rev. B **57**, R15052 (1998).

16. Y. Yan, G. M. Dalpian, M. M. Al-Jassim, and S.-H. Wei, Phys. Rev. B **70**, 193206 (2004)

17. X. H. Wu, L. M. Brown, D. Kapolnek, S. Keller, B. Keller, S. P. Den-Baars, and J. S. Speck, J. Appl. Phys. **80**, 3228 (1996).

18. C. Stampfl and Chris G. Van de Walle, Phys. Rev. B **57**, 15052 (1998).

19. I. Tischer, M. Feneberg, M. Schirra, H. Yacoub, R. Sauer, K. Thonke, T. Wunderer and F. Scholz, Phys. Rev. B **83**, 035314 (2011).

20. T. Onuma, S. F. Chichibu, A. Uedono, Y. Z. Yoo, T. Chikyow, T. Sota, M. Kawasaki and H. Koinuma, Appl. Phys. Lett. **85**, 5586 (2004).

21. L. W. Sun, H. P. He, C. Liu, Y. F. Lu and Z. Ye. Cryst. Eng. Comm. **13**, 2439 (2011).

22. W.-R. Liu, B. H. Lin, S. Yang, C. C. Kuo, Y.-H. Li, C.-H. Hsu, W. F. Hsieh, W. C. Lee, M. Hong, and J. Kwo, CrystEngComm **14**, 1665 (2012).

23. M. Schirra, R. Schneider, A. Reiser, G. M. Prinz, M. Feneberg, J. Biskupek, U. Kaiser, C. E. Krill, K. Thonke, and R. Sauer, Phys. Rev. B **77**, 125215 (2008).

24. J. S. Reparaz, F. Güell, M. R. Wagner, A. Hoffmann, A. Cornet, and J. R. Morante, Appl. Phys. Lett. **96,** 053105 (2010).

Chapter 6 Eliminating extra domains in *m*-plane ZnO by two-step growth on *m*-sapphire

6.1 Introduction

In the Chapter 5, we have observed the extra domains in the direct growth *m*-ZnO epifilms on *m*-sapphires; the extra $(1\bar{1}03)_{ZnO}$-oriented domains are attributed to the strain relaxation mechanism along the *c*-axis of *m*-ZnO. The extra domains solve the strain problem at the interface of the ZnO layer and sapphire. However, the broad-band emission at 3.17 eV due to the surface-bound exciton (SX) emission, which is caused by the exciton being trapped to the domain boundaries. The trapping of carriers on the domain boundaries in nonpolar ZnO-based material is not in favor of photonic applications. Moriyama, *et al.* [**1**] had reported the metal-organic vapor phase epitaxy (MOVPE) grown *m*-ZnO/*m*-Al_2O_3 layers exhibit extra-$(1\bar{1}03)_{ZnO}$ domains only for growth temperature below 800℃. Unfortunately the highest growth temperature of our PLD system is about 650℃, so we must find some way to grow *m*-ZnO/*m*-Al_2O_3 with reducing lattice mismatching and the amount of extra domains.

Two-step growth by metal-organic chemical vapor deposition (MOCVD) has been developed to improve the crystalline quality of GaN-based films on sapphires [**2, 3**]. The high interfacial energy difference between epilayer and sapphire leads to an island growth that is commonly used for GaN, InN or AlN nucleation layers grown at low-temperature (LT). Thermal annealing of nucleation layer (NL) before the high-temperature growth could enhance the lateral growth and suppress threading dislocations to improve the crystalline quality [**3-7**]. Several groups have demonstrated that the high-temperature growth over the LT-NL, known as the

two-step growth method, is also a key for achieving high-quality epilayers with reduction of the threading dislocation density and lattice mismatching [**3,8-10**]. The growth mechanism of MOCVD is unequal to PLD completely, but Nakahare, *et al.* [**11, 12**] have reported that using LT buffer layers grown at 200-400℃ by MBE can improve the surface morphology and crystal quality by thermal treatment at temperature higher than 700℃. Ko, *et al.* [**13, 14**] studied as-grown and annealed ZnO with LT-ZnO buffer on GaN templates grown by MOCVD on sapphire. The LT-ZnO buffer layers were grown at 250 to 300℃, and the surface morphology was dramatically improved by thermal treatment above 600℃. In this chapter, we will use two-step growth method for eliminating extra domains to reduce surface boundary trapped excitons. We will first grow single-phase *m*-ZnO at LT with temperature range from 150 to 350℃, and raise the growth temperature to improve crystal quality for growing main *m*-ZnO epilayer at 600℃.

The crystalline properties of LT-ZnO buffer will be studied first, then discussion of the main *m*-ZnO grown on high temperature (HT) at 600℃ with different thicknesses of LT-buffers will be presented. We also compare optical properties of two-step grown *m*-ZnO layers with Chapter 5, in which the samples were grown on m-sapphires at 600℃ without the LT-buffers. Finally, we demonstrate successful growth of 5 pairs of non-polar multiple quantum well (MQW) structures with well widths of 4, 8, and 16 nm on top of the two-step growth buffer layers. These MQW structures reveal quantum confinement effect with absence of the quantum confined Stark effect.

6.2 Structural properties of *m*-ZnO by two-step growth

6.2.1 Low temperature (LT) growth *m*-ZnO buffer layers

We grew the ZnO buffer layers on *m*-sapphires at low temperature (LT) ranging from 150 to 350℃ then thermally treated at various temperatures above 600℃. We found the optimal LT growth temperature is in the range of 150-200℃ to obtain the best crystal quality of the post HT-growth *m*-ZnO layers. Figure 6-1 is the XRD radial scan with different thicknesses of LT-ZnO buffers in the same growth conditions. The thicknesses of LT-buffers are around 4.7, 15.4, 58.3 and 156 nm, respectively, determined by X-ray reflection measurement. Their XRD surface-normal scans are respectively shown in Figs. 6-1(a)-(d). In addition to the XRD data, LT-buffers with thicknesses below 58.3 nm exhibit ZnO $(1\bar{1}00)$, $(2\bar{2}00)$, $(3\bar{3}00)$ and sapphire $(3\bar{3}00)$ plane reflections. The apparent interference fringes were observed from the thinner samples which result from the X-ray interference between two surfaces of LT-ZnO. The spacing of two closest fringes is inversely proportional to the film thickness. The thicker the LT-buffer, the more fringes are, but no fringes were observed with the thickness of LT-ZnO buffers over 58.3 nm in Figs. 6-1(c) and (d). We could not detect the extra $(1\bar{1}03)_{ZnO}$-reflection from Figs. 6-1(a)-(c), but observe outstanding $(1\bar{1}03)_{ZnO}$-reflection as the thickness of LT-ZnO reaches 156 nm in Fig. 6-1(d). We also found various thicknesses of LT-ZnO buffers, which show the existence of extra domains when the thickness of ZnO exceeds 67 nm. It is different from the results in Chapter 5, where extra domains were observed with *m*-ZnO film thickness reaching 40 nm as the growth temperature was set in the range of 400 to 600℃.

The off-normal azimuthal scans of these three thicknesses of LT-ZnO buffers shown in Figs. 6-2(a)-(c) all reveal $ZnO(10\bar{1}0)$ and $ZnO(0\bar{1}10)$ two reflection peaks, which are 180 degree apart. The sapphire {0006} reflections, marked by

yellow dashed line as reference and coincided with the sapphire {0006} reflections, are the $(10\bar{1}0)$ and $(01\bar{1}0)$ reflections of the *m*-ZnO. The LT-ZnO buffers grown on *m*-sapphire are still epitaxial, their the epitaxial relationship read $(1\bar{1}00)[11\bar{2}0]_{ZnO} \parallel (1\bar{1}00)[0001]_{sapphire}$ that is the same as the HT growth results in Chapter 5. In addition to the azimuthal scan shown in Fig. 6-2(c), whose thickness is ~ 156 nm, two strong peaks in the radial scan are attributed to two extra $(1\bar{1}03)_{ZnO}$ domains with 180 degree apart. The LT grown *m*-ZnO buffers show pure *m*-plane oriented without extra domains when the film thickness is below 67 nm, detectable extra $(1\bar{1}03)_{ZnO}$ domains appear for the thickness over 156 nm and their epitaxial relationships are similar to the HT growth *m*-ZnO/*m*-sapphire in Chapter 5. The thickest LT-ZnO buffer of ~ 156 nm showed even stronger extra domains than the HT *m*-ZnO/*m*-sapphire samples. The intensity ratio of the extra domains to the *m*-ZnO for the normal and lateral orientations are closed to 3.2×10^{-3} ($(1\bar{1}03)_{ZnO}/(1\bar{1}00)_{ZnO}$) and 2.8×10^{-3} ($(1\bar{1}00)_{ZnO}/(10\bar{1}0)_{ZnO}$) in thickest LT-ZnO buffer (~ 156 nm), which are larger than the HT *m*-ZnO/*m*-sapphire, which are less than 3.8×10^{-4} and 9.8×10^{-4}, respectively. The thicker the LT-buffer creates the more extra domains, so the optimal thickness of LT-buffer should be below 67 nm.

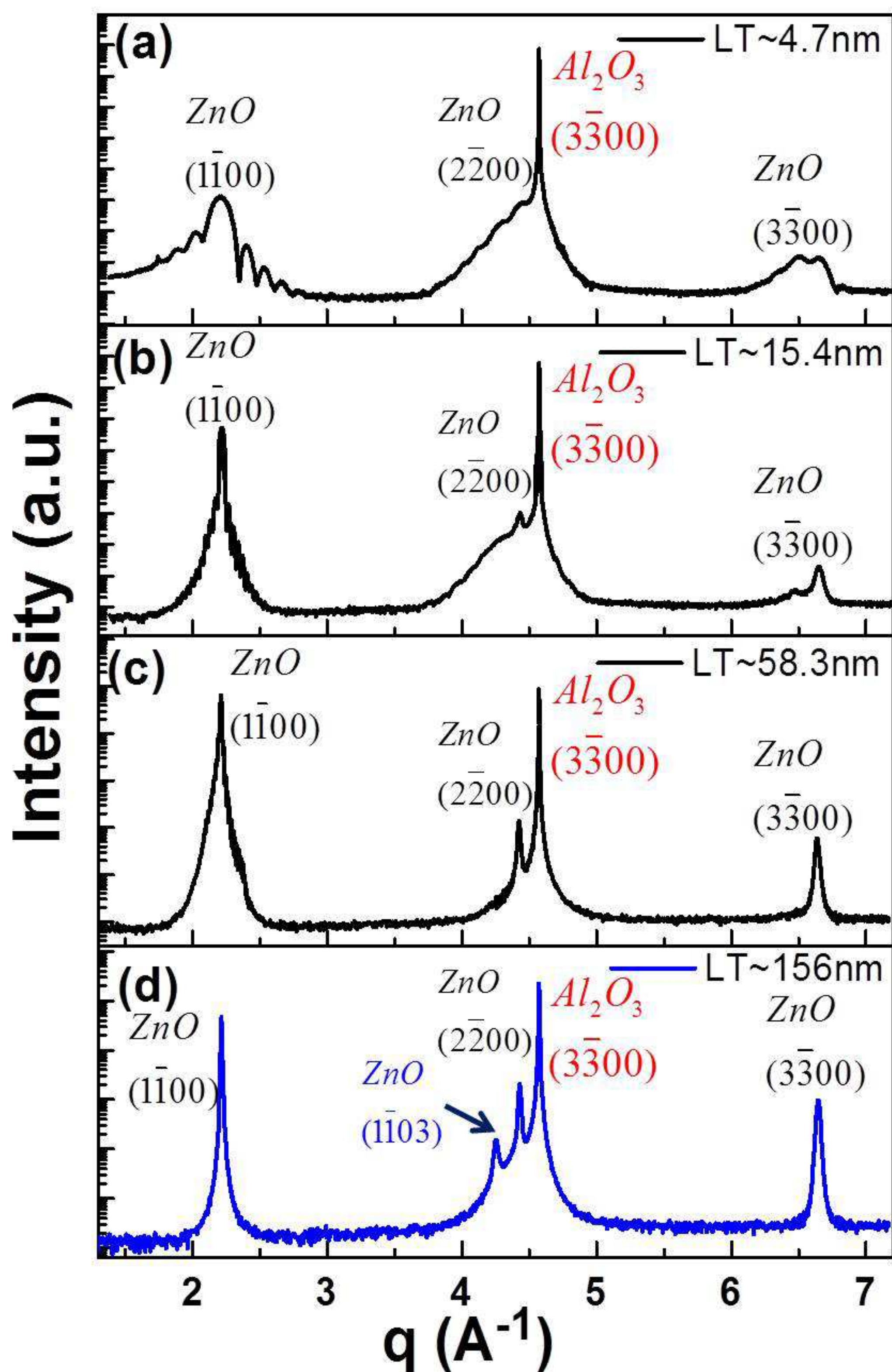

Fig. 6-1 The XRD radial scans of four thicknesses of LT-ZnO buffers grown at 175℃. The thicknesses are around (a) 4.7 nm, (b) 15.4 nm, (c) 58.3 nm, and (d) 156 nm, respectively. The extra domains are only observed for the 156nm sample.

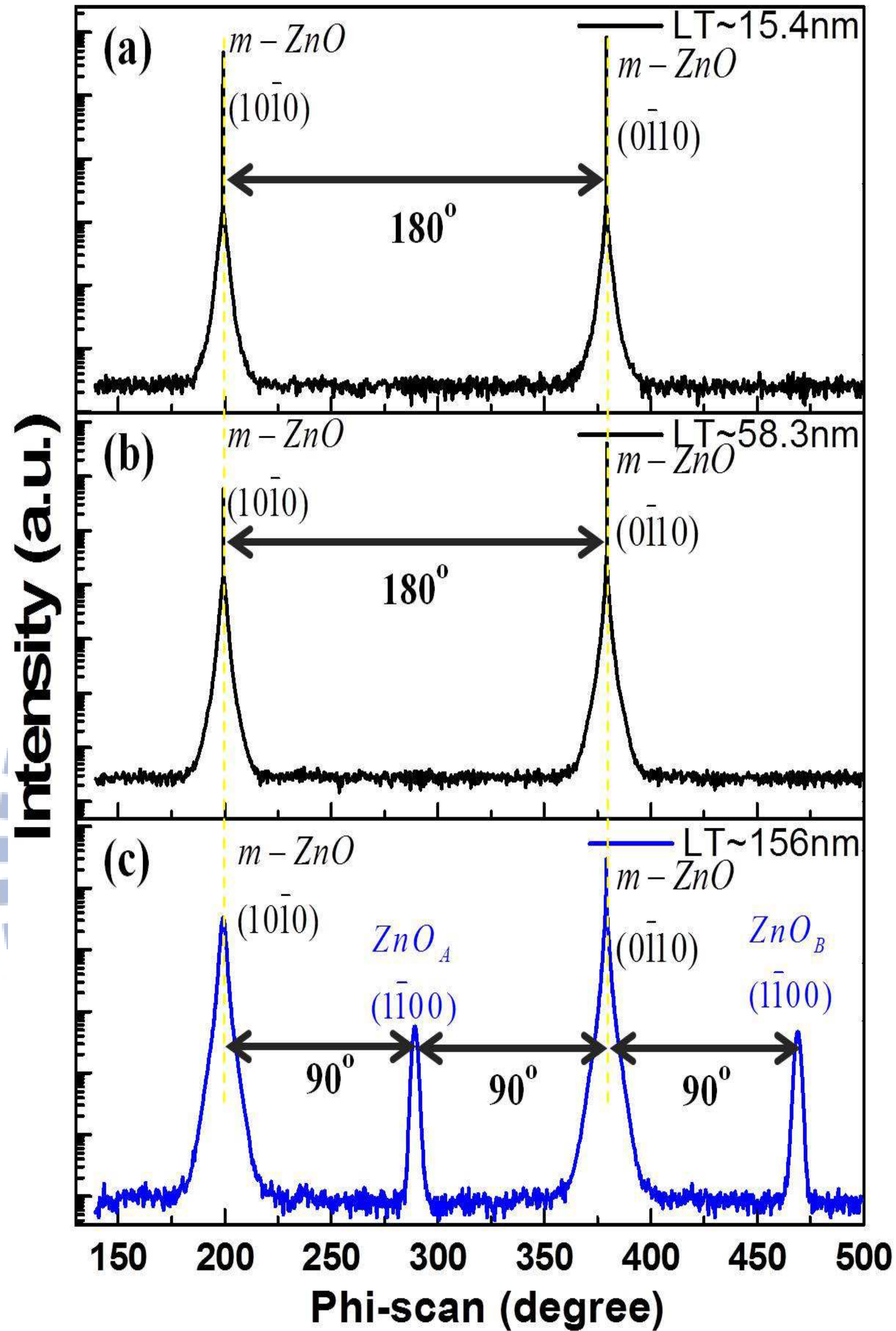

Fig. 6-2 Azimuthal scans of LT-ZnO with various thicknesses. (a) 15.4 nm, (b) 58.3 nm, and (c) 156 nm. The yellow dashed lines indicate the sapphire $\{0006\}$ as references.

In order to further confirm the above-mentioned results, we measured in-plane scan

on $ZnO(0002)$ with various depths that due to the epitaxial relationship between m-ZnO and extra domains showing $(1\bar{1}00)[0002]_{ZnO} \parallel (1\bar{1}03)[1\bar{1}0\bar{1}]_{ZnO}$. Figure 6-3(a) shows the reciprocal-space L-scan with various H, the scan is along $ZnO(0002)$. The value of L closed to 2.005 and 2.08 are attributed to the (0002) plane of LT m-ZnO and the $(1\bar{1}0\bar{1})$ plane of extra domain, respectively. Decrease in the H value indicates the shallower X-ray probed depth or near the surface of LT-ZnO; on the other hand, the larger H value presents the deeper probed depth or even close to the interface of LT-ZnO and m-sapphire substrate. We found the intensity of $ZnO(0002)$ is stronger than that of $ZnO(1\bar{1}0\bar{1})$ from extra domain for the deeper probing depths closed to the interface of LT-ZnO and m-sapphire substrate with H = 0.0135 and 0.0075; and the intensity of the extra domain peak comes close to the in-plane peak of m-ZnO for the shallowest one with H = 0.0005. It shows that the extra domains generation at a particular thickness with H = 0.0015. The result is consistent with Figs. 6-1 and 6-2, which show extra domains become promising when thickness of LT-m-ZnO is over 67 nm.

We determined from XRD peak positions associated with three mutually orthogonal planes, $(11\bar{2}0)$, $(1\bar{1}00)$, and (0002), of the LT-ZnO epilayer and defined the m-$[1\bar{1}00]$, a-$[11\bar{2}0]$, and c-[0001] axes of the wurtzite ZnO lattice as the three orthogonal axes x, y and z of the orthorhombic lattice, respectively. The results manifest that the LT-ZnO buffer is under a tensile strain along the growth direction, i.e., x-axis; laterally the lattice is small strained along the nonpolar y-axis and compressively stressed along the polar z-axis. The small strain along the y-axis results from domain matching the lattice parameter of a (3.2495 Å) of ZnO to c

(12.991 Å) of sapphire by almost factor 4 [**15, 16**] that leads to the lattice mismatch less than 0.08%. Figure 6-3(b) is the strain along mutually orthogonal directions, *x*- and *z*-axes; their strains are larger than 0.53% and -0.59% respectively. The lateral strain is compressive exceeding -1.04% for the second thin sample of ~ 15.4 nm. It first increases with increasing thickness, but reduces from -1.61% for 67 nm LT-buffer to -1.2% of 156 nm one resulting from the existence of extra domains to relax the strain along *z*-axis. On the other hand, along the *x*-axis it is tensile strained as shown in Fig. 6-3, which shows opposite tendency of the *x*-axis with respect to the *z*-axis. It shows the strain increases with increasing thickness of LT-buffer from 15 to 67 nm and strain relaxation occurs when the buffer thickness is thicker for 156 nm one, which exhibits extra domains. The result is consistent with the conclusion of Chapter 5, in which the extra domains provide strain relaxation along the *c*-axis of *m*-ZnO.

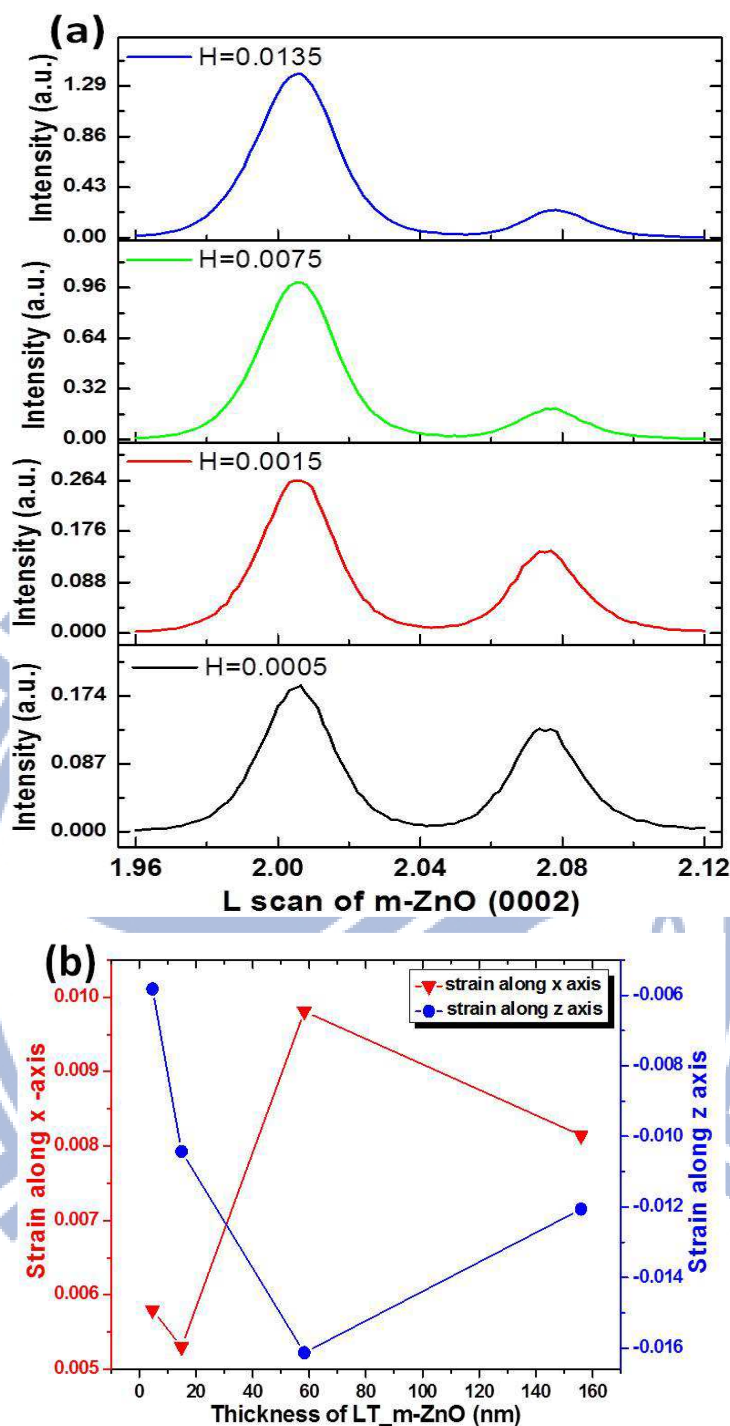

Fig. 6-3 (a) The reciprocal space L-scan on $ZnO(0002)$ with various probed depths label as the H values. The value of L around 2.005 and 2.08 are due to $ZnO(0002)$ of *m*-ZnO and $ZnO(1\bar{1}0\bar{1})$ of extra domain. (b) The strain along the $[1\bar{1}00]$ x-axis and the $[0002]$ z-axis, respectively.

We have shown that the LT grown *m*-plane ZnO buffer can effectively eliminating the extra domains in the two-step growth method, we therefore would proceed to grow *m*-plane ZnO epilayers and multiple quantum wells structures on the optimal LT buffers. However, before doing so, we have to further examine how good the surface morphology of the LT-ZnO buffers are without post thermal treatment. We used the atomic force microscopy (AFM) with tapping mode to measure the surface morphology and compare morphology with different crystalline LT-ZnO. The surface morphologies of LT-ZnO buffer were shown on Figs. 6-4(a)-(e) with ~ 1.7, 4.7, 15.4, 58.3 and 156 nm thicknesses by AFM where each image is $5\times5\,\mu m^2$. The calculated root mean square (RMS) roughness are 0.302, 0.239, 0.203, 0.171 and 6.04 nm, respectively when the thickness of LT-ZnO is increased from 1.7 to 156 nm. The upper and lower images of Fig. 6-4(f) show the fluctuation of surface roughness of LT-buffers having thickness below and above 67 nm. It reveals that the smaller fluctuation of surface roughness for the thin film of thickness < 67 nm due to no extra domains than the thick buffer of 156 nm one, which exhibits strong $\left(1\bar{1}03\right)$-domain XRD. Usually the epitaxial growth develops from the 2D growth to the 3D-island growth [**17, 18**] or called the Stransky-Krastanov (SK) growth mode: Initially, the adsorbates of deposition films grow in layer-by-layer fashion on the crystal substrate; when beyond a critical thickness, which depends on strain and the chemical potential between layer and substrate, the growth continues through the nucleation and island. The wetting layer initially grows layer-by-layer on the mismatched substrate with building up strain; as the wetting layer thickens, the associated strain energy increases rapidly. Once the thickness exceeds the critical thickness, in order to relieve the strain the epitaxial layer relaxes by changing to a 3D growth mode that leads to the formation of defect free islands. Although we are not so sure what thickness is

critical from AFM measurement, we find the LT-buffer without extra domains for those thicknesses below 67 nm, which may be close to 2D growth with small RMS surface roughness. The slight decrease in RMS roughness may be attributed to the lower step morphology generated with increasing thickness from 1.7 to 58.3 nm. The roughness of each step is very similar, but the more steps in thinner film introduce the larger RMS roughness. The thick buffer of ~ 156 nm presents a 3D growth, which possesses dominant extra domains with the larger RMS surface roughness. The different growth rates in 3D growth mode for various orientations make the surface rough for the thick (> 156 nm) film that is consistent with XRD results.

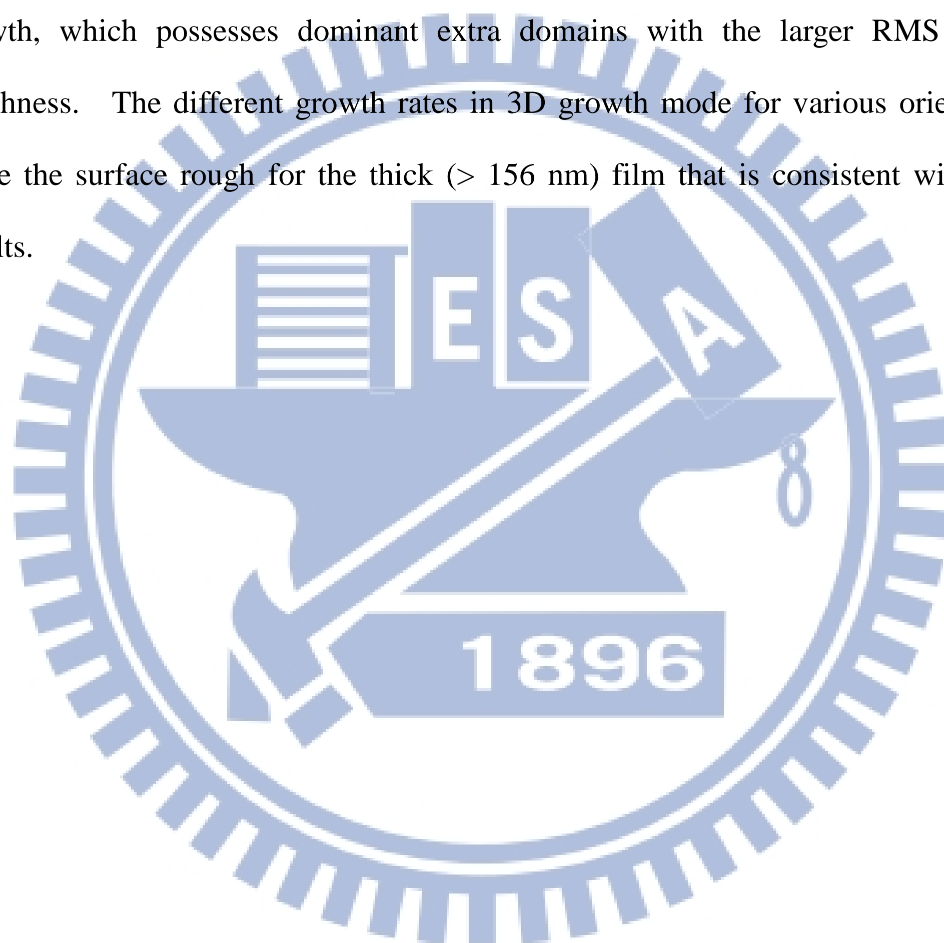

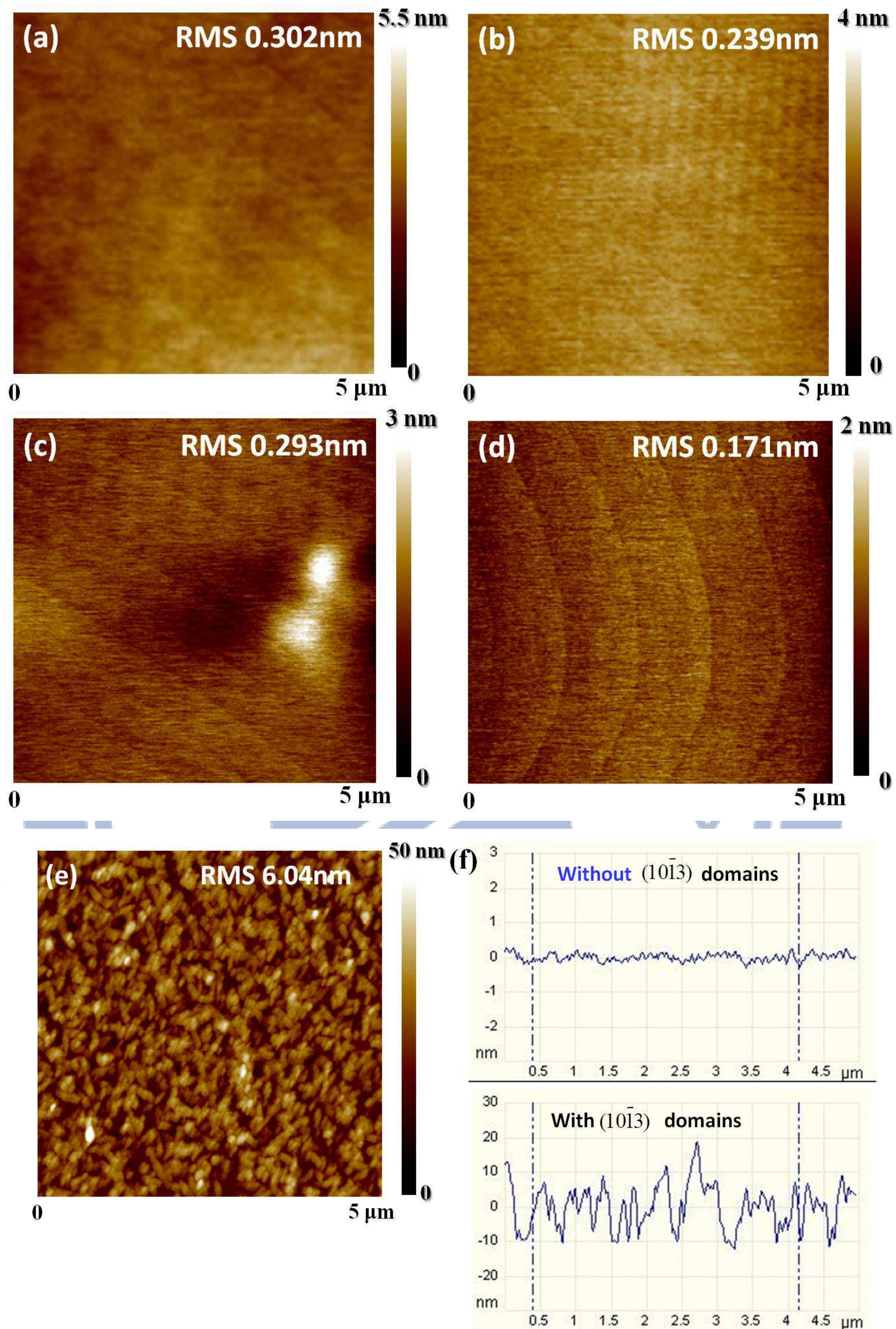

Fig. 6-4 AFM images of LT-ZnO with various thicknesses. (a) 1.7 nm, (b) 4.7 nm, (c) 15.4 nm, (d) 58.3 nm, and (e) 156 nm, respectively. (f) The cross-section profiles of AFM, the upper panel is for the thickness below 67 nm and the lower panel is from the AFM image of (e).

6.2.2 The *m*-ZnO epi-films on LT-buffer

We investigated here the epitaxial growth of *m*-ZnO on LT-buffer at 600℃ or called the high temperature (HT) *m*-ZnO films. The LT-ZnO buffer is the optimal thickness one with thickness < 67 nm. In order to prevent from confusion of the detection signals from the buffer, we grew HT *m*-ZnO over 300 nm. Figure 6-5 is the XRD radial and azimuthal scans of two-step HT *m*-ZnO films (red curves) on the LT-buffers of 4.7 and 58.3 nm (black curves), respectively, in Figs. 6-5(a) and (b) for the surface normal. We observed there are ZnO $(1\bar{1}00)$, $(2\bar{2}00)$, $(3\bar{3}00)$ plane reflections and sapphire $(3\bar{3}00)$ plane reflection, and a weaker shoulder close to q=4.254 $Å^{-1}$ either from the extra domains of HT *m*-ZnO films or from the diffraction interference of LT-buffer that needs further confirmation. The azimuthal scan is a powerful method to distinguish the diffraction interference with extra domains due to the shallower probing depth as compared with the radial ones. Figure 6-5(c) and (d) are the phi-scan of two-step HT *m*-ZnO with 4.7 and 58.3 nm buffer respectively, the yellow dashed lines are $Al_2O_3\{0006\}$ as a reference. The outstanding $ZnO(10\bar{1}0)$ and $ZnO(0\bar{1}10)$ reflections separated 180 degree apart show the epitaxial relationship as those in Chapter 5. However, two weak peaks of $ZnO(1\bar{1}00)$ reflections from extra domains were observable in the HT *m*-ZnO film grown on thin LT-buffers of < 47 nm.

As described in the previous section, the strain in LT-buffer increases with increasing thickness until reaching the critical thickness of ~ 47 nm. The more strain in the LT-buffer distributes the more strain in HT *m*-ZnO film. Therefore, the samples with the thicker LT-buffers possess the larger strain either tensile or compressive. With thick enough LT-buffer from 47 to 67 nm the strain has

significantly reduced but with not observable extra domains, the HT growth *m*-ZnO films on these LT-buffers have the better crystal quality. There is few extra domains observed for HT growth *m*-ZnO on thinner LT-buffers having thickness from 1.7 to 47 nm; we estimate the content of extra domains in *m*-ZnO by XRD intensity ratios of $(1\bar{1}03)_{extra}/(1\bar{1}00)_{ZnO}$ and $(1\bar{1}00)_{extra}/(10\bar{1}0)_{ZnO}$, corresponding to the surface- and off-normal ratios, to be 3.6×10^{-5} and 1.7×10^{-5}, respectively. These values are smaller than that of *m*-ZnO directly grown on *m*-sapphire at 600℃ without LT-buffers which are around 3×10^{-4} and 9.8×10^{-4}. In addition, by increasing the LT-buffer thickness the XRD intensity ratios of $(1\bar{1}03)_{extra}/(1\bar{1}00)_{ZnO}$ and $(1\bar{1}00)_{extra}/(10\bar{1}0)_{ZnO}$ decrease further whose values are one order of magnitude less than that without LT-buffers at the same growth conditions. Summarize from the XRD results, we find that although the two-step growth *m*-ZnO on LT-buffers of < 47 nm have effectively reduced the strain and extra domains to less one order than without the LT-buffers, the optimal thicknesses for LT-buffers should be from 47 to 67 nm in which extra domains in *m*-ZnO can be eliminated.

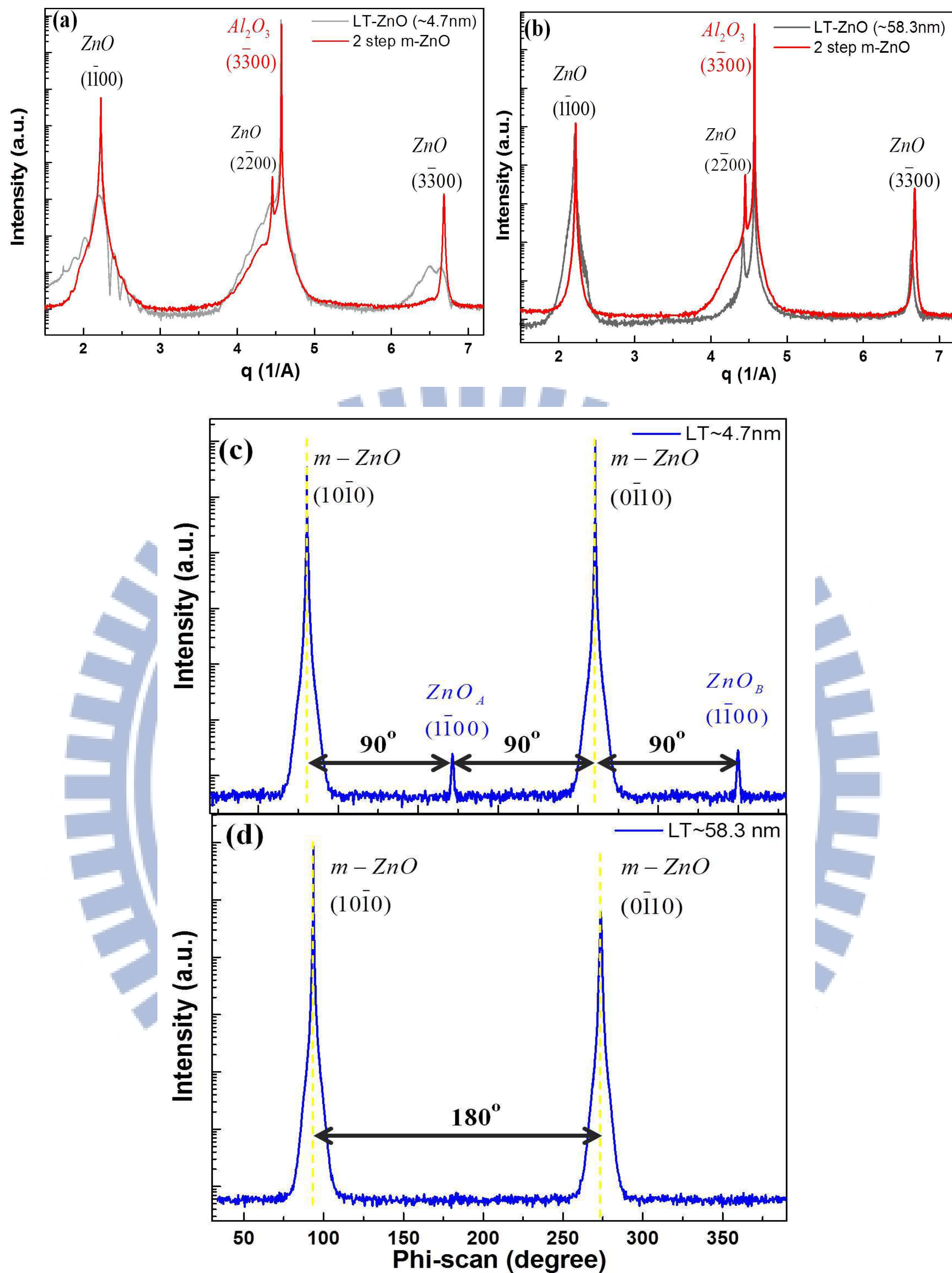

Fig. 6-5 The XRD radial and azimuthal scans of two-step growth *m*-ZnO on *m*-sapphire with LT-buffers of 4.7 and 58.3 nm thick. (a) and (b) are the surface radial scans (black curves for the LT-buffers and red curves for the HT *m*-ZnO). (c) and (d) are the azimuthal scans. The yellow dashed lines indicate the sapphire {0006} reflections.

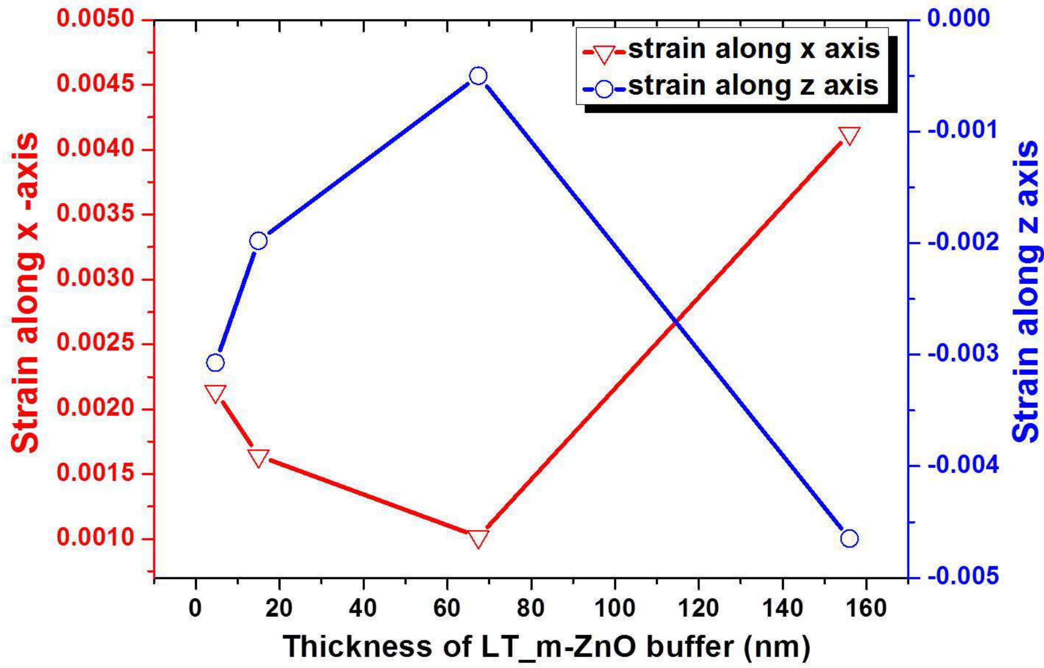

Fig. 6-6 The strains along the $[1\bar{1}00]$ *x*-axis and the $[0002]$ *z*-axis, respectively.

To confirm that the thicker LT-buffer could sustain the more lattice mismatch to release the strains in the HT *m*-ZnO, we calculated the strains of two-step HT *m*-ZnO along *x*-, *y*- and *z*-axes from XRD measurements. The *y*-axis strain along $[1\bar{1}20]$ direction is less than 6×10^{-4}, which is too small to be considered due to almost domain matching with sapphire *c*-axis (12.991Å). The strain of others axes, *x*- and *z*-axes are still tensile and compressive along $[1\bar{1}00]$ and $[0002]$ shown in Figs. 6-6. The HT *m*-ZnO epilayers show smaller strains than LT-buffer. The tendency of strains for the HT *m*-ZnO opposites to the LT-buffer that the strains of HT ZnO layers gradually decrease with increasing thickness of LT-buffer; while increase in strains for the LT-buffer. The strains for the HT *m*-ZnO films on the LT-buffers having thickness below 67 nm are less than 2.2×10^{-3} and -3.2×10^{-3} along *x*- and *z*-axes, respectively. The HT *m*-ZnO still experiences residual lattice mismatch for thinner LT-buffers (< 47 nm), which have no extra domains, whereas, the optimal

thicknesses of the LT-buffers in the range of 47-67 nm provide strain relaxation for growing high quality *m*-plane ZnO although they possess limited extra domains. The result is consistent with the extra domain ratio decrease with increasing LT-buffer thickness. On the other hand, in the thickest LT-buffer with 156 nm thick, the HT *m*-ZnO shows a lot of extra domains ($(1\bar{1}03)_{extra} / (1\bar{1}00)_{ZnO} \sim 5\times10^{-3}$) that is similar to the direct growth *m*-ZnO film on *m*-Al_2O_3 without the LT-buffer. We conclude that using the LT-buffer should be efficient to reduce the strain and to eliminate the extra domains.

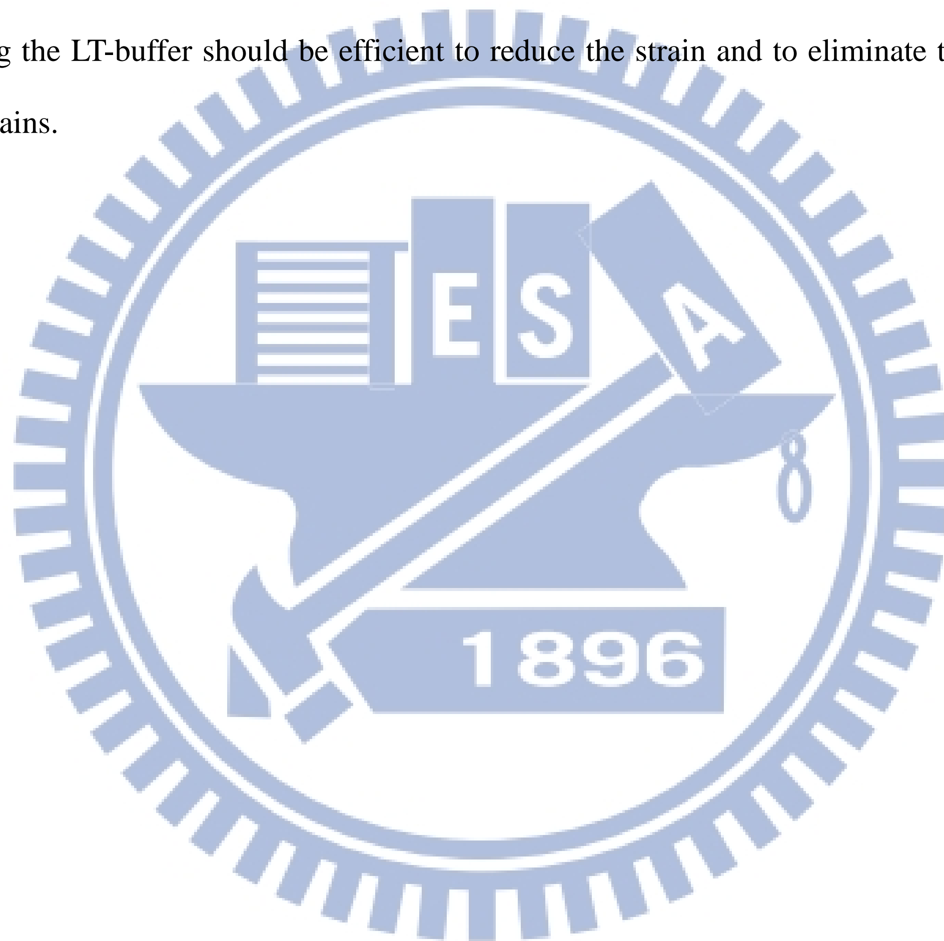

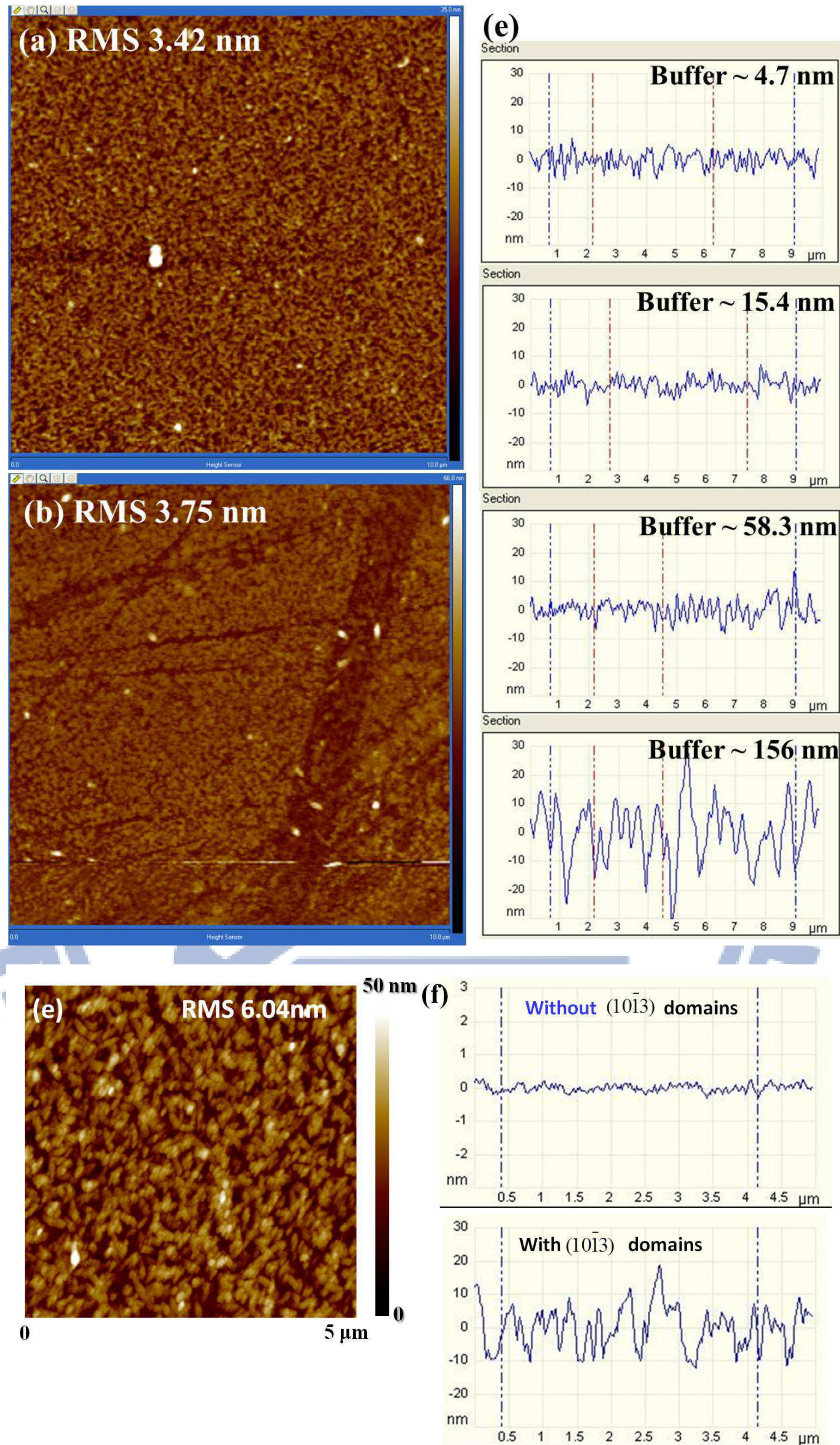

Fig. 6-7 The AFM images of two-step *m*-ZnO epilayers with various thicknesses of LT-buffers, (a) 4.7 nm, (b) 58.3 nm, and (c) 156 nm. (e) The cross-section profiles of AFM images of (a)-(d). (f) The 3-D image of the *m*-ZnO/*m*-sapphire without LT-buffer.

From the AFM images of LT-ZnO buffers in Fig. 6-7, we found smooth surface of HT *m*-ZnO films grown on the LT-buffers with thicknesses ranging from 1.7 to 67 nm; whereas the sample on the thickest LT-buffer of 156 nm shows rough surface that may be contributed from the extra domains. Figures 6-7(a), (b) and (c) are the AFM images of the two-step *m*-ZnO samples grown on 4.7, 58.3 and 156 nm LT-buffers. Their surface profiles are shown in Figs. 6.7(d), which reveal the RMS surface roughness are 3.42, 3.75, and 19.75 nm, respectively. Consistent with the previous discussion that the surface roughness is small for the samples with thickness of LT-buffers less than 67 nm, but it increases dramatically for the thickest buffer sample, whose roughness is comparable to the direct growth sample without buffer (17.5 nm) shown in Fig. 6.7(e). The large surface roughness should be attributed to the existence of extra domains.

6.2.3 Defect states in the two-step grown *m*-ZnO films

We also took cross-sectional TEM images of two-step growth *m*-ZnO with ~ 4.7 nm LT-buffer under various geometries. A selected area electron diffraction (SAED) pattern of the squared region near the *m*-ZnO/sapphire interface taken along the ZnO $[11\bar{2}0]$ zone axis is shown in Fig. 6-8(a) to reconfirm the epitaxial relationship determined by XRD. High-resolution TEM images of the *m*-ZnO/sapphire interface were also taken along two orthogonal zone-axes, $[11\bar{2}0]_{ZnO}$ and $[0002]_{ZnO}$, to examine the structure defects of the samples. Shown in Fig. 6-8(b) is the micrograph recorded along the $[0002]_{ZnO}$ zone axis with $\vec{g}=[11\bar{2}0]_{ZnO}$. It reveals the highly perfect atomic arrangement of the ZnO layer. The inset shows the Fourier filtered image of the interface region. The nearly periodically arranged misfit dislocations, noted by extra half-planes inserted in the ZnO film, illustrate the domain matching

epitaxial (DME) growth with four $(11\bar{2}0)_{ZnO}$ planes matching with three $(0006)_{sapphire}$ planes along the $[11\bar{2}0]_{ZnO}$ direction. The DME growth has significantly reduced the lattice mismatch induced strain along this direction. There are a few illegibility *m*-ZnO layers within 2 nm to the interface that should be attributed to lack of kinetic energy for atom rearrangement at LT growth. The thermal annealing at high temperature after the two-step growth should make improvement to the samples.

Notably, the TEM image reveals several contrast lines that propagate along the growth direction (marked by arrows). These lines are likely due to basal plane stacking faults (BSFs). We further characterize the nature of the contrast lines by performing diffraction contrast analysis on the annealed sample. The contrast lines are clearly visible in the dark field image recorded with diffraction vector $\vec{g} = [1\bar{1}00]_{ZnO}$ along the $[0002]_{ZnO}$ zone axis, shown as Fig. 6-8(c). Many BSFs initiated from the ZnO/sapphire interface were identified. We found the BSFs belong to intrinsic Frankel–Shockley partial dislocations (type-I_1) with a Burgers vector $\vec{b} = \frac{1}{6}\left[2\bar{2}03\right]$. The results of TEM are similar to the *m*-ZnO/*m*-sapphire in Chapter 5.

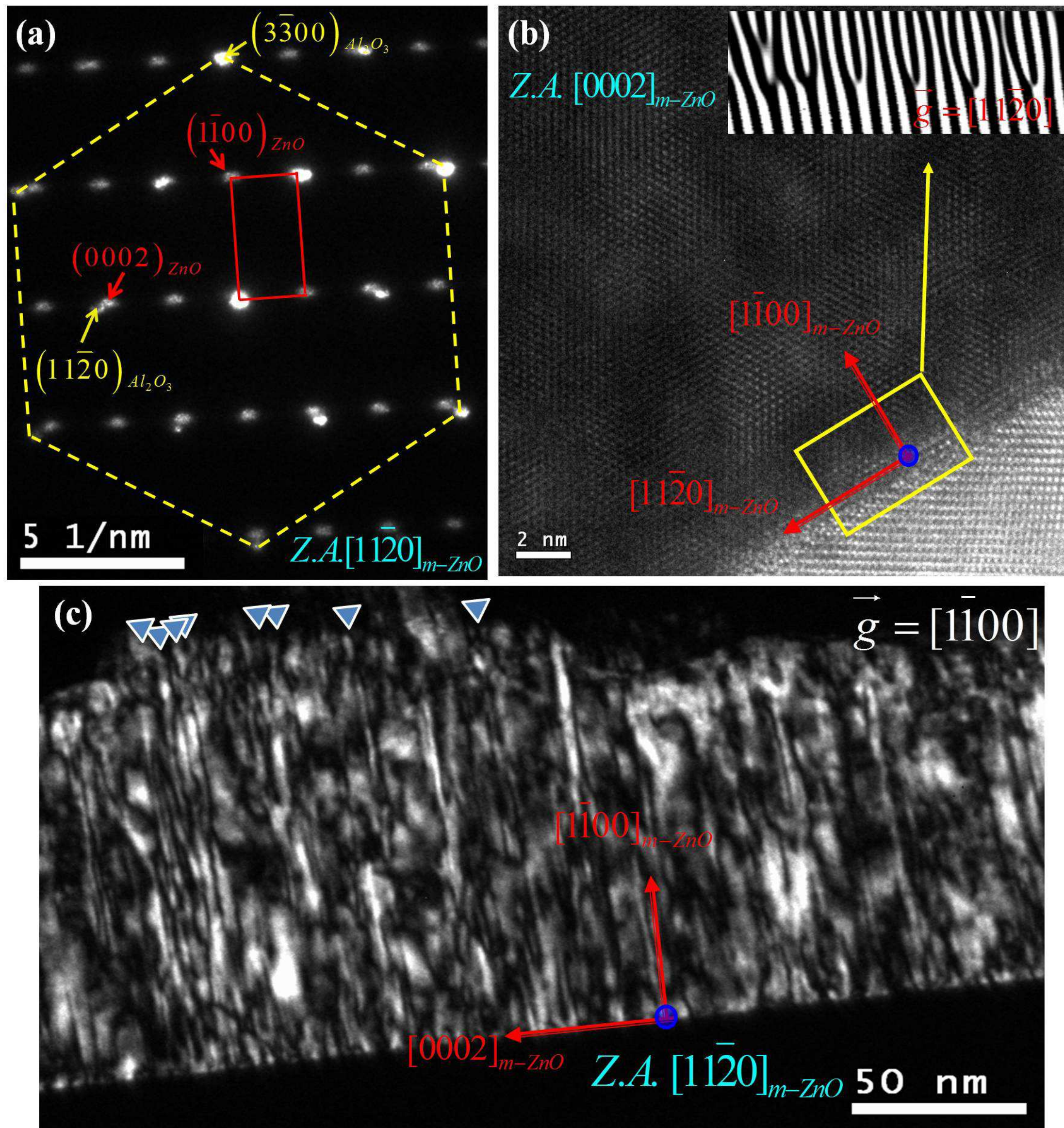

Fig. 6-8 (a) The selected area electron diffraction (SAED) of TEM along $[11\bar{2}0]_{ZnO}$ zone-axis, (b) high resolution TEM TEM images of the *m*-ZnO/sapphire interface along $[0002]_{ZnO}$ zone-axis, and (c) The TEM dark field image along $[11\bar{2}0]_{ZnO}$ zone-axis with $\vec{g} = [1\bar{1}00]_{ZnO}$. The inset in (b) is inverse Fourier transform image from interface with $\vec{g} = [11\bar{2}0]_{ZnO}$.

These TEM images reveal that BSF is the dominant structural defect in the

two-step growth *m*-ZnO. Its density is estimated to be about 2×10^{6} cm^{-1}, which is about four times more than *m*-ZnO without LT-buffer of $\sim5\times10^{5}$ cm^{-1}. The BSFs density of two step growth *m*-ZnO is quite close to the high quality *m*-plane ZnO films grown on $LaAlO_3$ and sapphire substrate at high and low growth temperatures by PLD and atomic layer deposition [**19, 20**]. The higher BSFs density should be one way to relax lattice mismatch that should in turn affect on optical properties of growth samples.

6.3 Optical properties of two-step growth *m*-ZnO

6.3.1 PL spectra

According to the structure properties of two-step growth *m*-ZnO samples, there are lower extra domains and higher BSFs density than that without LT-buffers. The ultimate goal of two-step growth is to eliminate extra domains to reduce domain boundary trapping excitons emitted around 3.17 eV. We compare the normalized PL spectra of two-step growth samples with those direct growth *m*-ZnO samples in Chapter 5 in Fig. 6-9 excited by 325 nm HeCd laser at 13K. The red and black dashed lines are *m*-ZnO with 4.7 nm LT-buffer and without buffer, respectively. It reveals that absence of broad-band 3.17 eV emission resulting from the domain boundary trapping between the *m*-ZnO and extra domains for LT-buffered *m*-ZnO films. There are three peaks from PL spectrum of two-step growth at about 3.364, 3.321 and 3.264 eV. Teke et al. [**21**] had identified the optical transitions of ZnO bulk that the spectral ranges of 3.3598-3.3664, 3.32-3.34 and 3.218-3.223 eV are attributed to the donor-bound excitons, two-electron satellite (TES), and donor-acceptor-pair (DAP) transitions, respectively. These transition energies of donor-bound excitons and TES are dependent on the bound energy of the localized

energy of donors. No emission peaks in the visible range observed suggest no deep-level emission from oxygen vacancies and zinc interstitials [**22**].

The peak energy of DAP follows $E_{DAP} \cong E_g - E_A - E_D$, where E_g, E_A and E_D are band-gap energy, binding energies of acceptor and donor, respectively. If the thermal energy can provide large enough energy for electrons to escape from the donor trapping potential, the higher transition called the free-electron bound to acceptor (e,A) with transition energy $E_{(e,\ A)} \cong E_g - E_A$ may occurs. In addition, many groups have reported strong BSF emissions in LT-PL spectra of nonpolar GaN layers [**23-26**]. In addition, Yang and Schirra *et al.* [**20, 27**] reported the stacking fault related 3.32 and 3.31 eV luminescence in *m*- and *a*-plane ZnO. Our samples with high BSFs density of 2×10^6 cm^{-1} should provide strong enough BSFs emission. We can distinguish these three intense lines from the PL spectra of two-step growth *m*-ZnO at about 3.364, 3.321 and 3.264 eV related to D_0X, X and Y bands, respectively, in which the X and Y bands could be either TES or BSFs and (e,A) emissions. In order to clearly identify the X and Y bands, we measured the peak position of Y band (blue circles) and intensity ratio of X band over D_0X (black stars) with various pumping powers in Fig. 6-10(a). The Y band is blue-shifted with increasing pumping power; that indicates the typical behavior of (e, A) emission. Though at lower pumping power the donor can bound the free electrons, with higher pumping power to increase the thermal energy due to heating frees the electrons so that the Y band is blue shifted. The shift energy corresponds to the binding energy of 14.5 meV, which is close to the energy of difference between $FX_{A,B}$ and D_0X (~ 15.2 meV). The values of black stars (intensity ratios of X-band/D_0X) in Fig. 6-10(a) are often over 1 with various pumping powers, and in Fig. 6-10(b) the binding energy ratios of D_0X/TES show scattered data. It implies the X band should not contribute

from the TES, which is the excited state of D_0X. According to the Haynes rule, the binding or localization energy of the D^0X is proportional to the binding energy of the corresponding donor, $E_{loc} = \alpha E_B$, where E_{loc}, E_B, and α are the localized energy of D_0X, donor binding energy of TES, and Haynes' proportionality constant close to 0.33 or 0.34 [**21**]. The TES transition should follow the above rule. We plotted all localization energy with binding energies of the corresponding donor of two-step samples in Fig. 6-10(b), and the red line is Haynes' proportionality constant close to 1/3, all of X band with different thicknesses of LT-buffers do not follow the Haynes rule, therefore we exclude the possible of TES transition.

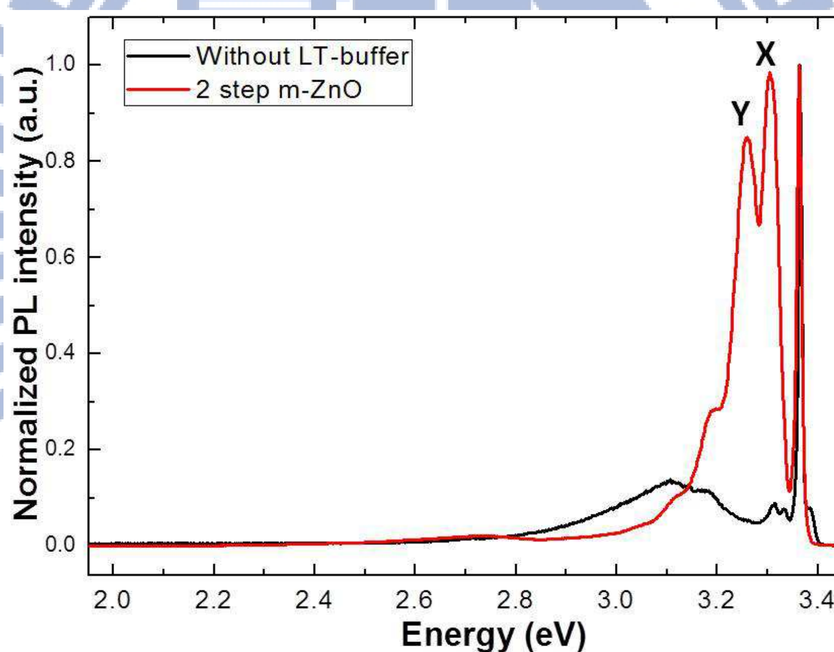

Fig. 6-9 The PL spectra of two-step growth m-ZnO and direct growth shown red and black lines at 13K. The peaks at about 3.321 and 3.264 eV are labeled with the X and Y bands.

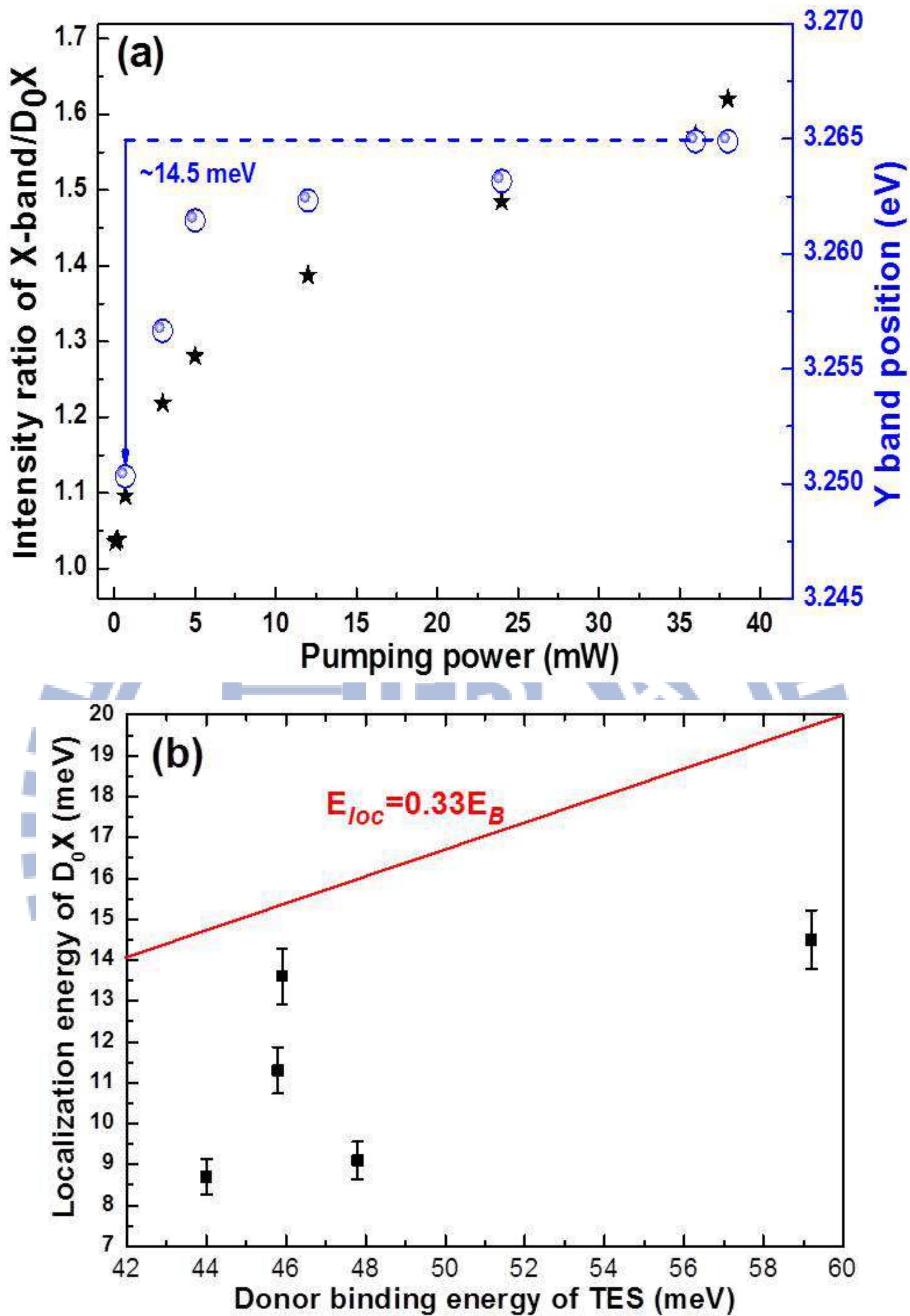

Fig. 6-10 The dependences of Y band position (blue circles) and intensity ratio (black stars) of X-band/D_0X on the pumping power (a) and the TES binding energy versus the donor binding energy (b). The red line is ideal Haynes rule and black points are the donor binding energy proportional to exciton binding energy of two-step samples with various thicknesses of LT-buffers.

All the PL spectra of two-step growth m-ZnO samples show only three dominant D_0X, X band, and (e,A) peaks as in Fig. 6-9, even if some of them have their LT-buffers contain extra domains. The absence of the SX emission is also similar to the annealed direct growth samples in Chapter 5, in which thermal annealing has dramatically reduced the content of extra domains to $\sim 10^{-5}$. Our two-step growth m-ZnO layers have the content of extra domains below 3.6×10^{-5}, therefore, we did not observe SX emission, but there is a weak TES transition in PL spectra of two-step m-ZnO layers with no extra domains. Figures 6-11(a) and (b) exhibit the temperature dependent PL spectra in log-scale of two-step m-ZnO with 58.3nm thick LT-buffer and the corresponding temperature dependent peak positions of all the emission peaks. We found three major peaks at 3.364, 3.309 and 3.263 eV and two shoulders at 3.378 and 3.328 eV are attributed to D_0X, X band, (e, A), A- and B-free excitons ($FX_{A.B}$), and TES emission, respectively. The dashed lines positioned in Fig. 6-10(a) labeled by LO-(e, A) phonon replica, ~72 meV apart from the (e, A) peak, are the LO-phonon replica of the (e, A) peak. The $FX_{A.B}$ data were fit by the Bose-Einstein expression: $E(T) = E(0) - \sum_{i=1}^{6} a_i / [\exp(E_i / kT) - 1]$, where $E(0)$ represents the emission energy of free exciton A, B at T = 0 K, E_i are the optical phonon energy with a_i being the strength of the corresponding exciton-phonon interaction [**28**]. The six optical phonon energies correspond to the Raman modes in bulk, which are 101, 380, 410, 437.5, 576 and 587 cm^{-1} [**29**]. However, the A_1(LO) and E_1(LO) modes (~ 576 and 587 cm^{-1}) have energy separation around 1 meV; it is too close to distinguish, therefore we combine them to a single LO-phonon mode at ~ 72.1 meV with the coupling strength a_5^*. After the fitting (black curve), we obtained the coupling coefficients a_1 and a_5^* to be 0.0214 and 0.5018 and the other

coupling coefficients are less than 10^{-12} which can be neglected. Furthermore, we found except for the X band, which shows temperature dependent "S" shape peak positions, those temperature dependent emission peaks can be well fit by the same coupling coefficients a_1 = 0.0214 and a_5^* = 0.5018. The respective energy differences to the $FX_{A,B}$ are about 11.8, 34.5 and 113 eV, respectively, for D_0X and TES, and (e, A), which are attributed to the localized energy of donor, donor binding energy of TES, and the localized energy of acceptor. In addition the peak labeled as TES has the Haynes' proportionality constant 0.342, similar to the inset of Fig. 4 in Ref. 21.

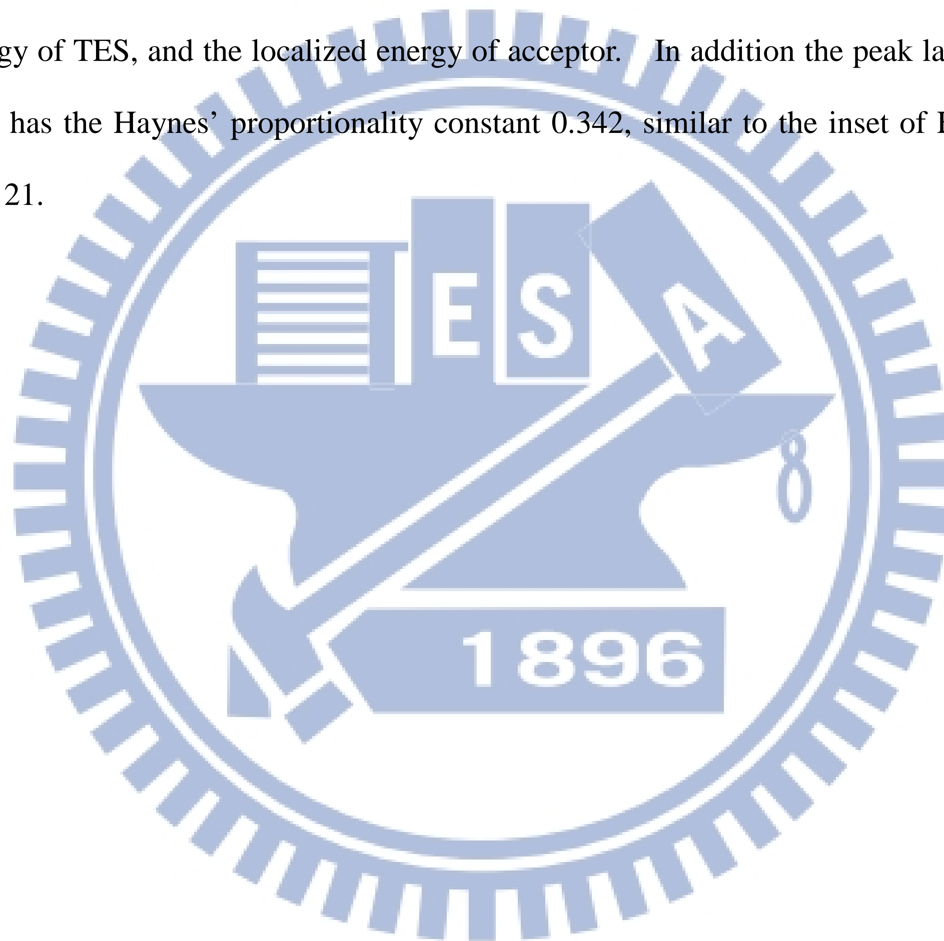

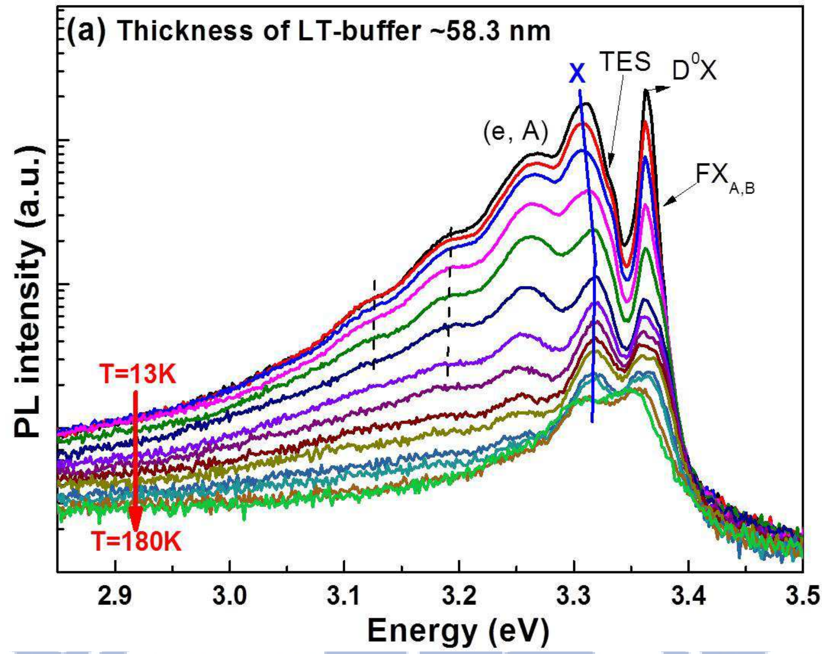

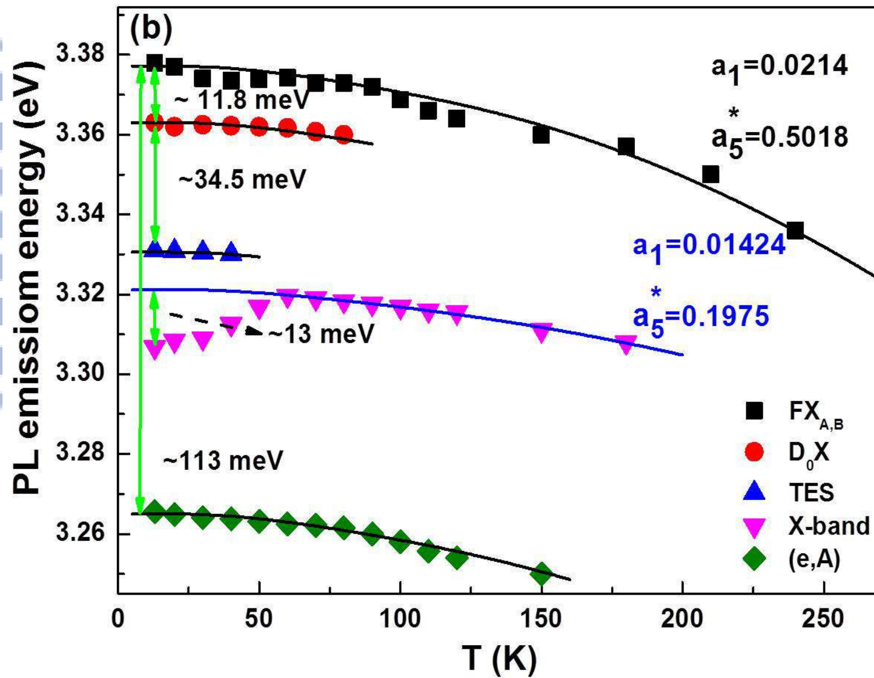

Fig. 6-11 The temperature dependent PL spectra (a) and (b) peaks position of $FX_{A,B}$, D_0X, TES, X-band and (e, A) of two-step m-ZnO with ~58.3 nm buffer which possesses no extra domains. The dashed lines in (a) are the phonon replica of (e, A). The temperature dependent peaks position of $FX_{A,B}$, D_0X, TES, X-band and (e, A) are labeled with black, red, blue, pink and green points, respectively in (b). The solid curves are the fittings to the Bose-Einstein equation.

The X band shows the S-shape red shift with respect to the fitting Bose-Einstein equation for temperature lower than 60K, which corresponds to the localized energy closed to 13 meV in Fig. 6-11(b). The fitting coupling strengths are a_1 = 0.01424 and a_5^* = 0.1917, which are smaller than the other emission peaks indicating the lower phonon coupling for the X band transition. The two-step growth *m*-ZnO layers not only possess the lower extra domains but also the higher BSFs density as compared with the direct growth *m*-ZnO. The lower extra domains and higher BSFs are the main reasons for causing X band emission but without the SX emission. It has been reported that the emissions at ~ 3.31 eV may come from the BSFs in nonpolar ZnO, [**20, 27, 30**] and Stampfl, *et al.* [**31**] reported the BSFs belonging to the type-I_1 stacking faults is a zinc-blende regions, which can trap the electrons. Sun, *et al.* [**32**] reported BSFs do not introduce localized state in the band gap, but they form quantum-well-like structures since they can be regarded as thin zinc-blende layers embedded in the wurtzite matrix. The transition energy of BSFs was reported sensitive to the potential fluctuations with localization energy closed to 18 meV that leads to the S-shape temperature dependent transition energy. The behaviors of X band emission are quite satisfied with the BSFs emission, BSFs structures are considered to be thin zinc-blende layers embedded in the wurtzite matrix which is the quantum-like structure. We have recently showed that the S-shaped due to the fluctuations of the distances of the coupled BSF wells, and their localized energy depend on the average BSFs density. [**20**] The smaller phonon coupling coefficients may be attributed to the quantum-like structure that reduces the LO-phonon coupling as a result of quantum confinement effect. [**33, 34**] We therefore conclude that the PL spectra of two-step growth *m*-ZnO are dominated by D_0X, BSFs and (e, A) emissions, the *m*-ZnO on optimal thickness of LT-buffer show weak TES emission

around 3.312 eV with eliminated SX emission due to lower extra domains content than those of direct grown *m*-ZnO layers without LT-buffers.

6.3.2 Raman spectra

The anisotropic strains in *m*-ZnO on *m*-sapphire substrates are smaller than *a*-ZnO whose crystal symmetry is broken on the *r*-sapphire substrates identified by XRD measurements. The Raman tensors for the wurtzite ZnO, which depend on specific crystal orientation such as A_1(LO) and A_1(TO) modes have the same form of lattice vibration but propagation parallel and perpendicular to *c*-axis of ZnO, should follow particular selection rules, which are useful to analyze the *m*-ZnO with different grown orientations. We used typical micro-Raman measurement by using a 100X objective lens to focus 532 nm excitation laser beam on the sample surface normally. Figure 6-12 shows the polarization dependent Raman spectra of the direct growth *m*-ZnO samples at various temperatures as indicated in which Φ is the angle between the electric field of incident excitation light and the c-axis of ZnO. The Raman peaks marked with blue circles at 378, 416, 429, 449, 574 and 642 cm^{-1} result from *m*-sapphire wafer. The characteristic peaks of ZnO are marked by black dashed and red solid lines located around 443 and 580 cm^{-1}, respectively. The reported phonon energies of E_2^{high}, A_1(LO) and E_1(LO) from bulk ZnO are 437.5, 576 and 587 cm^{-1} [**29**].

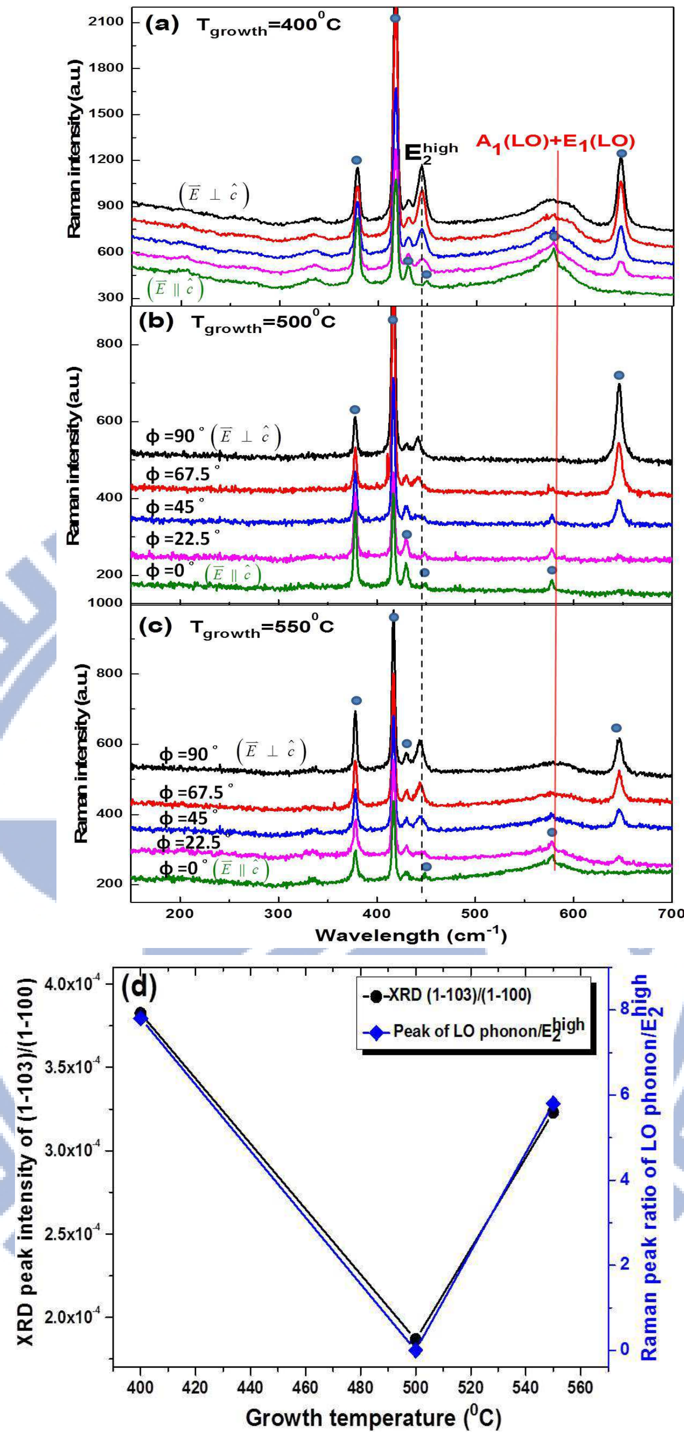

Fig. 6-12 The polarization dependent Raman spectra of the direct growth *m*-ZnO samples on *m*-sapphires without buffer layers grown at various temperatures. (a) 400℃, (b) 500℃, and (c) 550℃, respectively. The blue circles are sapphire modes. Black dashed and red solid lines are E_2^{high} mode at 443.02 cm^{-1} and 580 cm^{-1}. (d) The normalized peak intensity of LO-phonon modes and extra domains contents depend on growth temperature.

From the Raman tensors, $E_2^{high}=(d_{xy},d_{yx})$, $E_1(x)=(c_{xz},d_{zx})$, $E_1(y)=(c_{yz},d_{zy})$ and $A_1(z)=(a_{xx},a_{yy,}b_{zz})$, where the suffix of modes and index in the matrix are phonon propagation and polarization directions, respectively. Here x, y and z are the polarization directions along the ZnO crystallographic m-$[1\bar{1}00]$, y-$[11\bar{2}0]$ and z-[0002] directions. Based on the Raman selection rules for the E_2^{high} modes, one should not observe the E_2^{high} modes when the excited polarization is along the c-axis. Sander *et al.* [**35**] reported the high NA microscope objective should lead to a component of the polarization perpendicular to the sample's surface so that perpendicular to the *c*-axis of *m*-ZnO films. However, this effect is not sensitive in our case. This result is different from that in Fig. 4-6 of Chapter 4, in which ZnO crystal symmetry breaks to become C_{2V} showing weak E_2^{high} in $y(zx)\bar{y}$ as the excited polarization parallel to the c-axis.

Read from Figs. 6-12(a)-(c), we have the phonon frequencies of E_2^{high} are 443.05, 440.6 and 442.4 cm^{-1}, respectively, which are blue shift relative to the bulk value of 437.5 cm^{-1}. The E_2^{high} shift to the high-energy side due to compressive strain along the *z*-axis, tensile strain along *x*-axis, and almost strain free along *y*-axis in these samples determined from XRD. The growth temperature at 500℃ shows the closest to the bulk value due to the lowest compressive strain along *z*-axis. In addition, the peaks marked by red solid line at 580 cm^{-1} (bulk) are attributed to the A_1(LO) and E_1(LO) modes. Many reports have observed the quasimodes at ~ 580 cm^{-1}, which is intermediate to the frequencies of the A_1(LO) and the E_1(LO) modes of bulk value, are mixed symmetry modes due to phonons propagating between the *a*- and the *c*-axes [**36, 37**]. One should not observe the A_1(LO) mode in pure *m*-ZnO under any excitation polarizations as the measured direction is vertical to the phonon

propagation direction; on the other hand, the E_1(LO) mode should often be observable in any excitation polarizations when measured direction cross *c*-axis. The extra domains which rotates against the common y-axis by ~±59° from that of the *m*-ZnO provide the other crystalline orientation, the samples in Figs. 6-12(a)-(c) have the extra domains content around 10^{-4}, the mixing LO-phonon (A_1(LO) + E_1(LO)) mode is enhanced with the extra domains content. Figure 6-12(a) shows strong mixing LO-phonon mode in any Φ values. Nevertheless it is not observable in Fig. 6-12(b), which has the lowest content of extra domains of $\sim 1.8\times10^{-4}$ as presented in Chapter 5.

Figure 6-12(d) shows the extra domains contents and the normalized peak intensity of the mixing LO-phonon versus the growth temperature. The normalized peak intensities of the mixing LO-phonon are calculated by summing over all of the spectra with various Φ then being divided by the intensity of the E_2^{high} peak, which is the characteristic mode of ZnO regardless with the measured directions. It shows that the normalized intensity of mixing LO-phonon mode is highly correlated with the extra domains content in the direct growth *m*-ZnO/*m*-Al_2O_3 samples without LT-buffers. The Raman spectra become distinguishable from different measured orientations as the content of extra domains in *m*-ZnO is larger than 1.8×10^{-4}. So we conclude that the peaks at ~ 441.5 and 580 cm^{-1} attributed to the frequency shifted of E_2^{high} mode and A_1(LO)+ E_1(LO) phonon mode result from the strain effect and the existence of extra domains, respectively; and the Raman spectra are sensitive to extra domains content above 1.8×10^{-4}.

As mentioned previously, the two-step growth *m*-ZnO epilayers have extra domains contents below 3.6×10^{-5}, which is less than 1.8×10^{-4} and is too low to observe the difference in different configurations of Raman measurement. Figure 6-13(a) is the Raman spectra of the two-step growth *m*-ZnO layers with LT-buffer ~

4.7 nm having extra domains content of $\sim 3.4\times10^{-5}$, which is the largest one in these series of two-step growth samples. Similar to Fig. 6-12(a)-(c), the peaks marked with blue circles are the sapphire peaks, but there are no peaks at ~ 580 cm^{-1} in Fig. 6-13(a) due to the relatively low extra domains content, and the phonon frequency of the E_2^{high} mode is at ~ 439.5 cm^{-1}, which is smaller than 440.6 cm^{-1} in Fig. 6-12(b), that due to tensile strain as in Fig. 6.6. Figure 6-13(b) shows the E_2^{high} modes position dependent on the strain along *x*-axis (surface normal) which behavior is opposite to *z*-axis (*c*-axis) in Fig. 6-6. The blue dashed line is the ZnO bulk value of 437.5 cm^{-1}. The Fig. 6-13 show the thicker LT-buffer could reduce strain effective, which E_2^{high} frequencies are ~ 439.5, 438.9 and 438.3 cm^{-1}. The thicker LT-buffer with lower strain effect cause the E_2^{high} frequencies toward bulk value and the too low extra domains contents in *m*-ZnO ($\leq 3.6\times10^{-5}$) made the Raman spectra to observe LO-phonon mode.

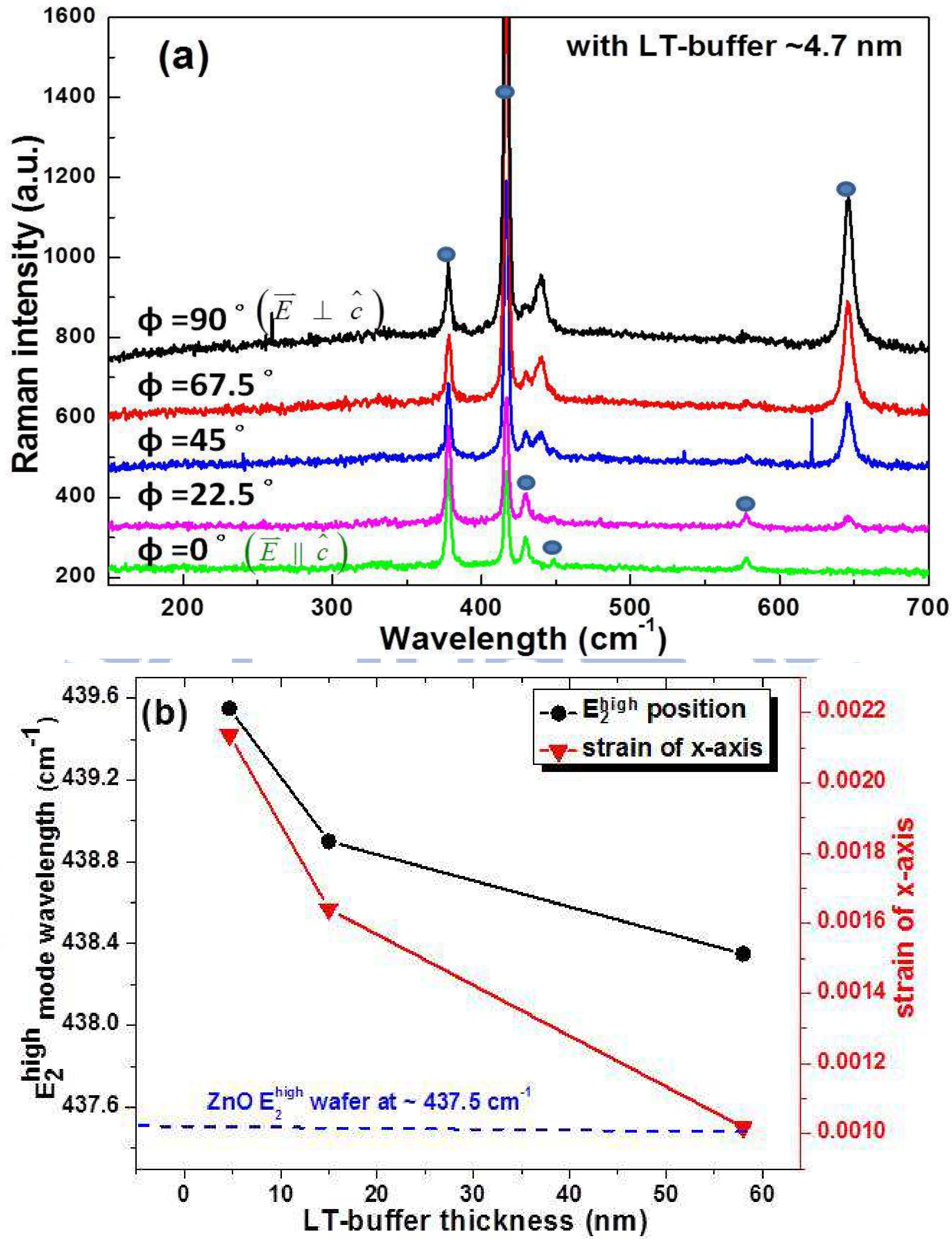

Fig. 6-13 The polarization dependent Raman spectra of two-step growth *m*-ZnO with buffer thickness ~ 4.7 nm (a) and the E_2^{high} mode frequency and strain of *x*-axis versus the thickness of LT-buffers (b). The extra domains content ($(1\bar{1}03)_{ZnO} / (1\bar{1}00)_{ZnO}$) is around $\sim 3.4\times10^{-5}$. The peaks marked by blue circles are the sapphire modes.

6.4 Non-polar quantum well structures on *m*-sapphire

In order to realize whether the nonpolar multiple quantum wells (MQWs)

structures could be made absence of the quantum confinement stork effect (QCSE), we fabricate 5 pairs of *m*-plane ZnO/MgZnO MQWs with three well widths on a *m*-ZnO buffer grown by two-step method including the LT and HT layers with thicknesses of about 5 and 500 nm. The thickness of barriers is fixed to 55 nm and the well widths are 4, 8, and 16 nm, respectively. The LT-PL spectrum of the QWs with well width of 4 nm shows the barrier (MgZnO) emission at 3.599 eV and well, emissions at 3.427 and 3.395 eV in Fig. 6-14(a), respectively. The Mg content calculated according to Koike's equation [**38**] from the PL spectra is close to 8.6%. The dashed line is the near-band edge emission of bulk ZnO at ~ 3.365 eV, on the low-energy side of the dashed line is attributed to the buffer emission. The peaks at 3.428 and 3.395 eV are attributed to the confined-exciton and BSF bound exciton emissions in the QWs, respectively. The energy separations of spectral peaks on the low-energy shoulder marked with solid lines in Fig. 6-14(a) are closed to 72 meV, corresponding to the LO phonon energy in ZnO. From the phonon position, we determine the phonon replica from the BSF bound exciton emissions (3.395 eV) in the QWs.

Figure 6-14(b) show the PL spectra at 13K with various well widths. The emissions of both the confined and the BSF bound excitons in QWs blue shift with decreasing well width resulting from the quantum confinement effect. The results differ from those of the polar ZnO QW structures, which were red shift below the bulk ZnO value due to the QCSE for the well width being wider than 3 nm [**39-43**]. The NBE emission of our sample with well width of 16 nm is closed to the bulk one, but as the samples with well widths decrease below 8 nm, their NBE emissions show blue shift relative to the bulk ZnO. Without the internal electric field building in the nonpolar QWs, the blue shift of band edge with further decreasing well width to 4 nm is more promising. These results confirm that the nonpolar QWs structures should

resolve the QCSE to enhance optical emission efficiency.

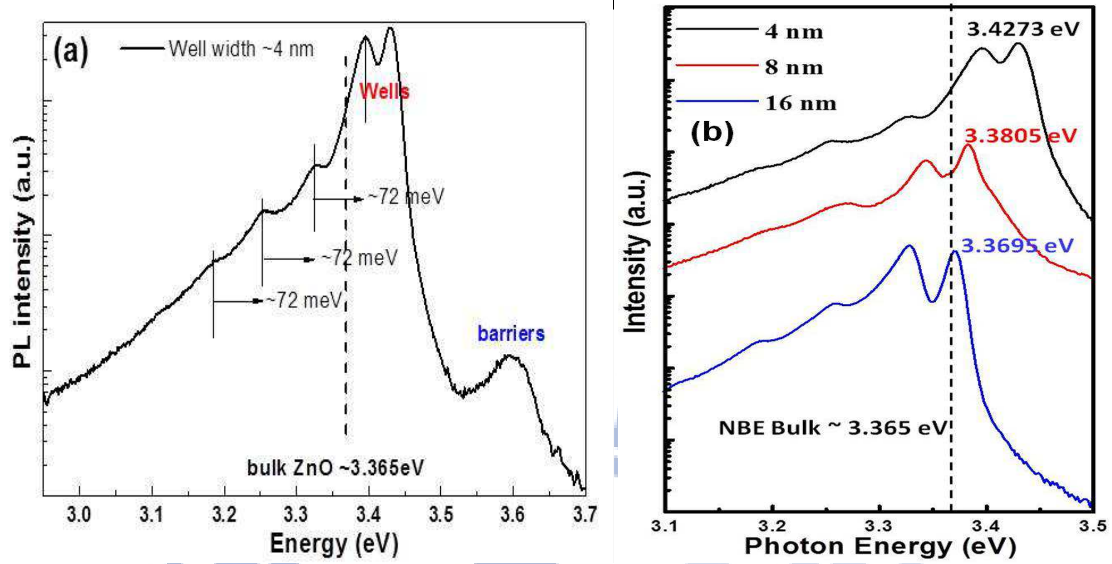

Fig. 6-14 The PL spectra of *m*-plane MQWs with well widths of 4, 8 and 16 nm measured at 13K. (a) The PL spectrum of nonpolar MQWs of 4 nm well width shows the near-band edge (NBE) emissions from barriers, respectively; and (b) The PL spectra of various well widths indicated. The dashed line is the NBE emission of bulk ZnO.

6.5 Summary

We use LT-buffer layers, which show no extra $(1\bar{1}03)_{ZnO}$ domains for successfully growing *m*-ZnO epitaxial films without extra domains on *m*-sapphire. The major crystal structure and defect properties of the two-step *m*-ZnO epilayers are similar to the thermal annealed *m*-ZnO layers in Chapter 5. After having analyzed the XRD measurement, we found absence of extra $(1\bar{1}03)_{ZnO}$ domains for the thickness of LT-buffer layers thinner than 67 nm, but presence of a few extra domains for the thickness going above 156 nm. Further raising the growth temperature to fabricate *m*-ZnO layers on the LT-buffers, we found the optimal thickness of LT-buffer ranging from 47 to 67 nm. For the samples grown with the thinner LT-buffers (< 47

nm), we could find weaker $(1\bar{1}03)_{ZnO}$ domains in the HT *m*-ZnO, whose content is about one order less than those direct growth *m*-ZnO samples without LT-buffers. The extra domains contents decrease with increasing LT-buffer thickness and the largest extra domains content is $\sim 3.6\times10^{-5}$ in *m*-ZnO with the 1.7 nm LT-buffer. Determined from XRD and Raman spectra, we found that the two-step growth *m*-ZnO samples show the lower strain than those without LT-buffers. The Raman spectra of the mixing LO-phonon mode (A_1(LO) + E_1(LO)) appeared at ~ 580 cm^{-1} become polarization independent when the extra domain content measured by the intensity ratio of $(1\bar{1}03)_{ZnO}/(1\bar{1}00)_{ZnO}$ is below $\sim 1.8\times10^{-4}$. We also correlated the peak positions of the E_2^{high} mode with the strain determined from the XRD results. From TEM measurement, we found a lot of BSFs density ($\sim 2\times10^{6}$ cm^{-1}) in two-step growth samples that helps to release the strains, and the D_0X, BSFs and (e, A) emissions dominate the NBE emission without deep-level and surface bound excitons (~ 3.17 eV) emission from PL spectra. The more BSFs density reduces the strain effect and generates the more BSFs emission in PL spectra. The two-step growth *m*-ZnO possess the smoother surface attributed to the lower or without other oriented growth in *m*-ZnO that will benefit for fabricating *m*-ZnO multilayer structures such as multiple quantum wells structures.

Finally, the *m*-plane nonpolar QWs show the quantum confinement effect with well widths below 8 nm, which confirm the nonpolar structure without internal field. The NBE emission from QWs is blue-shifted with respect to the bulk when the well width is narrower than 8 nm that shows the *m*-plane MQWs not only possess the quantum confinement effect but also prevent from the quantum confined Stark effect.

References

1. T. Moriyama and S. Fujita, Jpn. J. Appl. Phys., 44, 7919 (2005).

2. S. Nakamura, Jpn. J. Appl. Phys. 30, L1705 (1991).

3. S. Kim, J. Oh, J. Kang, D. Kim, J. Won, J. W. Kim and H.-K. Cho, J. Cryst. Growth 262, 7 (2004).

4. T. Hashimoto, M. Yuri, M. Ishida, Y. Terakoshi, O. Imafuji, T. Sugino, and K. Itoh, Jpn. J. Appl. Phys., 38, 6605 (1999).

5. X.H. Wu, P. Fini, E.J. Tarsa, B. Heying, S. Keller, U.K. Mishra, S.P. DenBaars, and J.S. Speck, J. Cryst. Growth, 189/190, 231 (1998).

6. H.J. Lee, S.W. Lee, H. Goto, H.-J. Lee, J.-S. Ha, K. Fujii, M.W. Cho, T. Yao, and S.K. Hong, J. Cryst. Growth, 310, 920 (2008).

7. C.F. Shih, M.Y. Keh, Y.N. Wang, N.C. Chen, C.-A. Chang, P.H. Chang, and K.S. Liu, J. Cryst. Growth, 277, 44 (2005).

8. J. Han, K.E. Waldrip, S.R. Lee, J.J. Figiel, S.J. Hearme, G.A. Petersen, and S.M. Myers, Appl. Phys. Lett. 78, 67 (2001).

9. C.Q. Chen, J.P. Zhang, M.E. Gaevski, H.M. Wang, W.H. Sun, R.S.Q. Fareed, J.W. Yang, amd M. Asif Khan, Appl. Phys. Lett. 81, 4961 (2002).

10. J.P. Zhang, H.M. Wang, M.E. Gaevski, C.Q. Chen, Q. Fareed, J.W. Yang, G. Simin, and M. Asif Khan, Appl. Phys. Lett. 19, 3542 (2002).

11. H. Takasu, P. Fons, K. Iwata, A. Yamada, K. Matsubara, R. Hunger, and S. Niki, J. Cryst. Growth, 227, 923 (2001).

12. H. Takasu, T. Tanabe, H. Takasu, P. Fons, K. Iwata, A. Yamada, K. Matsubara, R. Hunger, and S. Niki, Jpn. J. Appl. Phys., 40, 250 (2001).

13. H. J. Ko, Y. Chen, S. Hong, and T. Yao, J. Cryst. Growth, 209, 816 (2000).

14. S. Hong, H. J. Ko, Y. Chen, T. Hanada ,and T. Yao, J. Cryst. Growth, 214-215, 81 (2000).

15. J.-M. Chauveau, P. Vennéguès, M. Laügt, C. Deparis, J. Zuniga-Perez, and C. Morhain, J. Appl. Phys. 104, 073535 (2008).

16. C. C. Kuo, B. H. Lin, Song Yang, W. R. Liu, W. F. Hsieh, and C.-H. Hsu, Appl. Phys. Lett. 101, 011901 (2012).

17. Y. Chen, D. M. Bagnall, H.-J. Koh, K.-T. Park, K. Hiraga, Z. Zhu, and T. Yao, J. Appl. Phys. 84, 3912 (1998).

18. Y. Chen, D. M. Bagnall, Z. Zhu, T. Swkiuchi, K. Park, K. Hiraga, T. Yao, S. Koyama, M. Y. Shen, and T. Goto, J. Cryst. Growth, 181, 165 (1997).

19. W. L. Wang, Y. T. Ho, K. A. Chiu, C. Y. Peng, and L. Chang, J. Cryst. Growth, 312, 1179 (2010).

20. S. Yang, B. H. Lin, C. C. Kuo, H. C. Hsu, W.-R. Liu, M. O. Eriksson, P.-O. Holtz, C.-S. Chang, C.-H. Hsu, and W. F. Hsieh, Cryst. Growth Des. 12, 4745 (2012)

21. A. Teke, Ü. Özgür, S. Do˘gan, X. Gu, H. Morkoç, B. Nemeth, J. Nause, and H. O. Everitt, Phys. Rev. B 70, 195207 (2004).

22. A. Janotti and Chris G. Van de Walle, Phys. Rev. B 76, 165202 (2007).

23. R. Liu, A. Bell, and F. A. Ponce, C. Q. Chen, J. W. Yang, and M. A. Khan, Appl. Phys. Lett. 86, 021908 (2005).

24. I. Tischer, M. Feneberg, M. Schirra, H. Yacoub, R. Sauer, K. Thonke, T. Wunderer, F. Scholz, L. Dieterle, E. M¨uller, and D. Gerthsen, PHYSICAL REVIEW B 83, 035314 (2011).

25. W. Rieger, R. Dimitrov, D. Brunner, E. Rohrer, O. Ambacher, and M. Stutzmann, PHYSICAL REVIEW B 54, 17596 (1996).

26. P. Corfdir, P. Lefebvre, J. Levrat, A. Dussaigne, J.-D. Ganière, D Martin, J. Ristic, T. Zhu, N. Grandjean, and B. Deveaud-Plédran, J. Appl. Phys. 105, 043102 (2009).

27. M. Schirra, R. Schneider, A. Reiser, G. M. Prinz, M. Feneberg, J. Biskupek, U. Kaiser, C. E. Krill, K. Thonke, and R. Sauer, PHYSICAL REVIEW B 77, 125215

(2008).

28. T. Makino, C. H. Chia, N. T. Tuan, Y. Segawa, M. Kawasaki, A. Ohtomo, K. Tamura, and H. Koinuma, Appl. Phys. Lett. 76, 3549 (2000).

29. U. Ozgur, Ya. I. Alivov, C. Liu, A. Teke, M. A. Reshchikov, S. Doğan, V. Avrutin, S.-J. Cho, and H. Morkoc, J. Appl. Phys. 98, 041301 (2005).

30. C. Stampfl, C. G. Van de Walle, Phys. Rev. B, 57, R15052 (1998).

31. C. Stampfl and Chris G. Van de Walle, Phys. Rev. B 57, 15052 (1998).

32. Y. J. Sun, O. Brandt, U. Jahn, T. Y. Liu, A. Trampert, S. Cronenberg, S. Dhar, and K. H. Ploog, J. Appl. Phys., 92, 5714 (2002).

33. S. C. Ray, Y. Low, H. M. Tsai, C. W. Pao, J. W. Chiou, S. C. Yang, F. Z. Chien, W. F. Pong, M.-H. Tsai, K. F. Lin, H. M. Cheng, W. F. Hsieh, and J. F. Lee, Appl. Phys. Lett. 91, 262101 (2007).

34. W.-T. Hsu, K.-F. Lin, and W. F. Hsieh, Appl. Phys. Lett. 91, 181913 (2007).

35. T. Sander, S. Eisermann, B. K. Meyer, and P. J. Klar, PHYSICAL REVIEW B 85, 165208 (2012).

36. L. Bergman, X.-B. Chen, J. Huso, J. L. Morrison, and H. Hoeck, J. Appl. Phys. 98, 093507 (2005).

37. C. A. Arguello, D. L. Rousseau, and S. P. Porto, PHYSICAL REVIEW, 181, 1351 (1969).

38. K. Koike, K. Hama, I. Nakashima, G.-Y. Takada, K.-I. Ogata, S. Sasa, M. Inoue, and M. Yano, J. Cryst. Growth, 287, 288 (2005).

39. B. P. Zhang, B. L. Liu, J. Z. Yu, Q. M. Wang, C. Y. Liu, Y. C. Liu and Y. Segawa, Appl. Phys. Lett., 90, 132113 (2007)

40. T. Bretagnon, P. Lefebvre, T. Guillet, T. Taliercio, B. Gil and C. Morhain, Appl. Phys. Lett., 90, 201912 (2007)

41. T. Makino, A. Ohtomo, C.H. Chia, Y. Segawa, H. Koinuma and M. Kawasaki,

Physica E, 21, 671 (2004)

42. C. Morhain, T. Bretagnon, P. Lefebvre, X. Tang, P. Valvin, T. Guillet, B. Gil, T. Taliercio, M. Teisseire-Doninelli, B. Vinter, and C. Deparis, *Phys. Rev.* B 72, 241305 (2005).

43. T. Makino, Y. Segawa, A. Tsukazaki, A. Ohtomo, and M. Kawasaki, Appl. Phys. Lett. 93, 121907 (2008)

Chapter 7 Conclusions and Prospective

7.1 Conclusions

We have investigated for two nonpolar ZnO epifilms, $(11\bar{2}0)$- and $(1\bar{1}00)$-plane ZnO epifilms on *r*- and *m*- plane sapphire substrates by the laser-molecular beam epitaxy. We observed the in-plane anisotropic strains, tensile strain perpendicular to the *c*-axis and compressive stain parallel to the *c*-axis, cause crystal symmetry breaking from wurtzite (C_{6V}) to orthorhombic (C_{2V}) for the nonpolar $(11\bar{2}0)$ ZnO epilayers on *r*-sapphire. The as-grown *a*-ZnO epilayer has a small tilting angle ~ 0.3135^o of ZnO *c*-axis with respect to the optical plane of substrate that is closely related to the *r*-sapphire miscut, indicating high crystal quality. The observed blue-shift $E_2^{(high)}$ Raman mode contradicts with the anisotropic strain by XRD reveals violation of C_{6V} selection rule. Determining from the polarized Raman spectra of E_2 modes, the C_{2V} configuration satisfies most of the selection rules for the Raman modes but violation of the C_{6V} selection rule implies that the anisotropic strain on the nonpolar $(11\bar{2}0)$ ZnO epilayer may have changed crystal structure from C_{6V} to C_{2V}. The observed E_1 and E_2 bands in polarized optical reflection and photoluminescence spectra confirm that the anisotropic strains cause the structure change toward the orthorhombic structure for the nonpolar $(11\bar{2}0)$ ZnO epilayer grown on *r*-sapphire.

In the *m*-plane ZnO films grown on *m*-sapphire, we found small amount of $(1\bar{1}03)_{ZnO}$ domains provide strain relaxation of the *m*-ZnO matrix behaving as a low strain layer. Through carefully correlating low-temperature polarized PL spectra with the X-ray diffraction peak intensity ratio of $(1\bar{1}03)_{ZnO}/(1\bar{1}00)_{ZnO}$ of the samples

grown at different temperatures and after thermal treatment, we found that the broad-band emission around 3.17 eV may result from the interface defects trapped excitons at the boundaries between the $(1\bar{1}03)_{ZnO}$ domains and the *m*-ZnO matrix. The peak positions of the free A-, B- and C-exciton emissions in the PL spectra are close to that of bulk ZnO as a result of the $(1\bar{1}03)_{ZnO}$-oriented domains providing the strain relaxation mechanism. The more $(1\bar{1}03)_{ZnO}$ domains in the *m*-ZnO layer cause the more surface boundary that makes the stronger surface-bound-exciton emission. And the *a*-axes of both the $(1\bar{1}03)_{ZnO}$ domains and the *m*-ZnO matrix are aligned with the *c*-axis of the sapphire (α-Al_2O_3) substrate. The *c*-axis of the $(1\bar{1}03)_{ZnO}$ domains rotates about ±59° against the common *a*-axis of the *m*-ZnO.

We have successfully used a two-step growth method in *m*-ZnO on *m*-sapphire with LT-buffer to eliminate extra domains to reduce surface boundary trapping excitons. The as-grown LT-buffer exist large strain to reduce the main *m*-ZnO by the second step growth at high temperature. The two-step grown *m*-ZnO showing the lower strain from the XRD and Raman spectra is due to the LT-buffer sharing a lot of stresses from lattice mismatch. The thickness of LT-buffers has an ideal window from 47 to 67 nm for growing high temperature *m*-ZnO; below this range there exist extra domains but whose content ($\leq 3.6\times10^{-5}$) is one-order less than those made by direct growth *m*-ZnO without buffers. From AFM results, the two-step grown *m*-ZnO layers had smooth surface than without LT-buffer attributes the extra domains existence to add other growth orientated and make rough surface. The TEM and PL measurements indicate that more BSFs density $\sim 2\times10^{6}$ cm^{-1} with smooth surfaces in *m*-ZnO, which is larger than that of without buffers ($\sim 5\times10^{5}$ cm^{-1}), causes the stronger BSFs emission in LT-PL spectra. There are three dominant

emission peaks of D_0X, BSFs and (e, A) in LT-PL spectra of two-step *m*-ZnO. Finally, we confirm successful fabrication of nonpolar *m*-plane multiple quantum wells structures can be achieved by the two-step growth method. The *m*-plane MQWs show the blue-shift NBE emission spectra for well width narrower than 8 nm, exhibiting quantum confinement effect and free of the quantum confined Stark effect (QCSE) due to nonpolar nature, which has no internal field.

We have confirmed the change of optical properties in nonpolar ZnO epilayers result from the change of crystal structure. The change in optical transitions by the anisotropic strains in *a*-ZnO was identified by the symmetry breaking of C_{6V} to C_{2V} by polarized Raman, PL and optical reflection spectroscopy prior to the similar results reported in *a*-GaN by using polarized Raman spectroscopy recently in 2012. Furthermore, the first report to our knowledge in this study that the domain boundaries between the extra domains and main *m*-ZnO can trap the excitons to form the so-called surface-bound-excitons, proven by nicely correlating the characteristic of surface-bound-exciton emission with the extra domain content. By using the two-step growth method, we demonstrated successfully eliminating extra domains to reduce the surface-bound-exciton emission. This method provides a way of fabricating single-phase nonpolar *m*-ZnO structure with smooth surface and low strain state that merits for MQWs structure. The optical properties of nonpolar MQWs are consistent with other nonpolar MQWs which exhibit only quantum confinement effect with absence of the quantum confined Stark effect.

7.2 Prospective

In principle, $Mg_xZn_{1-x}O$ (MZO) could be engineered to achieve any bandgap in the range of 3.37 to 7.7 eV. However, the solubility of MgO in ZnO is limited in $0 < x < 0.33$ that restricts the band gap to the range of 3.37 eV $< E_g <$ 3.99 eV [**1**]. The

nonpolar ZnO QW based on ZnO/MZO structures have been reported without QCSE in literatures by MBE [**2, 3**] and laser-MBE [**4, 5**]. Photonic devices with nonpolar ZnO, such as *a*-plane (1120) and *m*-plane (1100), have been proposed to improve the quantum efficiency suffered by the quantum-confinement Stark effect (QCSE). The nonpolar QWs structures not only reduce the QCSE effect but also increase the polarized emission rate. We will grow the more nonpolar *a*-plane (1120) and *m*-plane (1100) ZnO QWs on *r*- and *m*-plane sapphires with various well widths and Mg contents. In addition, the surface roughness between the wells and barriers is also important to the QWs emission. The sharper the interface has the more efficient emission that also benefits for combining with the optical cavities. Many interesting physical properties in nonpolar QWs still need to investigate that are about excitons binding energy, exciton and phonon coupling interaction, phonon coupling with barriers, localized state, lifetime study, carriers dynamic and design barrier band engineered, etc.

If high density of excitons is excited in semiconductor materials such that average separation of excitons becomes shorter than the de Broglie wavelength of the exciton, then the excitons as quasi-Bosons would all condense to the lowest energy state. It is called the exciton Bose-Einstein condensates (BECs) [**6**]. The excitons BEC could generate the coherent emission as a laser does with high internal and extraction efficiencies having extreme low energy consumption. It is named the exciton polariton laser that has been recently realized in CdTe single quantum well within a microcavity at 19K under optical excitation 50 times below the lasing threshold [**6**]. A lot of polariton BEC effects have been observed in the semiconductor microcavity (MC) systems which often combine QWs and MCs to enhance electron and photon coupling generating polariton, including a bimodal momentum-space distribution with a narrow peak at zero momentum, long-range off-diagonal order [**6,7**], spatial

condensation in a macroscopic trap [**7,8**], spontaneous symmetry breaking [**9**], flow without dispersion [**10**], and a dramatic increase of coherence as measured in first-order and second-order correlation measurements [**11-13**]. Recently, L. Sapienza, *et al.* [**14**] have realized an electroluminescent device operating in the light-matter strong-coupling regime based on a GaAs/AlGaAs quantum cascade structure embedded in a planar MC. They experimentally demonstrated that the electrons can be selectively injected into polariton states up to RT. Intrinsic decoherence mechanisms in the MC polariton condensate have been studied limited by the combination of number fluctuations and interactions. [**15,16**] RT low-threshold transition to a coherent polariton state has been observed as polariton lasing in bulk wide bandgap GaN MC in the strong-coupling regime. [**17**] The observation of polariton lasing over such a broad range of temperatures reveals a clear transition from a kinetic to a thermodynamic regime with increasing temperature. Similar to GaN, ZnO is an environmental-friendly wide direct bandgap semiconductor. Therefore, dominant exciton emission can be constantly observed in ZnO even at RT. Due to its fast carrier cooling rate (< 200 fs) [**18**] and high Mott density (3.7 x 10^{19} cm^{-3}, exciton Bohr radius ~2.34 nm) and large Rabi splitting of 120 meV [**19**] that have been theoretically show that as a consequence of the broadening of the upper branch by the continuum, Rabi oscillations should not be observed in ZnO MCs which nevertheless remain good candidates for polariton-based effects (polariton BEC) involving the lower polariton branch. [**20**]

References

1. U. Ozgu¨r, Y. I. Alivov, C. Liu, A. Teke, M. A. Reshchikov, S. Dogan, V. Avrutin, S. J. Cho, and H. Morkoc, J. Appl. Phys. 98, 041301 (2005).

2. S. Sadofev, S. Blumstengel, J. Cui, J. Puls, S. Rogaschewski, P. Scha¨fer, Y. G. Sadofyev, and F. Henneberger, Appl. Phys. Lett. 87, 091903 (2005).

3. T. V. Shubina, A. A. Toropov, O. G. Lublinskaya, P. S. Kop'ev, S. V. Iva- nov, A. El-Shaer, M. Al-Suleiman, A. Bakin, A. Waag, A. Voinilovich, E. V. Lutsenko, G. P. Yablonskii, J. P. Bergman, G. Pozina, and B. Monemar, Appl. Phys. Lett. 91, 201104 (2007).

4. Marko Sto¨lzel Johannes Kupper, Matthias Brandt, Alexander Mu¨ller, Gabriele Benndorf, Michael Lorenz, and Marius Grundmann, JOURNAL OF APPLIED PHYSICS 111, 063701 (2012).

5. W. Bowen, W. Wang, E. Cagin, and J. Phillips, J. Electron. Mater. 37, 749 (2008).

6. Kasprzak, M. Richard, S. Kundermann, A. Baas, P. Jeambrun, J. M. J. Keeling, F. M. Marchetti, M. H. Szymanska, R. Andre, J. L. Staehli, V. Savona, P. B. Littlewood, B. Deveaud, and Le Si Dang, Nature 443, 409 (2006).

7. R. Balili, V. Hartwell, D. Snoke, L. Pfeiffer, and K. West, SCIENCE 316,1007 (2007).

8. B. Nelsen, R. Balili, D. W. Snoke, L. Pfeiffer, and K. West, J. Appl. Phys. 105, 122414 (2009).

9. J. J. Baumberg, A. V. Kavokin, S. Christopoulos, A. J. D. Grundy, R. Butte, G. Christmann, D. D. Solnyshkov, G. Malpuech, G. Baldassarri Hoger von Hogersthal, E. Feltin, J.-F. Carlin, and N. Grandjean, Phys. Rev. Letts. 101,136409 (2008).

10. A. Amo, J. Lefrère, S. Pigeon, C. Adrados, C. Ciuti, I. Carusotto, R. Houdré, E. Giacobino and A. Bramati, NATURE PHYSICS 5, 805 (2009).

11. D. Hagele, S. Pfalz, and M. Oestreich, Phys. Rev. Letts. 103, 146402 (2009).

12. Hui Deng, Glenn S. Solomon, Rudolf Hey, Klaus H. Ploog, and Yoshihisa Yamamoto, Phys. Rev. Letts. 99, 126403 (2007).

13. E. del Valle, D. Sanvitto, A. Amo, F.P. Laussy, R. Andre, C. Tejedor, and L. Vina, Phys. Rev. Letts. 103, 096404 (2009).

14. L. Sapienza, A. Vasanelli, R. Colombelli, C. Ciuti, Y. Chassagneux, C. Manquest, U. Gennser, and C. Sirtori, Phys. Rev. Letts. 100, 136806 (2008).

15. A. P. D. Love, D. N. Krizhanovskii, D. M. Whittaker, R. Bouchekioua, D. Sanvitto, S. Al Rizeiqi, R. Bradley, M. S. Skolnick, P. R. Eastham, R. Andre, and Le Si Dang, Phys. Rev. Letts. 101, 067404 (2008).

16. R. Cerna, D. Sarchi, T. K. Paraïso, G. Nardin, Y. Léger, M. Richard, B. Pietka, O. El Daif, F. Morier-Genoud, V. Savona, M. T., Portella-Oberli, and B. Deveaud-Plédran, Phys. Rev. B 80, 121309 (2009).

17. Raphaël Butté, Jacques Levrat, Gabriel Christmann, Eric Feltin, Jean-François Carlin, and Nicolas Grandjean, Phys. Rev. B 80, 233301 (2009).

18. Sun CK, Sun SZ, Lin KH, Zhang KYJ, Liu HL, Liu SC, and Wu JJ, Appl. Phys. Letts. 87(2), 023106 (2005).

19. M. Zamfirescu, A. Kavokin, B. Gil, G. Malpuech, and M. Kaliteevski, Phys. Rev. B 65, R161205 (2002).

20. S. Faure, T. Guillet, P. Lefebvre, T. Bretagnon, and B. Gil, Phys. Rev. B **78**, 235323 (2008).